SEL-71

# A Frequency-Tracking Direction Finder for Whistlers and Other Very Low Frequency Signals

by

Mark Keith Leavitt

December 1975

Technical Report No. 3456-2

Prepared under

Office of Naval Research Contract
Nonr N00014-67-A-0112-0012,
National Science Foundation
Section on Atmospheric Sciences
Grant DES-07707,
National Science Foundation
Office of Polar Programs
Grant GV-41369X



RADIOSCIENCE LABORATORY

STANFORD ELECTRONICS LABORATORIES

STANFORD UNIVERSITY • STANFORD, CALIFORNIA

(14) SU- SEL-76-001, TR-3456-2

(6) A FREQUENCY-TRACKING DIRECTION FINDER FOR WHISTLERS AND OTHER VERY LOW FREQUENCY SIGNALS.

by

(10) Mark Keith Leavitt

(12) 80 p.

(11) December 1975

(9) Technical Report No. 3456-2

Prepared under

(15)
Office of Naval Research
Contract Nonr N00014-67-A-0112-0012 NSF-GV-41369
National Science Foundation Section on Atmospheric Sciences
Grant DES-07707
National Science Foundation Office of Polar Programs
Grant GV-41369X

Radioscience Laboratory
Stanford Electronics Laboratories
Stanford University Stanford, California

332 400

## ABSTRACT

Whistlers and related very low frequency radio signals are guided in ducts of enhanced or reduced ionization along the geomagnetic lines of force of the earth's magnetosphere. The signals convey information about the distribution of particles in the plasma through which they have propagated and about the occurrence of wave-particle interactions in the magnetosphere. Direction-finding on such signals will aid in locating the ducts and measuring their temporal drifts, thus making an important contribution to studies of magnetospheric convection.

The signals, although narrowband in nature, exhibit wide frequency excursions in the 1 to 10 kilohertz range. An innovative technique is presented for tracking these frequency excursions in real time to produce a filtered, quasimonochromatic version of the signal. The voltages induced by the incident wave on two orthogonal loop antennas and a vertical monopole antenna are processed by this method. The filtered signals are then cross-multiplied in a manner analogous to a Poynting vector calculation to obtain a continuous indication of the wave direction of arrival.

The design, construction, and laboratory testing of a prototype instrument are described. Field testing of the instrument was performed at Stanford, California, and Roberval, Quebec, Canada. Operating at fixed frequencies, the direction-finder produced accurate results on VLF transmissions in the 10 to 20 kilohertz range from NAA, NPG, GBR, and the Omega stations. Well defined bearing indications were also obtained for spherics at frequencies in the 1 to 10 kilohertz region. Successful frequency-tracking and direction-finding were demonstrated for a wide variety of whistler-mode signals, including whistlers, chorus, and discrete emissions. The technique was also successfully applied to emissions

in the 2 to 7 kilohertz range stimulated by the VLF transmitter at Siple Station, Antarctica.

Direction of arrival indications on whistlers were consistent with the duct positions predicted by frequency profile analysis. Evidence was also presented of temporal changes in the direction of arrival of signals which may be an indication of duct drifts.

This instrument provides, for the first time, a continuous, immediately readable record of the direction of arrival of whistler-mode signals. It could also be applied to the automatic acquisition of whistler-mode signals and measurement of their amplitude and frequency variations.

## ACKNOWLEDGEMENTS

The author wishes to thank Professor R. A. Helliwell for his guidance, trust, and encouragement during the course of this research. In particular, his constant enthusiasm provided an essential spark of motivation through periods of failure as well as success.

Sincere appreciation is also expressed to Dr. D. L. Carpenter for his patient assistance and careful review of the manuscript; to Professor R. J. Smith for his helpful criticism; to Dr. C. G. Park and Mr. J. Katsufrakis for their continuing assistance and particular aid during the Roberval campaign; to Mr. J. Yarbrough for his friendly cooperation in preparing the spectral analyses; and to Mr. J. Lio for his fine craftsmanship in helping to construct the instrument.

A brief paragraph here cannot begin to express the gratitude due my wife, Susie, for her patience and spirit through the course of my graduate studies.

Finally, the author expresses his thanks to his employer, ESL Incorporated, and his supervisors in the Antenna/Microwave Laboratory, for their sponsorship and unflagging support throughout the course of his studies.

This research was supported in part by the Office of Naval Research under contract N00014-67-A-0112-0012, in part by the National Science Foundation Section on Atmospheric Sciences under grant DES-07707, and in part by the Office of Polar Programs of the National Science Foundation under grant GV-41369X.

## TABLE OF CONTENTS

## TABLE OF CONTENTS (Cont.)



## LIST OF TABLES

## ILLUSTRATIONS

ILLUSTRATIONS (Cont.)

ILLUSTRATIONS (Cont.)

ILLUSTRATIONS (Cont.)

ILLUSTRATIONS (Cont.)

# I. INTRODUCTION

## A. PURPOSE

The purpose of the research described herein is to develop apparatus and techniques for making direction of arrival measurements on whistlers and other very low frequency (VLF) signals in a field environment.

## B. BACKGROUND

### 1. Signals of Interest

Whistlers are bursts of VLF electromagnetic energy which originate in a lightning stroke and are guided along geomagnetic lines of force to the opposite hemisphere. Their character is that of a sweeping oscillation descending from the upper audio frequencies to the lower audio range in the course of a second or two; the frequency variation with time is a result of the dispersive propagation characteristics of the magnetoplasma through which the whistlers propagate. It is generally agreed [Helliwell, 1965] that the whistlers are guided in "ducts" of enhanced or reduced ionization within the magnetosphere. The frequency-time profile of a whistler conveys considerable information about particle densities in those regions of the magnetosphere through which the signal has passed. As a result, intensive scientific investigation has been underway since 1951, primarily consisting of the recording of VLF activity, spectrum analysis of the recorded tapes, and interpretation of the profiles.

While the frequency profile analysis can predict the equatorial radius of the duct, and hence the approximate magnetic latitude of its endpoint [Helliwell, 1965], no longitudinal information has been available other than the crude inference that the duct exit point is within some 500 to 1000 km radius of the recording station. Studies of the important problem of temporal drift of the ducts [e.g., Axford, 1969; Carpenter and Seely, 1975], and experiments to detect particles precipitated down into the atmosphere by the passage of waves through the magnetosphere require a more accurate means of locating the duct exit point. A single direction-finder determining the azimuthal angle of arrival of the signal could, in conjunction with the magnetic latitude analysis, locate the ducts; alternatively, direction-finding measurements at multiple, spaced stations could locate the ducts by triangulation, providing further data on the accuracy of the profile analysis as a predictor of the magnetic latitude of the duct exit point. These opportunities provide the motivation for the present research.

In addition to whistlers, the VLF spectrum exhibits other unusal signals which are less well-understood than whistlers and which are generally classified as "VLF emissions". Chorus and triggered emissions are prime examples of these signals. Of particular current interest are the artificially stimulated emissions (ASE) produced by the 100 kW VLF transmitter operated by Stanford University researchers at Siple Station, Antarctica [Helliwell and Katsufrakis, 1974]. These signals present an opportunity for investigation beyond the realm of natural whistlers; the stimulus energy can be controlled

to enhance the effects under study and reduce other phenomena which mask them. It is therefore desirable that a whistler-mode direction-finder be capable of operating on these signals also.

2. Classification of Direction Finding Techniques.

All direction-finders are specialized antenna and receiver systems which determine the direction of arrival of an incident electromagnetic wave. Classifications can be made according to which wave properties are measured and according to how these measurements are processed to determine the direction of arrival.

Consider a general plane wave propagating in free space toward a direction-finder site as illustrated in Fig. 1.1. The azimuthal angle of arrival is denoted by $\theta$ and the elevation angle by $\beta$. The wave polarization is described by an ellipse having an axis ratio R and a tilt angle $\alpha$ of the major axis. Any arbitrary polarization can be described by these parameters; note that $|R| \leq 1$, and that $R>0$ corresponds to right-hand polarization, while $R<0$ denotes left-hand polarization. (These geometrical conventions are similar to those employed by Bullough and Sagredo [1973] and are convenient both for visualization and for comparison of the new system with existing techniques.) The electric and magnetic fields of the wave are expressed as:

$$\begin{aligned} \mathbf{E} &= \mathrm{Re}\left[E_1 e^{j\omega t}(\cos\alpha\,\hat{a}_{\parallel} - \sin\alpha\,\hat{a}_{\perp}) + jE_2 e^{j\omega t}(-\sin\alpha\,\hat{a}_{\parallel} - \cos\alpha\,\hat{a}_{\perp})\right] \\ \mathbf{H} &= \mathrm{Re}\left[\frac{1}{\eta}E_1 e^{j\omega t}(\cos\alpha\,\hat{a}_{\perp} + \sin\alpha\,\hat{a}_{\parallel}) + j\frac{1}{\eta}E_2 e^{j\omega t}(-\sin\alpha\,\hat{a}_{\perp} + \cos\alpha\,\hat{a}_{\parallel})\right]. \end{aligned} \tag{1.1}$$

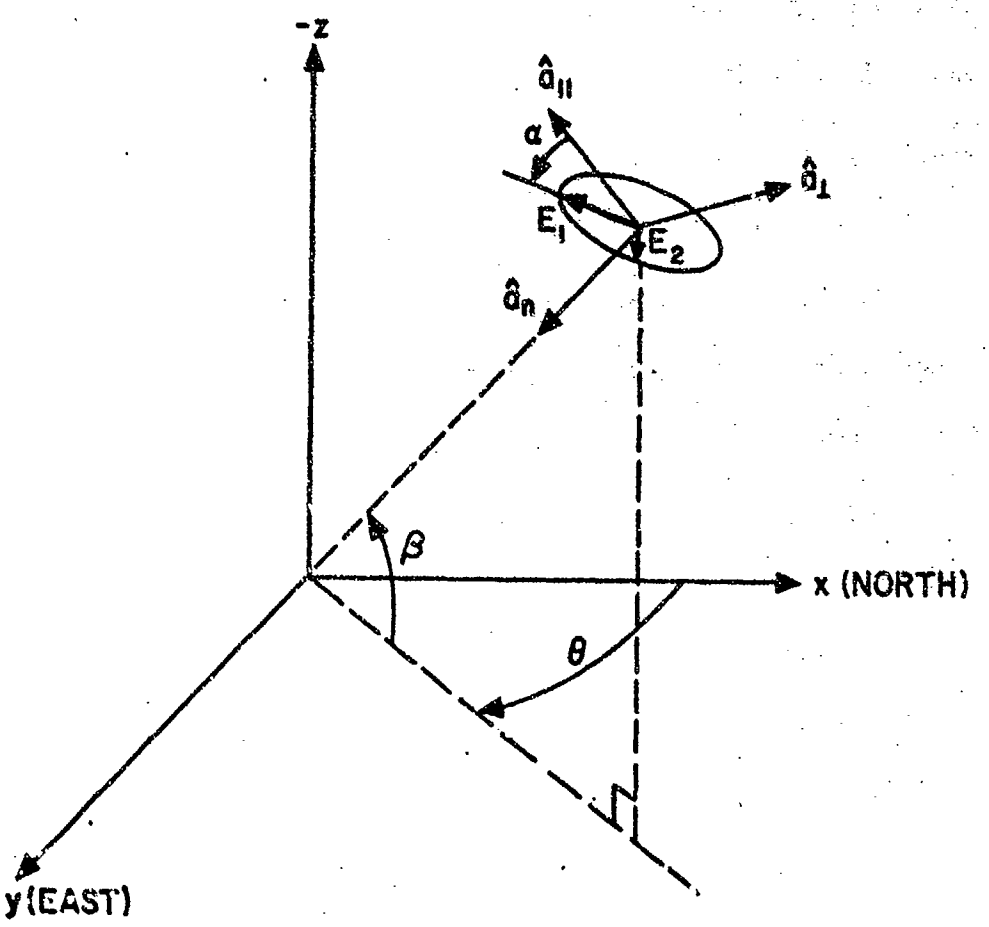


Notes:

1. $\hat{a}_n$, $\hat{a}_{\parallel}$, $\hat{a}_{\perp}$ are the unit vectors in the wave coordinate system; $\hat{a}_n$ is the direction of propagation, $\hat{a}_{\parallel}$ lies in the plane of incidence, and $\hat{a}_{\perp}$ is mutually perpendicular to $\hat{a}_n$ and $\hat{a}_{\parallel}$.
2. $E_1$ and $E_2$ are scalar quantities indicating the electric field along the major and minor axes of the polarization ellipse, respectively.
3. $R = E_2/E_1$.
4. R is positive for right-hand polarization.
5. With the x and y axes aligned as shown, the +z axis must point downward to maintain a right-handed coordinate system.

FIGURE 1.1 A GENERAL PLANE WAVE PROPAGATING TOWARD A DIRECTION-FINDER SITE.

In accord with the usual convention, we will drop the $e^{j\omega t}$ and Re[] symbols. Also applying the relation $R=E_2/E_1$, the fields can be expressed as

$$\mathbf{E} = E_1 \left[(\cos\alpha\,\hat{a}_{\parallel} - \sin\alpha\,\hat{a}_{\perp}) + jR\,(-\sin\alpha\,\hat{a}_{\parallel} - \cos\alpha\,\hat{a}_{\perp})\right]$$

$$\mathbf{H} = \frac{1}{\eta} E_1 \left[(\cos\alpha\,\hat{a}_{\perp} + \sin\alpha\,\hat{a}_{\parallel}) + jR\,(-\sin\alpha\,\hat{a}_{\perp} + \cos\alpha\,\hat{a}_{\parallel})\right] . \tag{1.2}$$

Measurement of the complete vector electric and magnetic fields at the direction-finder site is sufficient to determine the direction of power flow from Poynting's theorem. In theory, antennas could be constructed to independently sense $E_x$, $E_y$, $E_z$, $H_x$, $H_y$, and $H_z$ and circuits could be employed to execute the multiplications and additions necessary to compute $P_x$, $P_y$, and $P_z$, completely defining the propagation direction. Since the signal may have propagated via several reflections between the earth and ionosphere, the elevation angle of arrival is of limited usefulness in locating the source. Hence, ground based systems are often intentionally limited to the determination of azimuthal direction and only two or three field components are measured. Direction-finders operating on the power-flow measurement principle can utilize antenna systems which are small relative to the wavelengths involved and hence may be termed "small-aperture" direction-finders.

In contrast, "large-aperture" direction finders utilize antenna arrays which are appreciable in size relative to the signal wavelengths. One popular type is the "interferometer" direction-finder, in which multiple, spatially separated antennas are employed. Consider a system in which antennas are located at the origin of the coordinate system of Fig. 1.1 and also at some

radial distance along the x, y, and z axes. Each of the outlying antennas will sense a wave phase, relative to the wave phase at the origin, that corresponds to the projection of the wavenormal vector along that axis, thereby defining the direction of propagation. Again, most practical ground based systems are limited to the measurement of x and y components, and hence only the azimuthal arrival angle is determined.

The accuracy of the large-aperture system is proportional to the spacings used; the performance of the two types of direction-finders in the presence of instrumental imperfections and noise is shown in Appendix A to be comparable when the large-aperture system is constructed with antenna spacings of $\lambda/2\pi$. This principle is responsible for the practical preference for large-aperture systems at the high-frequency band and above, where spacings larger than this are easily achieved, and for the predominance of the small-aperture approach in the VLF range, where such spacings require large amounts of real estate and the long distance transmission of phase data.

As stated earlier, direction-finders can also be classified according to how the wave measurements are processed to determine the direction of arrival, regardless of which wave measurements are made.

Consider the general system configurations in Fig. 1.2. In the first system, (a), parallel channels filter the antenna signals and then a calculation is made in a non-linear processor to determine the direction of arrival. Contrast with this the second system, (b), in which the antenna signals are first combined in some time-varying manner, passed through a single

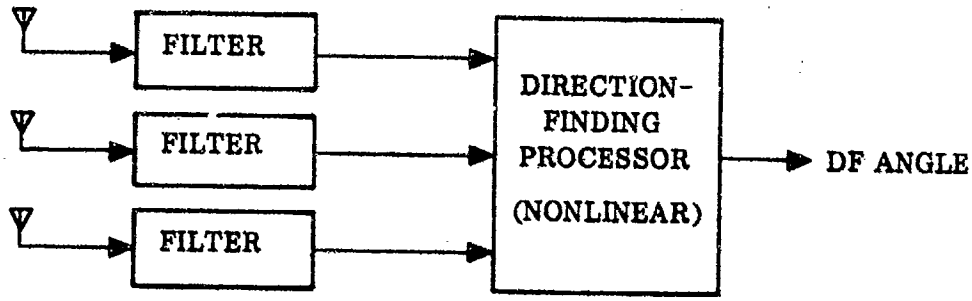


(a)

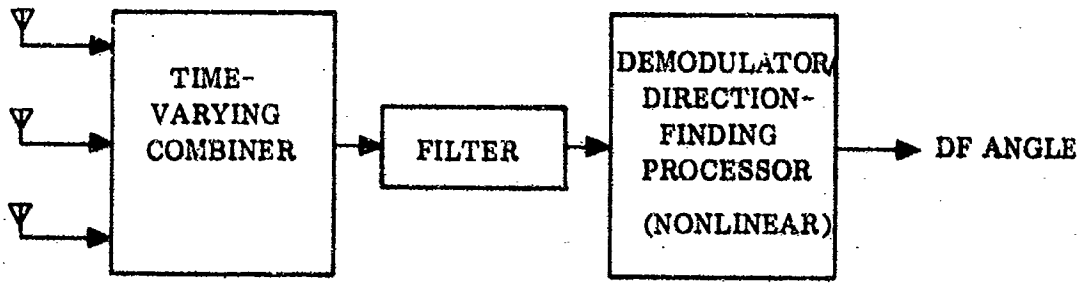


(b)

FIGURE 1.2 GENERAL CONFIGURATIONS FOR PROCESSING WAVE MEASUREMENTS TO DETERMINE DIRECTION OF ARRIVAL. (a) Multichannel, parallel processing. (b) Single-channel, sequential processing.

filtering channel, and then processed to calculate the direction of arrival. When the filtering operation requires human intervention, the broadband unfiltered signals must be recorded, and in this case the single channel system displays the advantage of requiring only one recording channel as compared to the requirement for matched multiple channels in the parallel system. However, signals of brief duration and signals exhibiting fading or modulation at frequencies comparable to the time-varying combiner operating frequency are prone to errors or complete loss of directional data in the single channel approach. The great majority of work in VLF direction-finding has been based on examination by an analyst of the entire spectrum to locate the signals of interest. Hence, the single-channel approach, embodying the rotating goniometer as the time-varying combiner, has predominated.

3. Prior Efforts in VLF Direction-Finding.

The earliest interest in direction-finding at VLF [Ockenden, 1954 ; Adcock and Clarke, 1947] was apparently motivated by a desire to locate the sources of atmospherics (generated by lightning strokes) for meteorological purposes. In the early systems, the voltages induced on a pair of crossed loop antennas were applied through dual amplifiers to the deflection plates of a cathode ray tube. Direction of arrival indication was purely visual and practically instantaneous. In the classification framework presented above, these systems would be described as small-aperture direction-finders using multi-channel parallel signal processing. The polarization errors which can occur in such crossed loop small-aperture

systems when the incident wave is not purely vertically polarized were discussed by Horner [1954]. Using continuous wave signals from station GBR, Horner [1957] also demonstrated that while daytime polarization errors were low (less than $10^{\circ}$), the nighttime values ranged up to $40^{\circ}$, being most prominent at distances of about 300 km and less prevalent at shorter and longer distances.

Specific attacks on the whistler direction-finding problem began in 1955 with Crary [1961], and Watts [1959] who used a rotating goniometer to combine the outputs of the crossed loops into a composite channel. These systems followed the "single-channel" philosophy, with the goniometer serving as the time-varying combiner, because it was necessary to record the entire VLF spectrum. The broadband tape recordings were spectrum analyzed onto paper or film, and then visually examined to locate the whistlers, determine their "null pattern", and compare the pattern with some reference to measure the direction of arrival. Some whistlers exhibited nulls while others did not. As a possible explanation, Watts pointed out that downcoming circularly polarized signals would not display good nulls on such a system. Another justification for the absence of nulls in "swishy" whistlers was that they would probably be composed of many elementary whistlers arriving from different directions. Ellis [1960] found incomplete nulls when measuring VLF noise at 5 kHz and advanced a similar explanation: the source must be of wide angular extent. The most recent efforts with the goniometer and crossed loops have been published by Bullough and Sagredo [1973]. Their data show

wide variability in the measured direction even on a single whistler, but when averaged over several whistlers judged from frequency profile analysis to have the same path, the RMS deviation is on the order of $\pm 10^{\circ}$ to $\pm 20^{\circ}$. This wide variability in the apparent direction was predicted in Crary's [1961] propagation analyses, along with indications that averaging the data over frequency could achieve considerable reductions in the error.

Tracing the history of "large-aperture" systems at VLF, it appears that the application of this technique for whistlers was first suggested by Crombie [1955] who recommended spacings of $0.15\lambda$, which, interestingly, compares closely with the spacing $(\lambda/2\pi)$ at which the large-aperture and small-aperture techniques display comparable accuracy in the presence of noise. The first report on an actual application of the technique is given by Delloue [1960], who used spaced loops and a radio relay link to transmit the phase information. He reported that the direction of arrival tended to "circle about the magnetic field line" and that the polarization varied rapidly. Another large - aperture system has been built by the National Bureau of Standards at Brighton, Colorado, as described by Hefley et al. [1961], with claimed accuracy of under $1^{\circ}$; however, it is adapted only for used with atmospherics. The antennas are placed at the vertices of an equilateral triangle with sides 4 miles in length and the signals are conveyed to the central location by transmission lines.

Of particular interest in this research are the efforts in small-aperture, multi-channel systems. Cousins [1972] proposed a method for combining the

signals from crossed loops and a vertical antenna which would yield no polarization error, provided the antenna responses were perfectly in agreement with theory and the incoming signals was not purely vertically polarized.† He recorded the three antenna signals on a multi-channel tape recorder, then digitized the spectra, and performed the filtering and processing on a computer in an interactive mode with a human operator. Tsuruda and Hayashi [1974] have described and built a system using a similar principle, but employing analog processing instead. These techniques are characterized by the need for multichannel phase and amplitude matched recording capability; human intervention is required to locate the frequency-time profile of the signal and adjust the filtering to extract it before the direction-finding processing is performed.

C. APPROACH SELECTED

With the goal of this research being the development of apparatus suitable for field usage, considerations of practicality entered the design at an early stage. At very low frequencies, the small-aperture antenna system is much more attractive than the large-aperture array with its attendant real estate requirements and the difficulty involved in conveying the antenna signals long distances to the processing site. In view of this consideration, and the predominance of crossed loop antenna systems at existing VLF receiving sites, the small-aperture approach was chosen. The more fruitful area for improvement was found to be in overcoming the limitation of existing

† For a discussion of this point see Section II.C.5.

VLF data gathering and signal processing techniques. Current methods customarily employ either broadband recording of the entire spectrum with subsequent examination of spectrum records by an analyst, or fixed frequency narrowband reception. The latter method can capture only a fraction of the typical whistler or artificially stimulated emission in the course of its wide frequency variation with time. A visible gap between these techniques exists: broadband analysis provides only rough indications of intensity as a function of frequency; narrowband techniques produce detailed data on the signal characteristics, but capture only a fraction of the desired signal. If an instrument could be developed which would automatically detect and filter a frequency-varying VLF signal from the background energy in real time, this gap would be bridged. The following benefits would be expected:

a. the multichannel processing technique of Fig. 1.2(a) would become feasible, producing a continuous record of direction of arrival uncompromised by fading or signal modulation, and usable for signals of any duration;

b. a greater amount of data about temporal and frequency-dependent variations in the apparent direction would be produced, and improved accuracy due to averaging out of errors over the entire signal profile would be expected;

c. automatic extraction of other signal parameters such as frequency and amplitude would be made practical; and

d. the burden on the human observer of searching and scaling spectral records would be reduced.

With this motivation, a new approach to VLF signal data gathering was conceived, following the block diagram of Fig. 1.3.

## D. CONTRIBUTIONS OF THE PRESENT WORK

The most important contributions of this research are summarized as follows:

1. A new and innovative technique for filtering and extracting direction of arrival information from whistlers and other VLF signals is proposed; the method is analyzed and compared to alternative approaches in theory; a prototype instrument embodying the new technique is designed and constructed and deployed in an actual field environment. The practicality, efficiency, and utility of the approach under these conditions are demonstrated.

2. The direction-finding data produced are of higher accuracy than that from existing approaches, displaying less polarization error and no $180^{\circ}$ ambiguity; the temporal resolution is continuous as compared to 10 or 25 sample-per-second limitations of the conventional goniometer. These advantages permit more detailed direction of arrival studies of the substructure within whistler events, including precursors and triggered emissions, as demonstrated in the observed data.

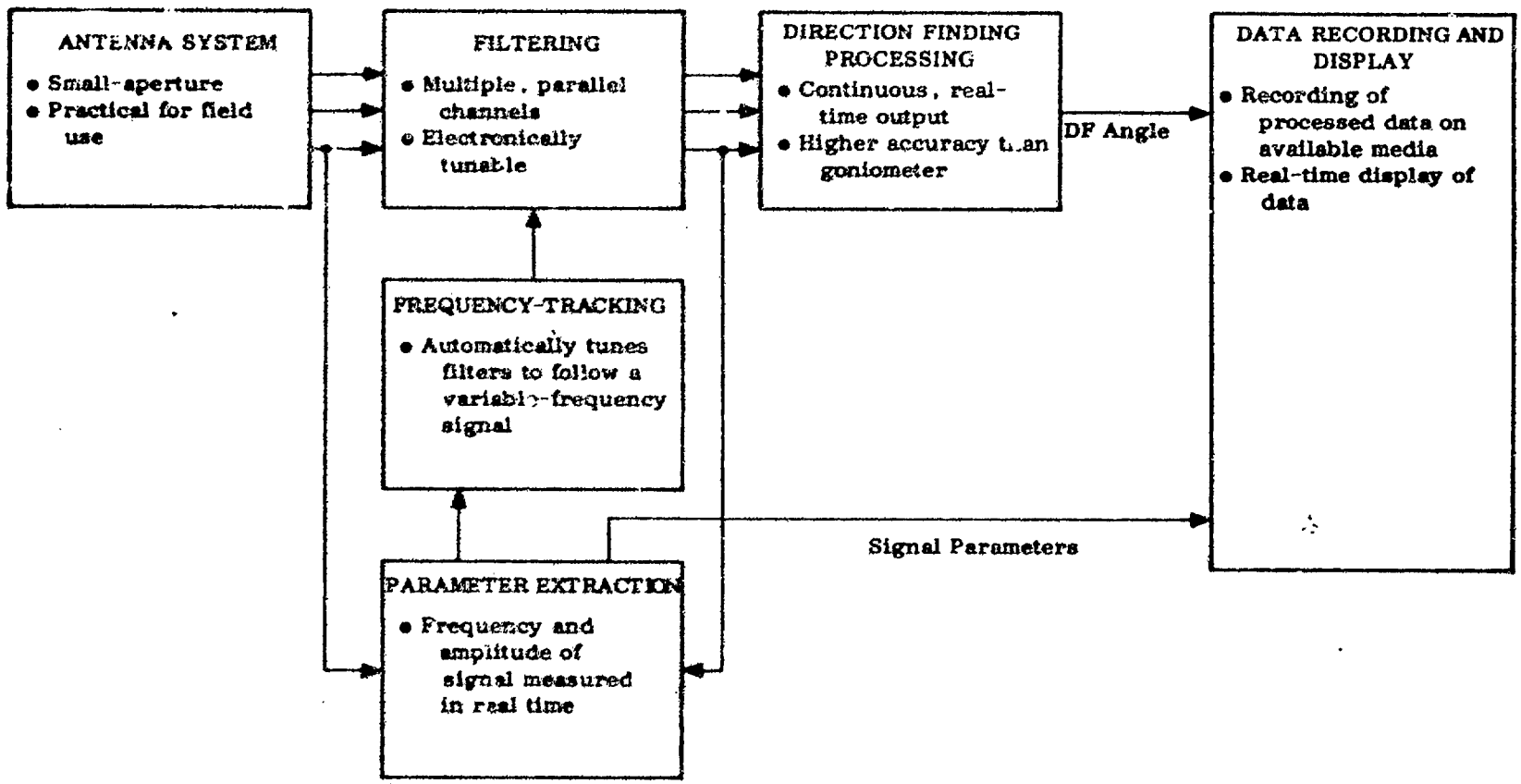


FIGURE 1.3 NEW APPROACH TO VLF DIRECTION FINDING AND DATA GATHERING

3. Examples of temporal changes in the direction of arrival of whistler-mode signals are found which may indicate drifting of magnetospheric ducts.

4. The first direction-finding on signals received via magnetospheric amplification from Siple Station, Antarctica, is demonstrated. Duct exit points indicated by the direction-finder agree with those of whistlers received in the same time period.

## II. THEORY AND ANALYSIS

### A. FREQUENCY-TRACKING OF VLF SIGNALS

The concept of adjusting the frequency of a receiver or filter to follow the frequency of a signal has been applied in other contexts; in particular, the technology of phase-locked receivers for satellite signal reception is highly advanced, as described by Gardner [1966]. All of these applications, however, involve tracking over a narrow frequency range relative to the signal frequency, whereas a whistler at VLF may sweep over a decade range in frequency. To accommodate such an excursion, new concepts in the design of the frequency-tracking circuitry must be introduced.

#### 1. Tracking Loop Characteristics and Limitations.

Two configurations for achieving automatic tuning of a receiver or filter, open-loop and closed-loop, are illustrated in Fig. 2.1. When the purpose of the filtering is to extract the signal from background noise and interference, the open-loop approach is clearly unsuitable as the frequency information would contain these undesirable elements and tracking would be poor; open-loop operation is also more sensitive to small drifts in circuit parameters. Thus, the logical choice is the closed-loop configuration, in which the frequency information is extracted from the filtered signal and fed back to control the tuning of the receiver. Furthermore, the most practical way to achieve electronic tuning of multiple filtering channels is to use fixed filters and to instead translate the frequency of the incoming signals by an electronically variable amount, using a voltage-controlled local oscillator

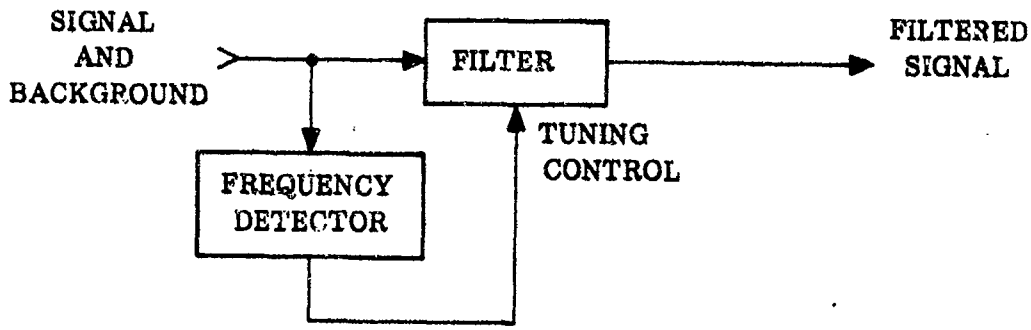


(a)

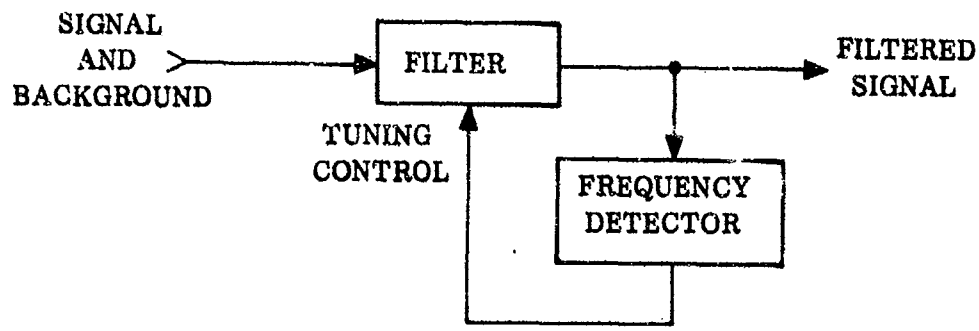


(b)

FIGURE 2.1 CONFIGURATIONS FOR FREQUENCY TRACKING. (a) Open loop. (b) Closed loop.

and mixers. Implementation of this technique is illustrated in Fig. 2.2.

A rigorous analysis of the operation of such circuitry is beyond the realm of linear circuit theory, because of the presence of nonlinear elements: mixers, voltage-controlled oscillators, limiters and frequency discriminators. However, by proper definition of the system variables and by restriction of the range of operation, a linear model can be produced. The voltage-controlled oscillator and frequency discriminator can be modeled as linear, memoryless voltage-to-frequency and frequency-to-voltage transducers. The mixer, which generates sum and difference frequencies from its input signals, can be represented as a frequency subtractor. (The sum frequency component is not passed by the IF filter.) For the IF filter, the problem lies in determining the response of the output frequency to changes in the input frequency. Panter [1965] and Baghdady [1961] have performed analyses demonstrating that an appropriate linear model for the "modulation transfer function" is provided by mathematically translating the IF bandpass filter function into a low-pass filter function centered at zero frequency. With the benefit of these approximations, an analog to the system can be constructed as in Fig. 2.3.

Changes in the tuning frequency of the receiver are brought about by the detected frequency error $\Delta f$ in the IF passband. The error which must be tolerated to produce the necessary changes depends on the loop feedback filter used. A pure, memoryless amplifier for feedback requires an error proportional to the tuning offset needed (that is, the difference between the signal frequency and the receiver quiescent tuning frequency). With a

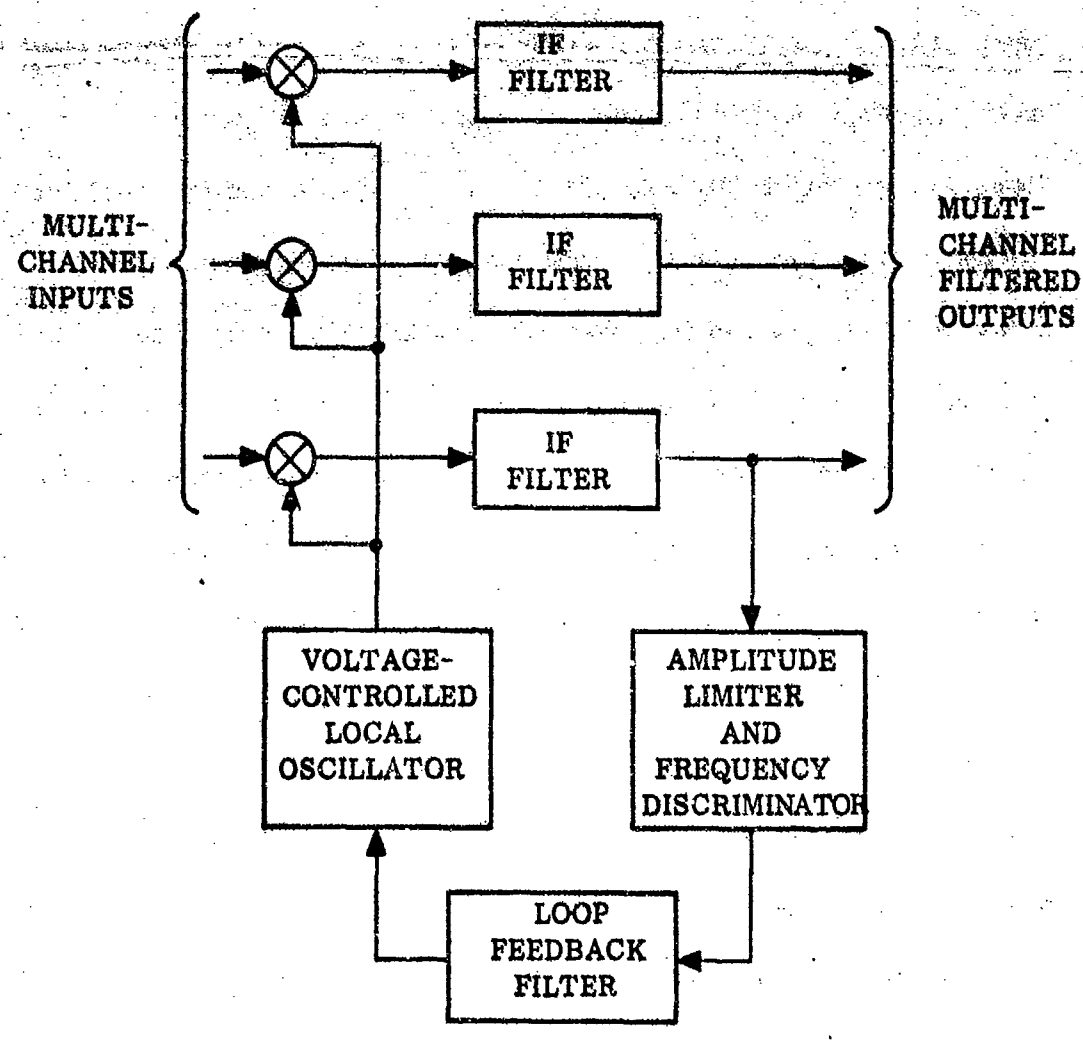


FIGURE 2.2 IMPLEMENTATION OF A MULTICHANNEL SUPERHETERODYNE FREQUENCY-TRACKING RECEIVER.

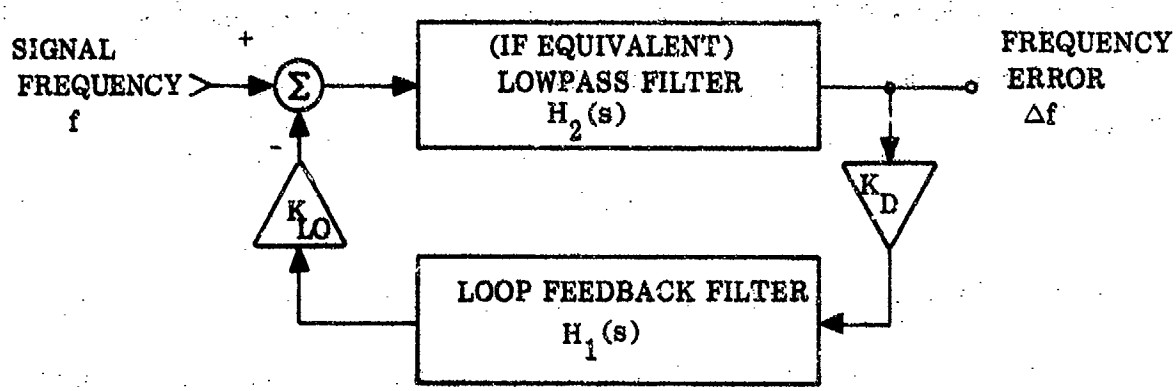


FIGURE 2.3 LINEAR MODEL OF FREQUENCY-TRACKING LOOP.

single integrator in the loop, the error is zero for any constant frequency signals and proportional to df/dt for changing frequencies. With double integration, the error is proportional to $d^2f/dt^2$, and so on; however, the higher the order of integration, the slower the initial response of the loop to the transients involved in acquiring a new signal. For whistlers, a single integrator appears to be the optimum choice.

Let us now address the question of loop gain and stability. The DC gain constants around the loop may be lumped into a single factor K and incorporated into the integrator gain, giving

$$H_1(s) = K/s \tag{2.1}$$

as the LaPlace transform transfer function of the loop feedback filter. The modulation transfer function for the IF filter depends on the exact shape of the filter response; however, a good approximation for most practical circuits is given by

$$H_2(s) = \frac{(BW_{rad}/2)^2}{s^2 + (BW_{rad}/2)s + (BW_{rad}/2)^2} \tag{2.2}$$

where $BW_{rad}$ is the bandwidth of the IF bandpass filter in radians per second. This function exhibits a conjugate pole pair at the natural frequency $(BW_{rad}/2)$, with damping ratio $\frac{1}{2}$. The response of the entire loop is then described by the roots of the characteristic polynomial,

$$s^3 + (BW_{rad}/2)\ s^2 + (BW_{rad}/2)^2 s + K(BW_{rad}/2)^2. \qquad (2.3)$$

Applying the Routh-Hurwitz stability criterion [Melsa and Schultz, 1969], the loop response will be stable if

$$K < (BW_{rad}/2). \qquad (2.4)$$

Allowing the customary stability margin, a convenient value for the gain is

$$K = (BW_{rad}/2)/\pi = BW_{Hz}. \qquad (2.5)$$

(Hereafter, $BW_{IF}$ will be taken to represent $BW_{Hz}$.)

In order to simplify the calculation of system response to various inputs, it can be observed that the loop behavior is dominated by the integrator pole at zero frequency; thus, although the complete loop transfer function must be considered in determining stability, a modified loop model as shown in Fig. 2.4 is adequate for determining system response. Using $K=BW_{IF}$, the differential equation for the frequency error $\Delta f$ is given by

$$\Delta f = \frac{df/dt - d\Delta f/dt}{BW_{IF}} \qquad (2.6)$$

from which we can conclude that:

a. for a constant frequency input, the steady state error is zero;

b. for a small step change in frequency, the transient response has a time constant of $(1/BW_{IF})$;

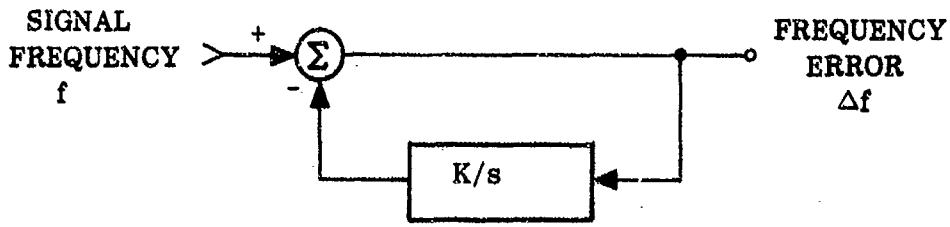


FIGURE 2.4 SIMPLIFIED SYSTEM RESPONSE MODEL.

c. for a frequency ramp input, the steady state error is constant and equal to $\frac{df/dt}{(BW_{IF})}$; and

d. the maximum rate of change in frequency, or fastest ramp which can be tracked, is that for which $|\Delta f| = (BW_{IF}/2)$, in order that the signal remain within the IF passband. Therefore,

$$|df/dt|_{max} = BW_{IF}^2/2. \tag{2.7}$$

2. Tracking in the Presence of Noise and Interference.

Let us postulate the addition of white noise to the signal. The noise power spectral density shall be denoted by $N_o$, and the signal power by S. Then the signal-to-noise ratio in the IF is,

$$(S/N)_{IF} = \frac{S}{N_o BW_{IF}} . \tag{2.8}$$

Gardner [1966] has shown that passage of the signal and noise through an amplitude limiter has a moderate enhancement effect on signal-to-noise ratio as given by

$$(S/N)_{LIM} = (S/N)_{IF} \left[ \frac{1 + 2(S/N)_{IF}}{4/\pi + (S/N)_{IF}} \right] \tag{2.9}$$

which is well approximated by

$$(S/N)_{LIM} = 2(S/N)_{IF} \tag{2.10}$$

for all $(S/N)_{IF}$ greater than 0 dB. Applying the limited signal to the discriminator, Panter [1965] has shown an analysis demonstrating that the voltage output of the discriminator will contain a mean-square fluctuating component of

$$\overline{e_n^2} = K_D^2 \frac{1.64}{(S/N)_{LIM}} BW_{IF}^2 , \tag{2.11}$$

which, combining the limiter and discriminator, gives

$$\overline{e_n^2} = K_D^2 \frac{0.82}{(S/N)_{IF}} BW_{IF}^2 . \tag{2.12}$$

The noise voltage may be equivalently expressed as representing a frequency error due to noise, $\Delta f_n$. Since

$$\Delta f_n = e_n / K_D ,$$

the RMS value for $\Delta f_n$ is given by,

$$(\Delta f_n)_{RMS} = \frac{0.91}{\sqrt{(S/N)_{IF}}} BW_{IF} . \tag{2.13}$$

Thus, the frequency error is a zero mean, fluctuating component with an RMS value approximately equal to the bandwidth divided by the square root of the signal-to-noise ratio.

At moderate to high signal-to-noise ratios, the presence of such a noise component does not disrupt the basic tracking behavior of the receiver. At low signal-to-noise ratios, however, the fluctuation noise exceeds the range of the linear approximations made in studying the loop behavior. A

rigorous solution to the behavior of the loop under such conditions has not been demonstrated; however, a number of workers have applied experimental, simulative, and analytical techniques with the conclusion that a sharp threshold exists near unity signal-to-noise ratio below which tracking is not possible [Panter, 1965].

Let us now study instead the addition of a second, coherent signal within the IF passband. This interfering signal might be due to another source or it could be a component from the same origin which has propagated via a different path. The frequencies of the desired and undesired signals are denoted by $f_1$ and $f_2$, respectively, and the power ratio as $(S/I)_{IF}$. Both signals are passed by the IF filter and applied to the limiter-discriminator. The effect of the limiter in this case has been shown by Baghdady [1961] to be a moderate suppression of the weaker signal in the presence of the stronger one, approximated by

$$(S/I)_{LIM} \cong (S/I)_{IF} \left[2 - \frac{1}{4(S/I)_{IF}}\right]^2 \qquad (2.14)$$

for $(S/I)_{IF} > 2$, which in turn can be approximated as

$$(S/I)_{LIM} \cong 4\,(S/I)_{IF}. \qquad (2.15)$$

Applying this factor, the amplitude of the interfering signal relative to a unit amplitude desired signal is

$$A_i = \frac{1}{2\sqrt{(S/I)_{IF}}} \tag{2.16}$$

at the input to the discriminator. The vectoral combination of these two signals is illustrated in Fig. 2.5. The phase of the resultant of the two signals is given by

$$\Phi_R = 2\pi f_1 t + \tan^{-1}\left[\frac{A_i \sin 2\pi (f_2 - f_1) t}{1 + A_i \cos 2\pi (f_2 - f_1) t}\right] .$$

The interference term, represented by the second part of the expression for $\Phi_R$, can be expressed alternatively as a series, giving

$$\Phi_R = 2\pi f_1 t + \sum_{n=1}^{\infty} (-1)^{n+1} (A_i)^n (1/n) \sin 2\pi n (f_2 - f_1) t,$$

and, taking derivatives to convert phase into instantaneous frequency, we have

$$f_R = f_1 + (f_2 - f_1) \sum_{n=1}^{\infty} (-1)^{n+1} (A_i)^n \cos 2\pi n (f_2 - f_1) t \quad . \tag{2.17}$$

Thus, the output of the frequency discriminator will contain a steady component correctly representing the frequency of the strong signal $f_1$, plus a time-periodic error component $\Delta f_i$ due to the presence of the weaker interfering signal. The character of $\Delta f_i$ is illustrated in Fig. 2.6 [Panter, 1965]. From the form of the expression for $\Delta f_i$, a summation of harmonic cosinusoids

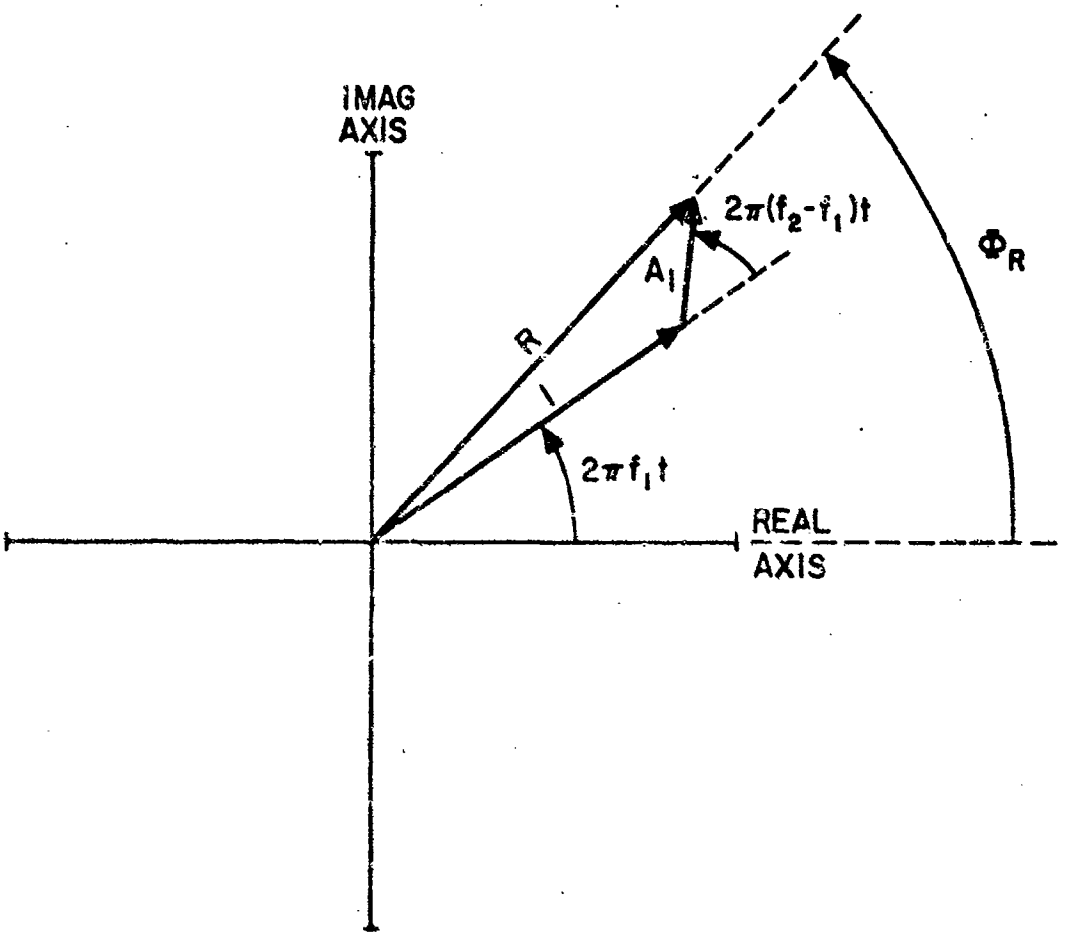


FIGURE 2.5 VECTORAL COMBINATION OF A DESIRED, UNIT-AMPLITUDE SIGNAL AT FREQUENCY $f_1$ AND AN INTERFERING SIGNAL OF AMPLITUDE $A_1$ AT FREQUENCY $f_2$.

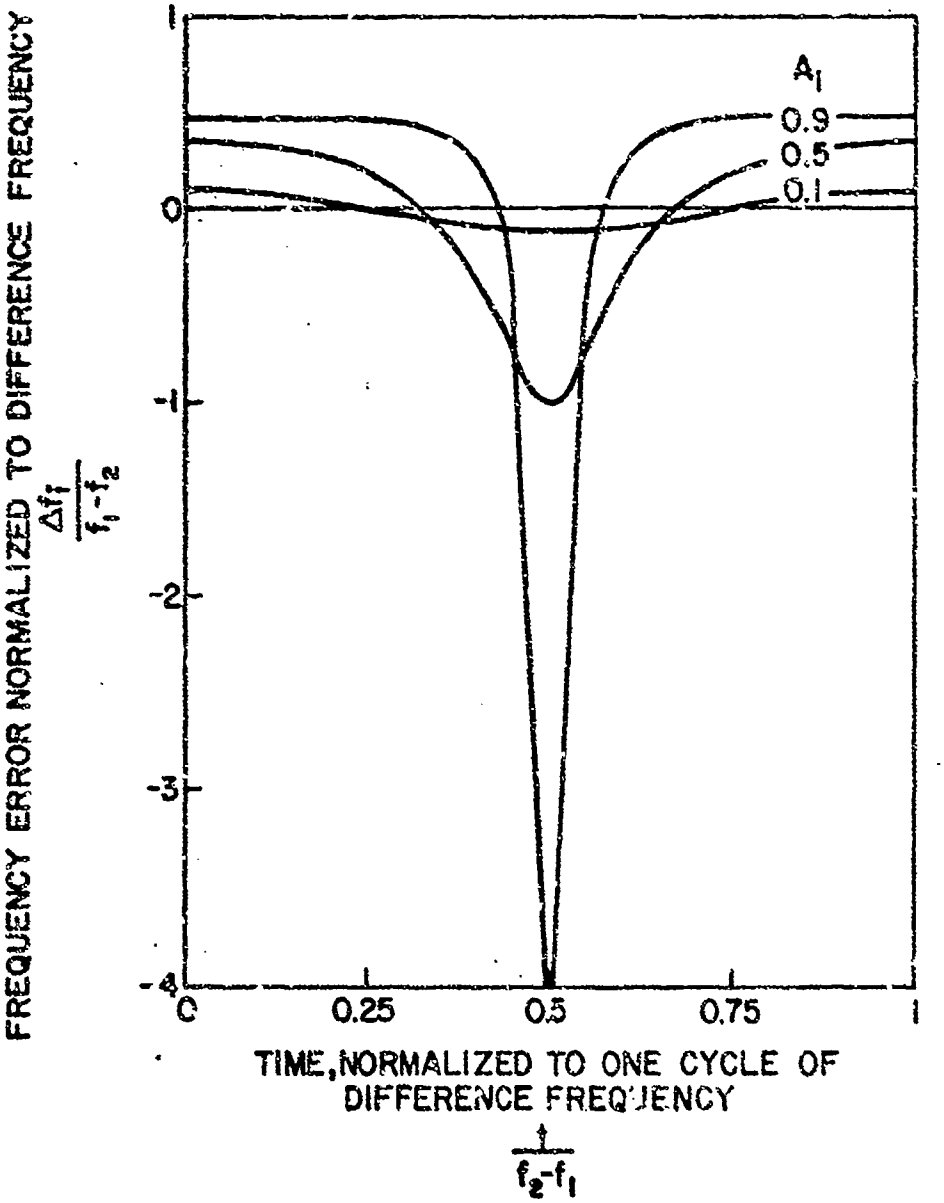


FIGURE 2.6 FREQUENCY ERROR WAVEFORM VERSUS TIME FOR VARIOUS INTERFERENCE SIGNAL AMPLITUDES.

of fundamental frequency $(f_2-f_1)$, we can conclude that the time-averaged frequency error, $\Delta f_i$, is zero. Furthermore, for $A_i$ less than $\frac{1}{2}$, the RMS frequency error, $(\Delta f)_{iRMS}$, is well approximated by $(f_2-f_1)A_i/\sqrt{2}$.

For values of $A_i$ less than or equal to $\frac{1}{2}$, the instantaneous frequency error does not exceed the linear operating region of the discriminator. Filtering of the discriminator output, therefore, will eliminate the zero-mean fluctuating component $\Delta f_i$, and tracking behavior will not be impaired. For $A_i$ greater than $\frac{1}{2}$, however, the excursions in $\Delta f_i$ exceed the linear region of the discriminator, and the time-averaged frequency output will be biased so that it lies somewhat closer to the interfering signal frequency. Thus, a signal-to-interference ratio which produces $A_i = \frac{1}{2}$ may be considered the threshold for successful tracking. In this threshold region, the approximations in equations (2.14) and (2.15) do not hold. Based on Baghdady's [1961] exact results, this threshold occurs for $(S/I)_{IF} = 2.5$ dB.

The results of the preceding analyses may be summarized as follows:

a. the tracking technique requires a signal-to-noise power ratio in the IF bandwidth of at least 0 dB;

b. white noise causes a fluctuating frequency error $\Delta f_n$ of zero mean and RMS value $\frac{BW_{IF}}{\sqrt{(S/N)_{IF}}}$;

c. the tracking technique requires a signal-to-interference power ratio in the IF bandwidth of at least 2.5 dB; and

d. Coherent interference at frequency $f_2$ causes an error in tracking frequency $f_1$, denoted by $\Delta f_i$, of zero mean and RMS value $\frac{f_2 - f_1}{2.8\sqrt{(S/I)_{IF}}}$.

## B. THE ANTENNA SYSTEM AND THE INCIDENT WAVE

### 1. Wave Fields and Polarization

Consider the general incident wave described in Equation (1.2) and Fig. 1.1. Transforming to the x,y,z ground coordinate system, the six field components are

$$
\begin{aligned}
E_x &= E_1 \left[ (-\sin\alpha - jR\cos\alpha)(\sin\theta) + (\cos\alpha - jR\sin\alpha)(-\sin\beta\cos\theta) \right] \\
E_y &= E_1 \left[ (-\sin\alpha - jR\cos\alpha)(-\cos\theta) + (\cos\alpha - jR\sin\alpha)(-\sin\beta\sin\theta) \right] \\
E_z &= E_1 \left[ (\cos\alpha - jR\sin\alpha)(-\cos\beta) \right] \qquad (2.18) \\
H_x &= E_1/\eta \left[ (\cos\alpha - jR\sin\alpha)(\sin\theta) + (\sin\alpha + jR\cos\alpha)(-\sin\beta\cos\theta) \right. \\
H_y &= E_1/\eta \left[ (\cos\alpha - jR\sin\alpha)(-\cos\theta) + (\sin\alpha + jR\cos\alpha)(-\sin\beta\sin\theta) \right. \\
H_z &= E_1/\eta \left[ (\sin\alpha + jR\cos\alpha)(-\cos\beta) \right.
\end{aligned}
$$

If an antenna system were constructed consisting of three orthogonal electric field sensors and three orthogonal magnetic field sensors to measure the field components, the instantaneous power flow in the wave could be calculated, theoretically, as the Poynting vector,

$$
\begin{aligned}
P_x &= E_y H_z - E_z H_y \\
P_y &= E_z H_x - E_x H_z \qquad (2.19) \\
P_z &= E_x H_y - E_y H_x .
\end{aligned}
$$

Measurement of the elevation angle of arrival is of limited value because of the presence of earth-ionosphere reflections. To find the azimuthal angle of arrival, only the first two components, $P_x$ and $P_y$, need be determined. however, the equations still require all six field components to be measured. Practical direction-finders for ground-based use omit several of the antennas, implying the assumption that the omitted field components are small. Typically, a system consisting of crossed loops and a vertical electric antenna will be employed, measuring $E_z$, $H_x$, and $H_y$. Then

$$\begin{aligned} P_x &\cong -E_z H_y \\ P_y &\cong E_z H_x \quad . \end{aligned} \tag{2.20}$$

assuming either $H_z$ is small, or both $E_x$ and $E_y$ are small; these conditions are realized with a purely vertical polarization (in the traditional sense, that is, electric field in the plane of incidence) for the wave. The success of this system for direction-finding on ground-wave signals from vertically polarized transmitters supports this assumption. When ionospherically reflected waves are received, however, the polarization may not be purely vertical; the estimates of $P_x$ and $P_y$ from the three field components are incorrect, and the error is referred to as polarization error. Working backward from the observed polarization error on a signal transmitted with vertical polarization from a known direction of arrival, Horner [1957] found that the received polarization for a 100-km path during skywave conditions

Very few data are available concerning the received polarization of VLF whistlers and emissions. Researchers [Delloue, 1960; Crary, 1961] have reported that the polarization is random or rapidly varying. Crary [1961] performed a detailed simulation covering propagation of a whistler from its duct exit point at the lower edge of the ionosphere, through the earth-ionosphere waveguide, to a ground based receiving site. His results for the polarization also show wide variability as a function of frequency and path distance. In studying his plots, however, the general observation can be made that the polarization ellipse will tend to have an axis ratio of about $\frac{1}{2}$, and that the handedness of the whistler polarization in the duct is preserved. The conclusion drawn is that the direction-finder design selected should be one which produces the minimum possible polarization error over the entire range of received polarization.

2. Antenna Elements for Field Component Measurements.

At very low frequencies, the antennas which can be practically constructed for direction-finding are electrically very small compared with the wavelengths involved. While the efficiency of such antennas may be low, the radiation patterns of small dipoles and loop are theoretically perfect. When used as a receiving antenna, the small dipole is sensitive only to the electric field along the dipole axis; the small loop is sensitive to the magnetic field perpendicular to the plane of the loop.

A considerable amount of controversy has existed concerning the relative merits of loops and dipoles for VLF reception. One consideration is sensitivity of the receiving system, which will depend on the efficiency with which the antenna extracts energy from the incident wave and couples it to the preamplifier. Papers clarifying this controversy have been published by Wheeler [1946] and Franks [1964]. In theory, the available power from any small antenna, loop or dipole, of any size less than $\lambda/2\pi$, is the same for a given incident wave power density. In practice, this amount of power is never extracted due to the difficulty of presenting the antenna with a conjugate-matched load impedance and due to losses in the antenna and matching circuit conductors. The impedance of the small antenna is primarily reactive, with the radiation resistance representing only a small part of the impedance. A useful figure of merit suggested by Wheeler is the quantity p, where

$$p = \frac{R_{rad}}{X_{ant.}} , \qquad (2.21)$$

which is the ratio of the radiation resistance to the antenna reactance. It is indicative of the antenna efficiency which can be achieved with practical coupling techniques. In Figs. 2.7 and 2.8, the impedance and efficiency characteristics of small dipoles and loops as a function of their size are described. Most interestingly, the value of p is identical for both antennas when the dipole length is equal to the loop diameter.

Another consideration which has been advanced is the relative immunity to noise pickup of the two types of antennas. "Noise pickup" may be of two

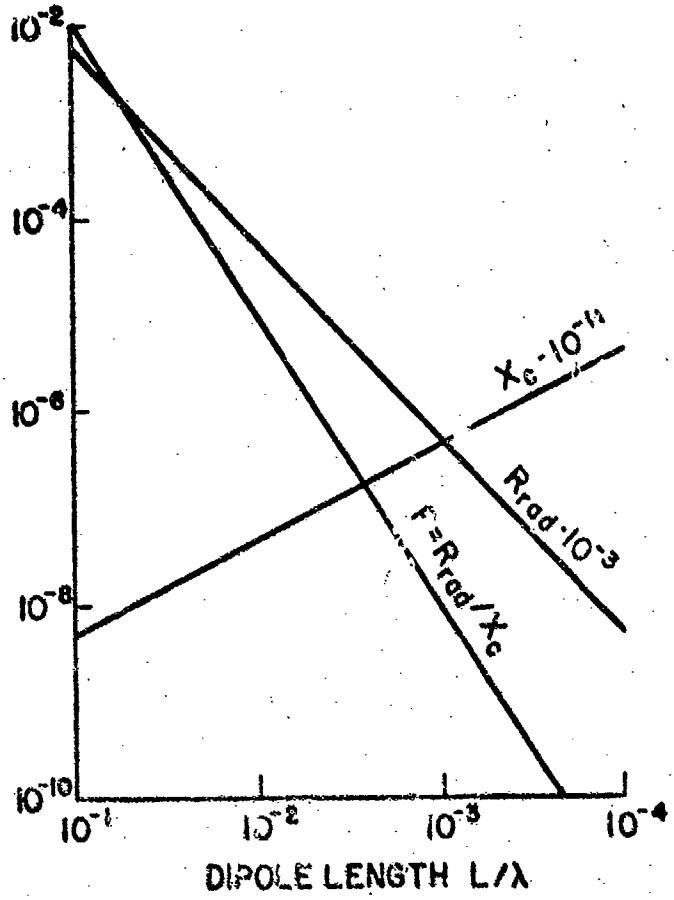


FIGURE 2.7 RADIATION RESISTANCE, CAPACITIVE REACTANCE, AND PRACTICAL EFFICIENCY OF SMALL DIPOLES AS A FUNCTION OF THEIR LENGTH.

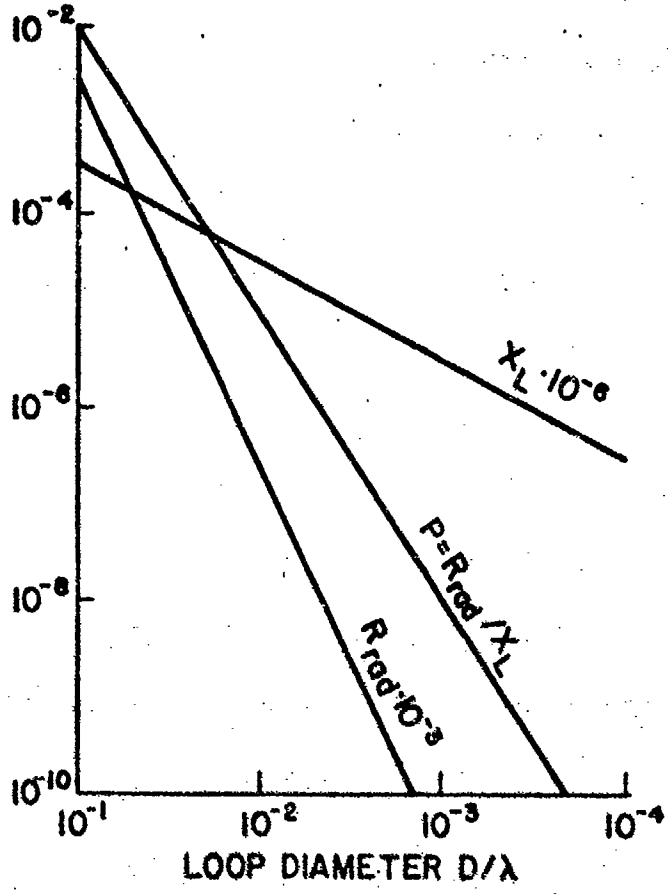


FIGURE 2.8 RADIATION RESISTANCE, INDUCTIVE REACTANCE, AND PRACTICAL EFFICIENCY OF SMALL LOOPS AS A FUNCTION OF THEIR DIAMETER.

types: first, nearby sources of noise may capacitively or inductively couple undesired energy into the antenna; second, there may be direct collisions of charged particles with the antenna element. Practical experience indicates that the electric field antenna, or dipole, is more severely affected by both types of noise pickup. In particular, the author has witnessed incidents in which a cloud passing directly overhead caused very high potentials to develop across a vertical electric antenna's terminals, causing arcing and rendering its output useless, while loop antennas at the same location were unaffected. There are possibilities for controlling noise, both by shielding of manmade sources and by providing weakly conducting dielectric shields to reduce particle impingement.

3. Antenna Axis Perturbations and Site Effects.

The sensitive axis of a dipole or loop may differ from the intended direction for mechanical or electrical reasons. Mechanical misalignment of the antennas produces a predictable change: the direction-finding errors so produced are analyzed in Section II.C.4. Electrical causes of axis disturbance are more subtle in nature. All conductors in the vicinity of the antennas respond to the incident waves also, creating electric and magnetic fields which can couple into the antennas capacitively or inductively. Any imbalance in the construction of the antennas and preamplifiers reduces the immunity of the antenna to such stray potentials and currents.

Measurement of the incident electric field presents particular problems due to the influence of the cables used to carry power to the antenna

preamplifiers or signals away from the antennas. The dipoles must be perfectly balanced and the cables led away orthogonally, or else the potential induced on the cable bundle by the incident wave will couple into the dipole causing a response to an undesired component ($E_x$ in Fig. 2.9a) of the field. For the vertical electrical dipole measuring $E_z$, this balance is almost impossible to achieve in practice. As illustrated in Fig. 2.9(a) the capacitance between the lower dipole arm and ground will unavoidably be greater than that between the upper arm and ground; as a result, the charge distribution induced on the long feedline cable bundle by the $E_x$ field component shown will induce a greater potential on the upper arm than the lower arm, and the difference will appear as a voltage across the dipole terminals. Another approach is the "monopole" antenna design shown in Fig. 2.9(b). Since the grounding process is imperfect at best, the imaging plane displays a much lower resistance along the direction of the feedline than in other radial directions; as a result the monopole's image is skewed and the equivalent axis of the dipole is tilted, again making it sensitive to $E_x$. These two approaches make up most existing antenna installations for VLF observations of electric fields. Although the installation illustrated in Fig. 2.9(c) would be expected to reduce the problem, practical considerations dictate the desirability of a system which can operate with existing antenna installations. Consideration of the problems introduced by imperfect measurement of $E_z$ is given in Section II.C.5.

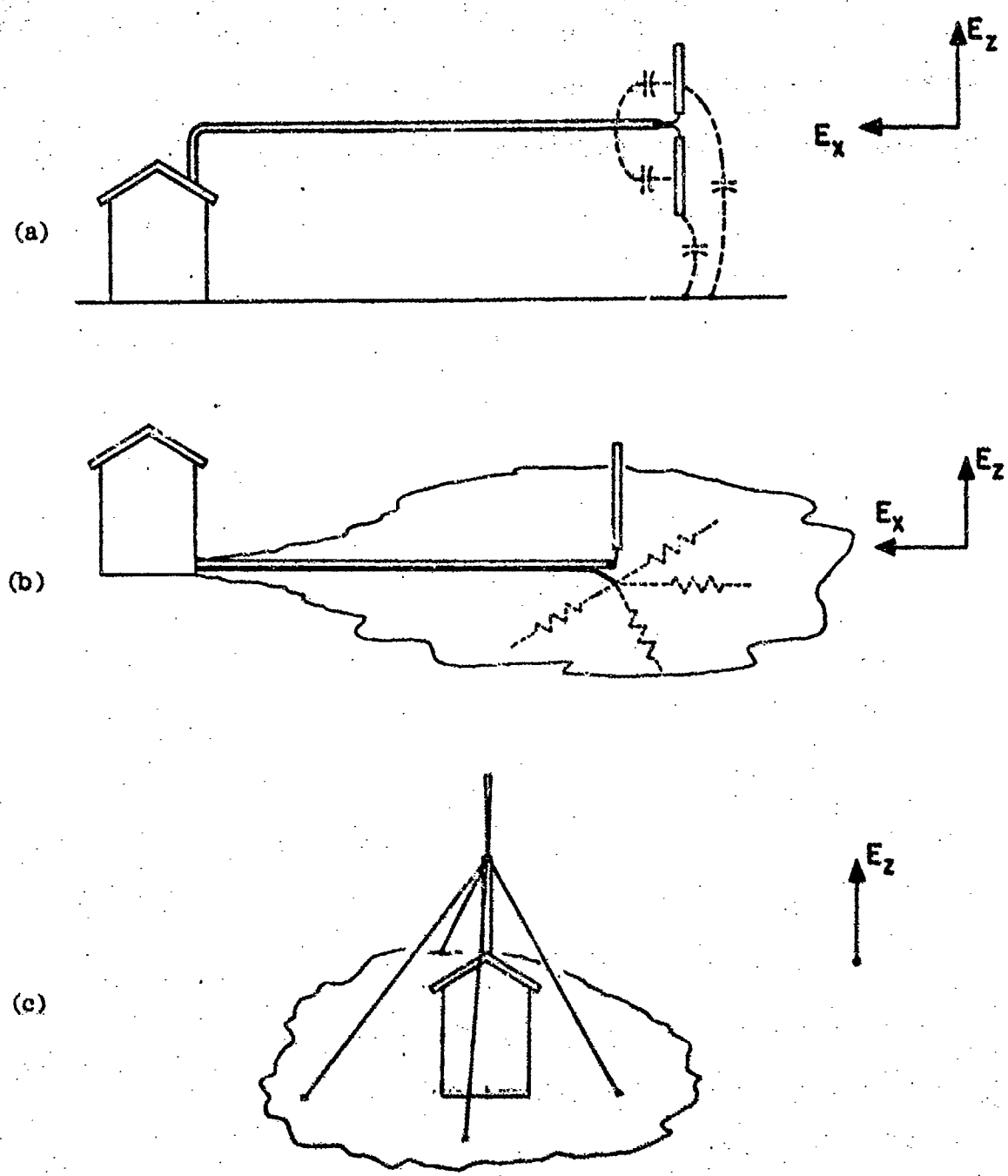


FIGURE 2.9 VERTICAL ELECTRIC ANTENNA APPROACHES AND PROBLEMS. (a) Elevated vertical dipole. Unbalance due to presence of ground causes coupling to feedline potential, and sensitivity to $E_x$. (b) Ground based monopole. Finite ground resistance causes lowest resistance path to exist along feedline shield, tilting dipole equivalent axis, causing sensitivity to $E_x$. (c) Monopole with complete symmetry maintained in grounding and nearby objects. Power lines will destroy symmetry. Sensitive only to $E_z$.

One more source of error in the direction-finder is "site" error. These errors are not really part of the instrumentation, as they represent deviations in the direction of propagation of the wave, and even a theoretically perfect direction-finder would be affected. One of the more familiar forms of error is the coastal refraction effect, which is associated with the discontinuity between highly conducting seawater and poorly conducting ground. Kukes and Starik [1962] state that this form of error is less than $1^{\circ}$ at wavelengths greater than 3000 meters (100 kHz). Other possible sources of error are inhomogeneities in the earth conductivity and sloping ground. Inasmuch as these errors are dependent on the site, the most appropriate solution is to perform a calibration of the site using emitters at known bearing angles, determining the measurement errors, and fitting a curve to the error as a function of angle.

## C. DIRECTION-FINDING SIGNAL PROCESSING

### 1. Analysis of New Technique.

The new technique for determining direction of arrival from the signals from the small-aperture antenna system consists of computing the time-averaged Poynting vector components in the x- and y-directions, and resolving the direction of arrival as the reverse† of the Poynting vector. Stated mathematically, the Poynting vector estimates are

†The reversal is due to the fact the direction of arrival is taken to mean the bearing to the signal source rather than the direction of signal propagation.

$$\hat{P}_x = -E_z H_y \qquad \hat{P}_y = E_z H_x, \tag{2.22}$$

(where the symbol "^" denotes an estimated quantity), and the time-averaged values of the Poynting vectors are therefore

$$\hat{\bar{P}}_x = \frac{1}{4}\left[E_z H_y^* + E_z^* H_y\right] \quad \hat{\bar{P}}_y = \frac{1}{4}\left[E_z H_x^* + E_z^* H_x\right] . \tag{2.23}$$

From these estimates of the average power flow in the x- and y-directions, the direction of arrival is the reverse of the Poynting vector, or[†]

$$\hat{\theta} = \angle\left(-\hat{\bar{P}}_x - j\hat{\bar{P}}_y\right) . \tag{2.24}$$

This new technique differs from existing VLF direction-finding methods because nonlinear operations, that is, cross-multiplications between the antenna signals, are performed. This is made possible by the real time multichannel filtering action provided by the frequency-tracking loop; without prefiltering, such nonlinear operations would produce massive intermodulation between all the spectral components present, obscuring the desired information unless an extremely high signal-to-noise ratio were present.

[†]The use of the imaginary operator "j" here is not to be confused with its usual application in the representation of sinusoidally time-varying quantities. In equation (2.24), the complex quantity $-\hat{\bar{P}}_x - j\hat{\bar{P}}_y$ represents a vector in space; the positive real axis coincides with the x (north) direction and the positive imaginary axis lies along the y (east) direction. Complex notation is a mathematically convenient means for composing a vector from two orthogonal components; the angle of the vector relative to the reference axis is given by taking the complex argument ($\angle$). This representation is superior to the conventional arctangent function which contains a $180^\circ$ ambiguity and which can only be used to represent angles over a $\pm 90^\circ$ range unless a special note is made to examine the signs of the numerator and denominator forming the argument of the function.

The implementation of the signal processing technique will now be discussed. Since all three input signals are mixed with a common local oscillator signal, the phase and amplitude relationships of the signals are preserved during the translation to the intermediate frequency. The IF voltages are denoted by $V_1$, $V_2$, and $V_3$. Since, as discussed in Section II.B.2, the efficiencies of comparably sized loops and dipoles are equal, these voltages must be given by

$$V_1 = E_z \qquad V_2 = \eta H_x \qquad V_3 = \eta H_y \quad (e^{j\omega_{IF}t} \text{ assumed}) \tag{2.25}$$

The cross-multiplications and angle resolution are performed in a novel manner in the hardware. By applying the channel 1 ($E_z$) signal to an amplitude limiter, the phase information is extracted in binary form; the binary limiter output is then digitally multiplied with a binary "scanning" signal before application to controlling inversion switches in the two loop signal channels. A discussion of the hardware in detail is reserved for Section III; for purposes of analysis, the process can be modeled as shown in Fig. 2.10(a) and (b).†

The cross-multiplication operations in Fig. 2.10(a) yield the instantaneous Poynting vector estimates; low-pass filtering removes the twice-IF component. Thus,

†The effects of the amplitude limiter will be considered, however, when noise or interference are present.

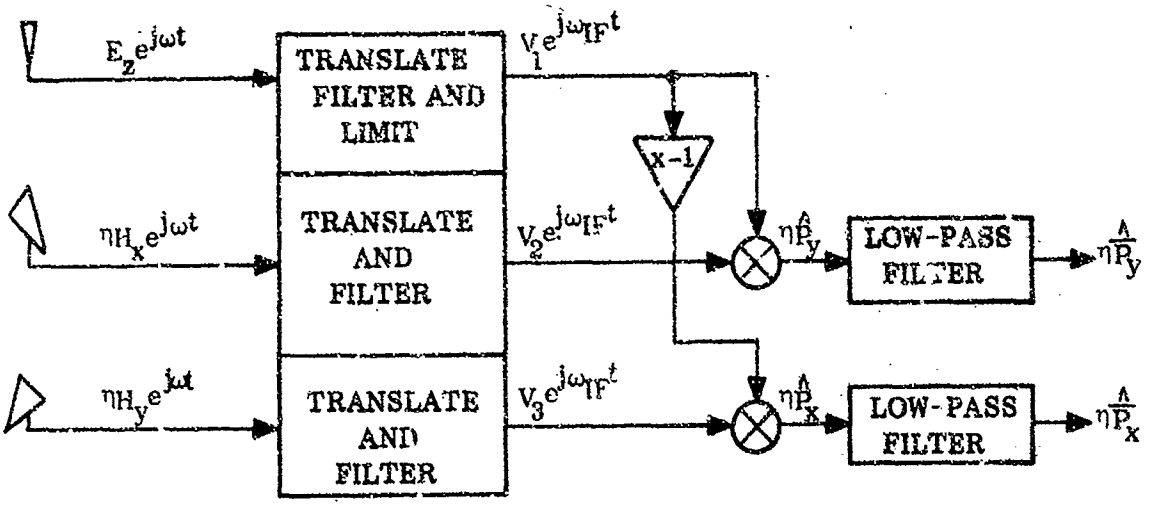


(a)

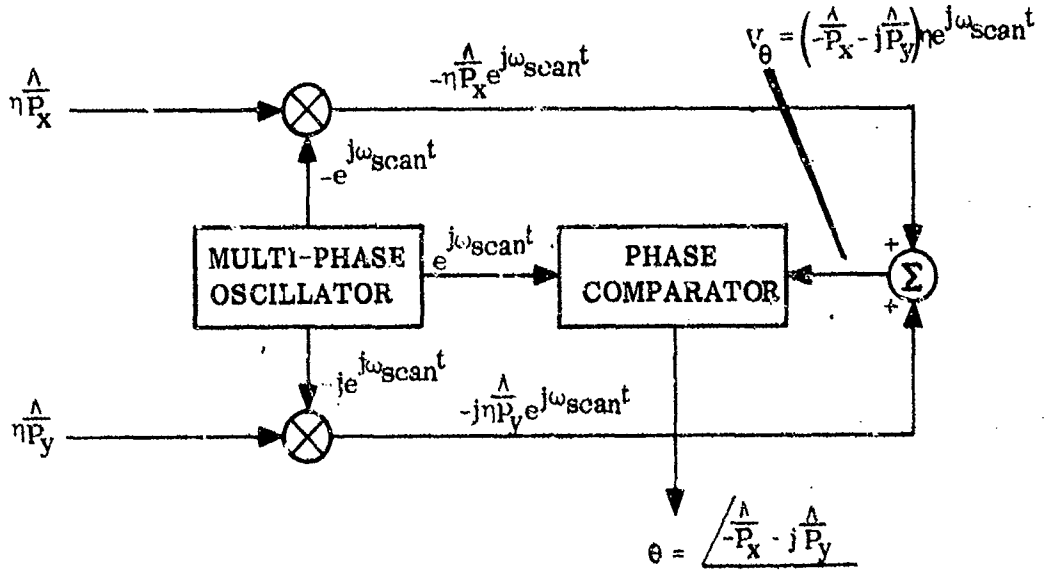


(b)

FIGURE 2.10 MODEL OF SIGNAL PROCESSING PERFORMED TO COMPUTE THE DIRECTION OF ARRIVAL FROM THE WAVE MEASUREMENTS. (a) Model of signal processing to compute the time-averaged Poynting vector components from the antenna signals. (b) Model of signal processing to resolve the direction of arrival angle from the time-averaged Poynting vector components.

$$\eta\hat{\bar{P}}_x = -\tfrac{1}{4}\left[V_1 V_3^* + V_1^* V_3\right]$$

$$\eta\hat{\bar{P}}_y = \tfrac{1}{4}\left[V_1 V_2^* + V_1^* V_2\right]. \tag{2.26}$$

These voltages are then multiplied by the scanning signals as in Fig. 2.10(b), and summed to produce a signal of

$$V_\theta = -\eta\hat{\bar{P}}_x e^{j\omega_{scan}t} - j\eta\hat{\bar{P}}_y e^{j\omega_{scan}t}. \tag{2.27}$$

This voltage is compared in phase to the scanning carrier $e^{j\omega_{scan}t}$. Then,

$$\hat{\theta} = \angle\left(-\eta\hat{\bar{P}}_x e^{j\omega_{scan}t} - j\eta\hat{\bar{P}}_y e^{j\omega_{scan}t}\right) - \angle\left(e^{j\omega_{scan}t}\right) \tag{2.28}$$

which is equivalent to

$$\hat{\theta} = \left[\angle\left(-\eta\hat{\bar{P}}_x - j\eta\hat{\bar{P}}_y\right)\right] + \omega_{scan}t - \omega_{scan}t,$$

thus, the desired relation of (2.24) has been implemented,

$$\hat{\theta} = \angle\left(\hat{\overline{P}}_x - j\hat{\overline{P}}_y\right) .$$

To demonstrate the validity of the computations, let us temporarily assume an incident wave at angle $\theta$, purely vertically polarized so that $\alpha = 0$ and $R = 0$. The field quantities in equations (2.18) now reduce to

$$\begin{aligned} E_z &= -E_1 \cos\beta \\ H_x &= E_1/\eta \sin\theta \\ H_y &= -E_1/\eta \cos\theta \end{aligned} \qquad (2.29)$$

and the IF voltages are

$$\begin{aligned} V_1 &= -E_1 \cos\beta \\ V_2 &= E_1 \sin\theta \\ V_3 &= -E_1 \cos\theta . \end{aligned} \qquad (2.30)$$

The cross-multiplications produce

$$\eta\hat{\bar{P}}_x = -\tfrac{1}{2} E_1^2 \cos\beta\cos\theta$$
$$\eta\hat{\bar{P}}_y = -\tfrac{1}{2} E_1^2 \cos\beta\sin\theta \qquad (2.31)$$

and the angle resolution produces

$$\hat{\theta} = \angle\tfrac{1}{2}E_1^2 \cos\beta\,(\cos\theta + j\sin\theta), \qquad (2.32)$$

or

$$\hat{\theta} = \theta \qquad (2.33)$$

The technique provides a unique, unambiguous indication of the direction of arrival. The causes of error in $\hat{\theta}$ will now be investigated.

2. Errors Due to Noise and Interference.

The effects of internally generated noise in the equipment provide an ultimate limitation to the direction-finder sensitivity for weak signals. The total noise contributions in each channel may be lumped into an additive noise voltage, denoted by $n_1(t)$, $n_2(t)$, and $n_3(t)$ for the three channels. These three voltages are independent, originating in separate processes, but they

may all be considered to have Gaussian statistics, with zero mean, and identical mean-squared values:

$$\overline{n_1(t)} = \overline{n_2(t)} = \overline{n_3(t)} = 0$$

$$\overline{n_1^2(t)} = \overline{n_2^2(t)} = \overline{n_3^2(t)} = \overline{n^2(t)} \tag{2.34}$$

To analyze the effects of these noise voltages, we can adopt a model for narrow-band noise presented by Panter [1965] containing independent Gaussian components in quadrature at the center frequency of the band. The noise voltages at the IF circuitry are thus represented by

$$n(t) = n_c(t)e^{j\omega_{IF}t} + jn_s(t)e^{j\omega_{IF}t} \tag{2.35}$$

where $n_c(t)$ and $n_s(t)$ are slowly varying compared to $e^{j\omega_{IF}t}$, and for which

$$\overline{n_c^2(t)} = \overline{n_s^2(t)} = \overline{n^2(t)}. \tag{2.36}$$

It is desirable to express $\overline{n^2(t)}$ in terms of the signal-to-noise power ratio in the IF. To avoid ambiguity due to the fact that the signal varies with the incident wave geometry, we will define $(S/N)_{IF}$ to be the signal-to-noise ratio which would exist on a comparable, but nondirectional, receiving system. Then.

$$V = E_1 \quad (e^{j\omega_{IF}t} \text{ assumed})$$

and the signal power is

$$S = E_1^2/2.$$

The noise power is given by $\overline{n^2(t)}$, and therefore

$$(S/N)_{IF} = E_1^2/2\overline{n^2(t)}$$

and

$$\overline{n^2(t)} = E_1^2/2(S/N)_{IF} \tag{2.37}$$

(Hereafter, the time-dependence of $n$, $n_c$, $n_s$ will be implicit.) The IF voltages resulting from the combination of signal and noise can now be written

$$\begin{aligned} V_1 &= E_z + n_{c1} + jn_{s1} \\ V_2 &= \eta H_x + n_{c2} + jn_{s2} \\ V_3 &= \eta H_y + n_{c2} + jn_{s3}, \end{aligned} \tag{2.38}$$

($e^{j\omega_{IF}t}$ assumed for all quantities)

and, for vertical polarization of the incident wave, ($\alpha = 0^o$, R = 0), we have

$$\begin{aligned} V_1 &= -E_1 \cos\beta + n_{c1} + jn_{s1} \\ V_2 &= E_1 \sin\theta + n_{c2} + jn_{s2} \\ V_3 &= -E_1 \cos\theta + n_{c3} + jn_{s3} \end{aligned} \tag{2.39}$$

At this point we must taken into account the fact that a limiter amplifier is included in channel 1. As discussed in Section II.A.2, the noise is reduced in the presence of the signal when $(S/N)_{IF} > 1$, according to the formula of (2.10),

$$(S/N)_{LIM} = 2(S/N)_{IF}.$$

We must therefore modify $n_{c1}$ and $n_{s1}$ in $V_1$ by the factor $1/\sqrt{2}$. Proceeding with the cross-multiplications of $V_1$ with $V_3$ and $V_1$ with $V_2$, and the low-pass filtering, we derive

$$\eta \hat{\bar{P}}_x = -\frac{1}{2}\left[E_1^2 \cos\beta \cos\theta - (1/\sqrt{2})\, E_i \cos\theta\, n_{ci} - E_i \cos\beta\, n_{c3} \ldots\right.$$

$$\left. \ldots + (1/\sqrt{2})\, n_{c1}\, n_{c3} + (1/\sqrt{2}) n_{s1}\, n_{s3}\right] \qquad (2.40)$$

$$\eta \hat{\bar{P}}_y = \frac{1}{2}\left[-E_1^2 \cos\beta \sin\theta + (1/\sqrt{2})\, E_1 \sin\theta\, n_{c1} - E_1 \cos\beta\, n_{c2} \ldots\right.$$

$$\left. \ldots + (1/\sqrt{2})\, n_{c1}\, n_{c2} + (1/\sqrt{2}) n_{s1}\, n_{s2}\right].$$

Resolving the direction of arrival using equation (2.24) we have, after some rearranging,

$$\hat{\theta} = \frac{\frac{1}{2}\left[(E_1^2 \cos\beta - \frac{1}{\sqrt{2}} E_1 n_{c1})(\cos\theta + j \sin\theta) \quad \ldots\right.}{\left. \ldots + (\frac{1}{\sqrt{2}} n_{c1} - E_1 \cos\beta)(n_{c3} - jn_{c2}) + (\frac{1}{\sqrt{2}} n_{s1})(n_{s3} - jn_{s2})\right]} \qquad (2.41)$$

Now, knowing that the noise components are all Gaussian distributions, we can express them each as the product of independent unit-variance Gaussian distributions, $n_{u1}$, $n_{u2}$, etc., and the root-mean-square of the desired distribution, that is,

$$n_{c1}(t) = \sqrt{\overline{n_{c1}^2(t)}} \cdot n_{u1}(t) \ , \quad \text{etc.}$$

Using this approach and equation (2.37), the angle $\hat{\theta}$ can be expressed as

$$\hat{\theta} = \angle\left[\left(\cos\beta - \frac{n_{u1}}{2\sqrt{(S/N)}}\right)e^{j\theta} - \left(\frac{\cos\beta}{\sqrt{2(S/N)}} + \frac{n_{u1}}{2\sqrt{2}\,(S/N)}\right)(n_{u2} - jn_{u3}) \cdots \right.$$
$$\left. \cdots + \left(\frac{n_{u4}}{2\sqrt{2}\,(S/N)}\right)(n_{u5} - jn_{u6})\right] . \tag{2.42}$$

The vectors $(n_{u2} - jn_{u3})$ and $(n_{u4} - jn_{u5})$ are random in phase, and therefore we can transform them into two new vectors $(n_{u6}e^{j\theta} - jn_{u7}e^{j\theta})$ and $(n_{u8}e^{j\theta} - jn_{u9}e^{j\theta})$ without harm. Then the angle may again be rewritten:

$$\hat{\theta} = \angle\left[\cos\beta\left(1 - \frac{n_{u6}}{\sqrt{2(S/N)}}\right) - n_{u1}\left(\frac{1}{2\sqrt{(S/N)}} + \frac{n_{u6}}{2\sqrt{2}(S/N)}\right) \cdots \right.$$
$$\cdots + n_{u4}\left(\frac{n_{u8}}{2\sqrt{2}(S/N)}\right)\Big]e^{j\theta} + je^{j\theta}\left[\left(\frac{\cos\beta}{\sqrt{2(S/N)}} + \frac{n_{u1}}{2\sqrt{2}(S/N)}\right)\right.$$
$$\left. \cdots - \left(\frac{n_{u4}}{2\sqrt{2}(S/N)}\right)n_{u9}\right] . \tag{2.43}$$

Expressing this as

$$Ae^{j\hat{\theta}} = Be^{j\theta} + Ce^{j(\pi/2+\theta)} \tag{2.44}$$

and dividing by $Be^{j\theta}$ (assuming $B > 0$),

$$(A/B)e^{j(\hat{\theta}-\theta)} = 1 + (C/B)e^{j\pi/2}, \tag{2.45}$$

the angle error $\Delta\theta = \hat{\theta}-\theta$ is given by

$$\Delta\theta = \angle 1 + (C/B)e^{j\pi/2} = \arctan (C/B) \tag{2.46}$$

or

$$\Delta\theta = \arctan \left[ \frac{\frac{n_{u7}}{\sqrt{2}\ (S/N)} + \frac{n_{u1}\ n_{u7} - n_{u4}\ n_{u9}}{2\sqrt{2}\cos\beta\ (S/N)}}{1 + \frac{-2n_{u6} - \sqrt{2}\ n_{u1}}{2\sqrt{2}\cos\beta\sqrt{(S/N)}} + \frac{-n_{u1}\ n_{u6} + n_{u4}\ n_{u8}}{2\sqrt{2}\cos\beta\ (S/N)}} \right] \tag{2.47}$$

From this expression we can see that the error has a zero mean. To determine the RMS error, a computer simulation was performed using random number generators shaped to have Gaussian distributions. These results are shown in Figure 2.11. For high signal-to-noise ratio conditions, the error can be approximated by:

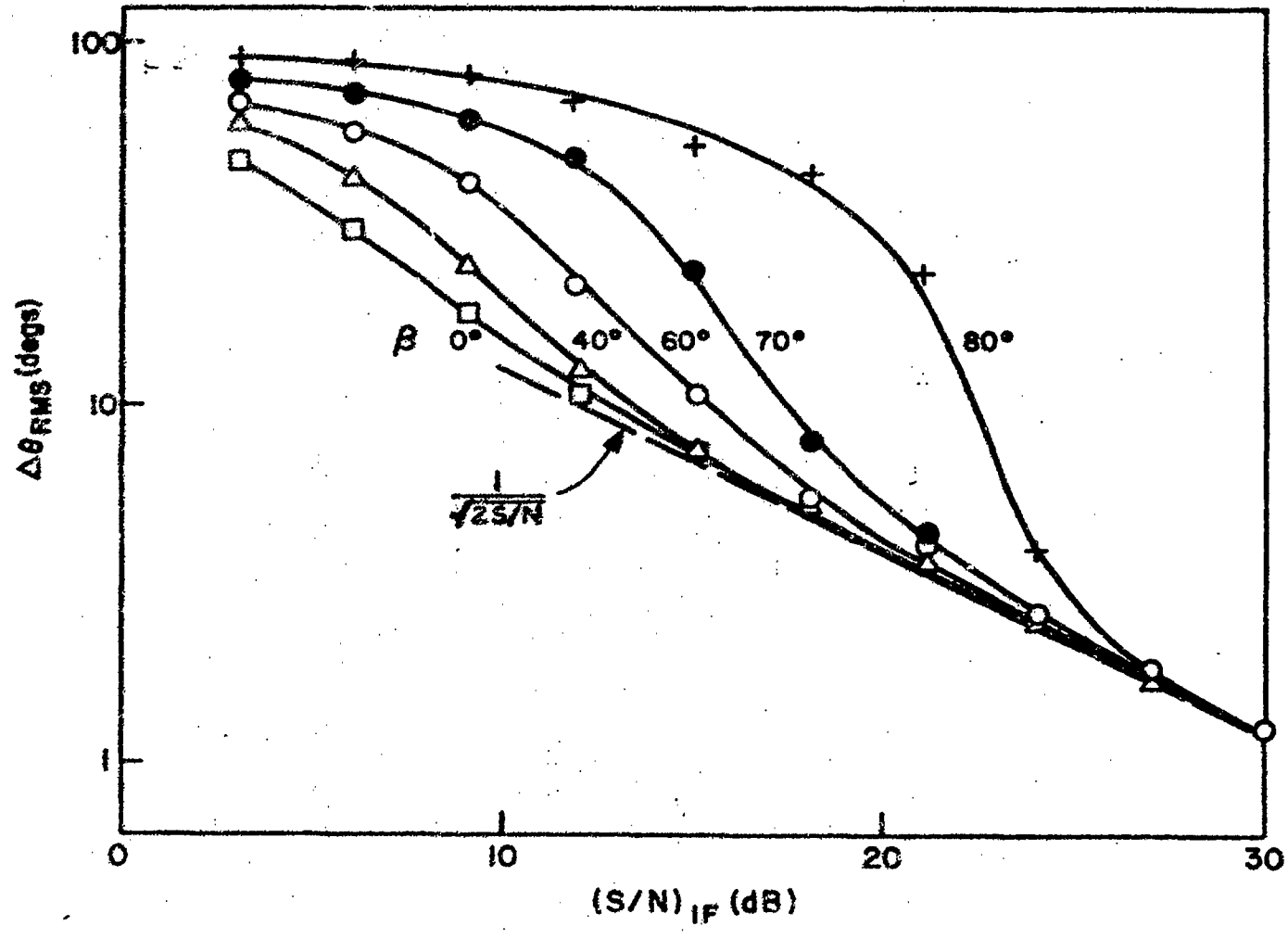


FIGURE 2.11 RMS DIRECTION-FINDING ERROR VERSUS SIGNAL-TO-NOISE RATIO WHICH WOULD BE PRODUCED ON A COMPARABLE, BUT NONDIRECTIONAL, RECEIVING SYSTEM.

$$\Delta\theta = \frac{n_{u7}}{\sqrt{2(S/N)}}$$

and therefore

$$\Delta\theta_{RMS} = \frac{1}{\sqrt{2(S/N)}} \quad . \tag{2.48}$$

We will now consider instead the effects of a second coherent signal within the receiver passband. The ratio of the desired signal power to the interfering signal power is denoted by $(S/I)_{IF}$, and the difference frequency between the two signals by $f_d$. Whereas the azimuthal angle of arrival of the desired signal is $\theta$, the angle of arrival of the interference will be $\theta + \theta_d$; the elevation angle of the desired signal is $\beta$, and the elevation angle of the interfering signal is $\beta_i$.

The amplitude of the interfering signal can be calculated as:

$$E_i = E_1 / \sqrt{(S/I)_{IF}} \tag{2.49}$$

and the signals in the IF are therefore given by ($e^{j\omega_{IF}t}$ assumed for all quantities)

$$V_1 = -E_1 \cos\beta - E_1 \frac{\cos\beta_1}{\sqrt{(S/I)_{IF}}} e^{j\omega_d t}$$

$$V_2 = E_1 \sin\theta + E_1 \frac{\sin(\theta+\theta_d)}{\sqrt{(S/I)_{IF}}} e^{j\omega_d t} \qquad (2.50)$$

$$V_3 = -E_1 \cos\theta - E_1 \frac{\cos(\theta+\theta_d)}{\sqrt{(S/I)_{IF}}} e^{j\omega_d t} \quad .$$

At this point we must again take into account the presence of the limiter amplifier included in the cross-multiplication circuitry. Incorporating the S/N enhancement from equation (2.15) and performing the cross-multiplications, we have

$$\eta\hat{\bar{P}}_x = -\frac{1}{2}\left[E_1^2 \cos\beta\cos\theta + E_1^2 \cos\beta\cos(\theta+\theta_d)\frac{\cos\omega_d t}{\sqrt{(S/I)_{IF}}} \cdots\right.$$

$$\cdots + E_1^2 \cos\beta_1\cos\theta\frac{\cos\omega_d t}{2\sqrt{(S/I)_{IF}}} + E_1^2\cos\beta_1\cos(\theta+\theta_d)\cdots$$

$$\left.\cdots\times\frac{1}{2(S/I)_{IF}}\right] \qquad (2.51)$$

$$\eta\hat{\bar{P}}_y = -\frac{1}{2}\left[-E_1^2 \cos\beta \sin\theta - E_1^2 \cos\beta \sin(\theta+\theta_d)\frac{\cos\omega_d t}{\sqrt{(S/I)_{IF}}} \cdots\right.$$

$$\cdots -E_1^2 \cos\beta_1 \sin\theta \frac{\cos\omega_d t}{2\sqrt{(S/I)_{IF}}} - E_1^2 \cos\beta_1 \sin(\theta+\theta_d) \cdots$$

$$\left.\cdots \times \frac{1}{2\,(S/I)_{IF}}\right]. \qquad \text{(2.51 cont.)}$$

The resolution of these quantities into an estimated angle $\hat{\theta}$ gives

$$\hat{\theta} = \angle\left[\cos\beta + \cos\beta_1 \frac{\cos\omega_d t}{2\sqrt{(S/I)_{IF}}}\right] e^{j\theta} + \left[\cos\beta \frac{\cos\omega_d t}{\sqrt{(S/I)_{IF}}} \cdots\right.$$

$$\left.\cdots + \cos\beta_1 \frac{1}{2\,(S/I)_{IF}}\right] e^{j(\theta+\theta_d)} \qquad (2.52)$$

Expressing this as

$$Ae^{j\hat{\theta}} = Be^{j\theta} + Ce^{j(\theta+\theta_d)} \qquad (2.53)$$

and dividing by $Be^{j\theta}$, (assuming $\frac{\cos\beta_i}{2\cos\beta\sqrt{S/I)}} < 1$),

$$(A/B)e^{j(\hat{\theta}-\theta)} = 1 + (C/B)e^{j\theta_d t} ; \qquad (2.54)$$

thus, the angle error $\Delta\theta = \hat{\theta}-\theta$, is given by

$$\Delta\theta = \angle 1 + (C/B)e^{j\theta_d t} \qquad (2.55)$$

or

$$\Delta\theta = \angle\left[1 + \left[\frac{\frac{\cos\beta_i}{2\cos\beta\,(S/I)} + \frac{\cos\omega_d t}{\sqrt{(S/I)}}}{1 + \frac{\cos\beta_i}{2\cos\beta}\frac{\cos\omega_d t}{\sqrt{(S/I)}}}\right] e^{j\theta_d t}\right] . \qquad (2.56)$$

From this expression we can see that the error contains both a non-zero mean value and a periodic variation at the difference frequency $f_d$. The character of $\Delta\theta$ versus time is illustrated in Fig. 2.12 for some representative conditions. The mean error $\overline{\Delta\theta}$ and the RMS variation about the mean for various conditions are plotted in Fig. 2.13.

Approximations can also be made which provide a simpler indication of the effects of interference. For high signal-to-interference ratio conditions, the error is well approximated by

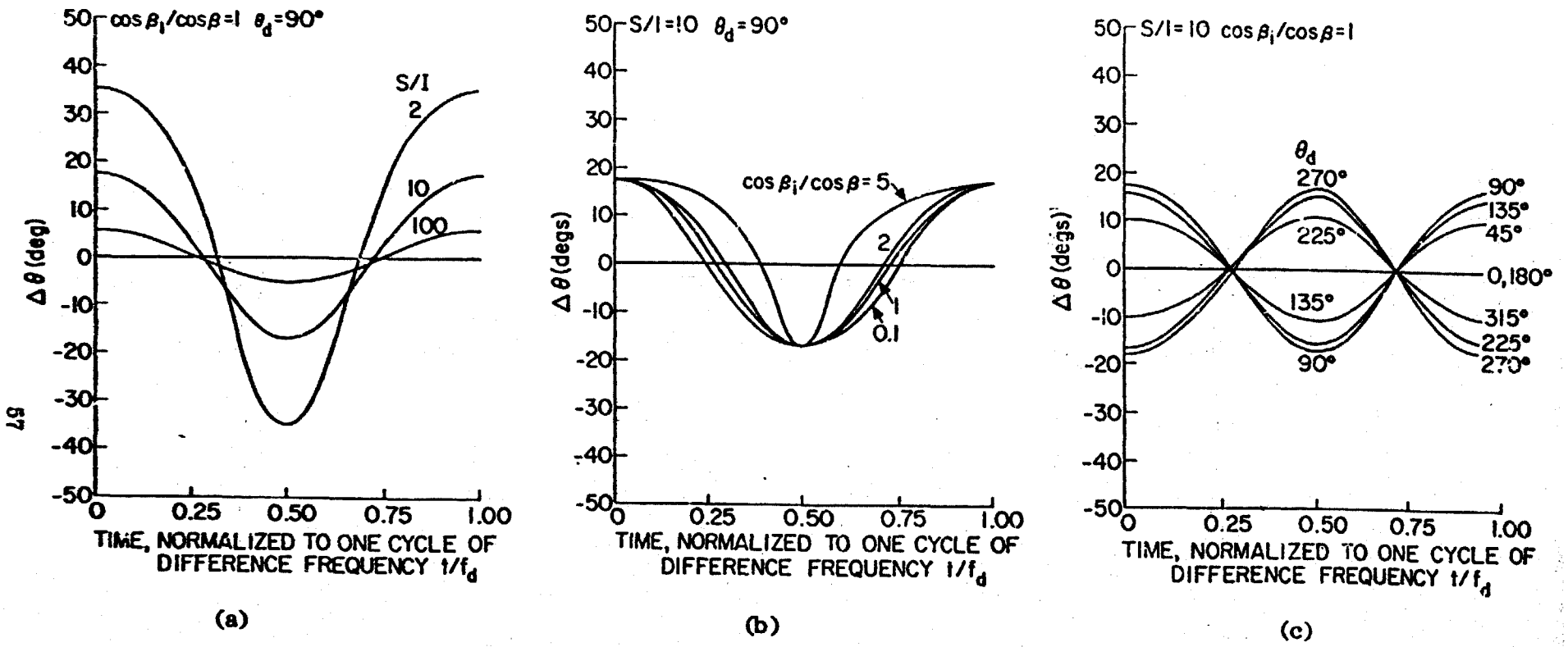


**FIGURE 2.12 DIRECTION-FINDING ERROR VERSUS TIME FOR VARIOUS (a) SIGNAL TO INTERFERENCE RATIOS; (b) ELEVATION ANGLE RATIOS; (c) RELATIVE INTERFERING SIGNAL BEARINGS.**

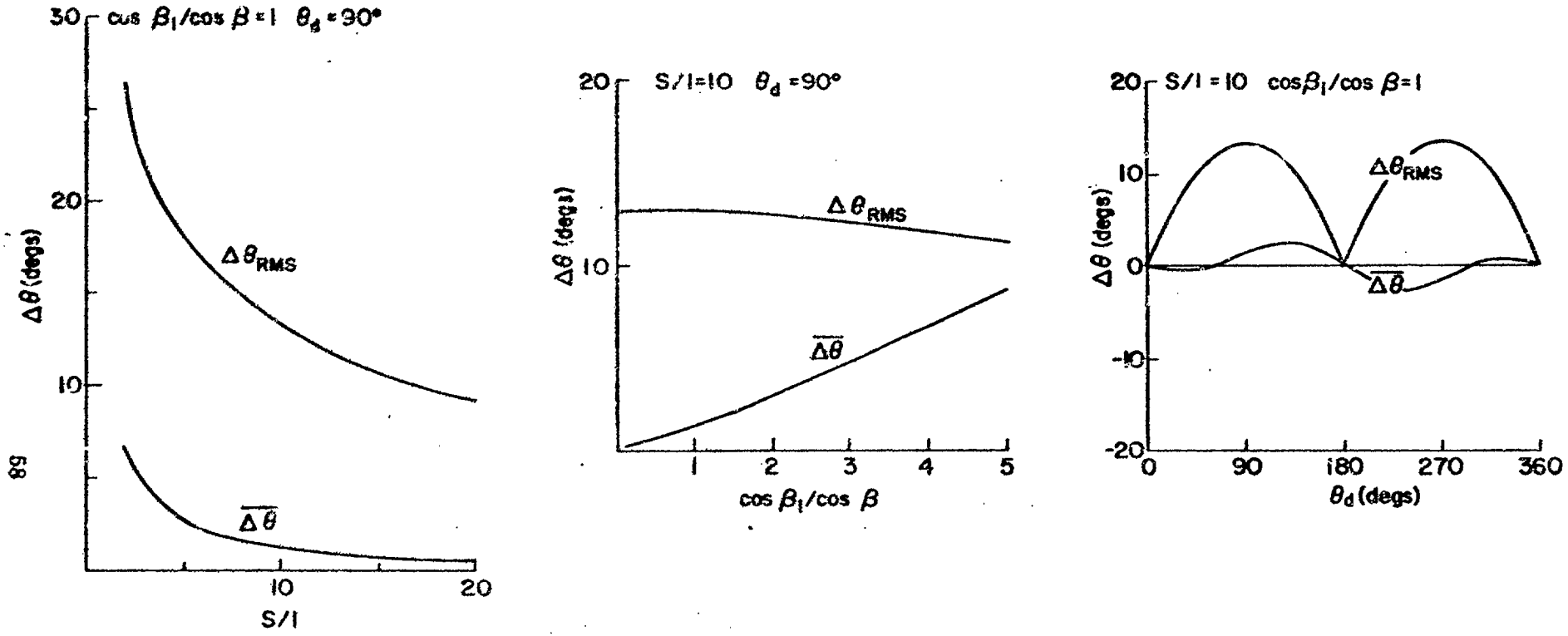


FIGURE 2.13 MEAN AND RMS DIRECTION-FINDING ERROR VERSUS (a) SIGNAL-TO-INTERFERENCE RATIO; (b) ELEVATION ANGLE RATIO: (c) RELATIVE INTERFERING SIGNAL BEARING .

$$\Delta\theta = \left[ \frac{\cos \beta_i}{2 \cos \beta \, (S/I)} + \frac{\cos \omega_d t}{\sqrt{(S/I)}} \right] \sin \theta_d \qquad (2.57)$$

demonstrating that,

$$\overline{\Delta\theta} = \frac{\cos \beta_i}{2 \cos \beta \, (S/I)} \sin \theta_d \qquad (2.58)$$

and

$$\Delta\theta_{RMS} = \frac{1}{\sqrt{2 \, (S/I)}} \left| \sin \theta_d \right| . \qquad (2.59)$$

### 3. Polarization Error

To this point in the analysis we have restricted the polarization of the incident wave to purely vertical. When this condition is relaxed, the estimates of the Poynting vector components $\hat{P}_x$ and $\hat{P}_y$ based only on measurement of $E_z$, $H_x$, and $H_y$ may be incorrect, and the computed angle of arrival may contain an error known as polarization error.

Let $\alpha$ and R take on nonzero values so that a general polarization is permitted. The fields from equations (2.18) are measured by the antennas, and presented as IF voltages ($e^{j\omega_{IF}t}$ assumed),

$$V_1 = E_1 (\cos\alpha - jR \sin\alpha)(-\cos\beta)$$

$$V_2 = E_1 (\cos\alpha - jR \sin\alpha)(\sin\theta) + (\sin\alpha + jR\cos\alpha)(-\sin\beta\cos\theta)$$

$$V_3 = E_1 (\cos\alpha - jR \sin\alpha)(-\cos\theta) + (\sin\alpha + jR\cos\alpha)(-\sin\beta\sin\theta)$$

The cross-multiplications then yield

$$\eta\hat{\bar{P}}_x = -\frac{1}{2} E_1^2 \cos\beta \left[(\cos^2\alpha + R^2\sin^2)(\cos\theta) \ldots \right.$$

$$\left. \ldots + (1-R^2)(\cos\alpha\sin\alpha)(\sin\beta\sin\theta)\right] \qquad (2.60)$$

$$\eta\hat{\bar{P}}_y = \frac{1}{2} E_1^2 \cos\beta \left[(\cos^2\alpha + R^2\sin^2\alpha)(-\sin\theta) \ldots \right.$$

$$\left. \ldots + (1-R^2)(\cos\alpha\sin\alpha)(\sin\beta\cos\theta)\right]$$

Resolving this into an angle $\hat{\theta}$,

$$\hat{\theta} = \sqrt{\left[(\cos^2\alpha + R^2\sin^2\alpha)\right]e^{j\theta} + \left[\sin\beta\,(R^2-1)\cos\alpha\sin\alpha\right]e^{j(\theta+\pi/2)}} \qquad (2.61)$$

and expressing this as

$$Ae^{j\hat{\theta}} = Be^{j\theta} + Ce^{j(\theta+\pi/2)}$$

we divide by $Be^{j\theta}$ ($B \neq 0$, providing a polarization other than pure linear horizontal is assumed),

$$(A/B)\, e^{j(\hat{\theta}-\theta)} = 1 + (C/B)\, e^{j\pi/2}$$

or

$$\Delta\theta = \underline{/1 + (C/B)\, e^{j\pi/2}} = \arctan\,(C/B)$$

so the polarization error is given by

$$\Delta\theta = \arctan\left[\frac{\sin\beta\,(R^2-1)\cos\alpha\,\sin\alpha}{\cos^2\alpha + R^2\sin^2\alpha}\right] \qquad (2.62)$$

The polarization error as a function of R, $\beta$, and $\alpha$ is plotted in Fig. 2.14. For purposes of comparison, the polarization error of the goniometer system, based on the analysis of Bullough and Sagredo [1973], is plotted in adjacent frames. The advantage of the new technique is evidenced by lower errors, especially for high elevation angles and polarizations near circular.

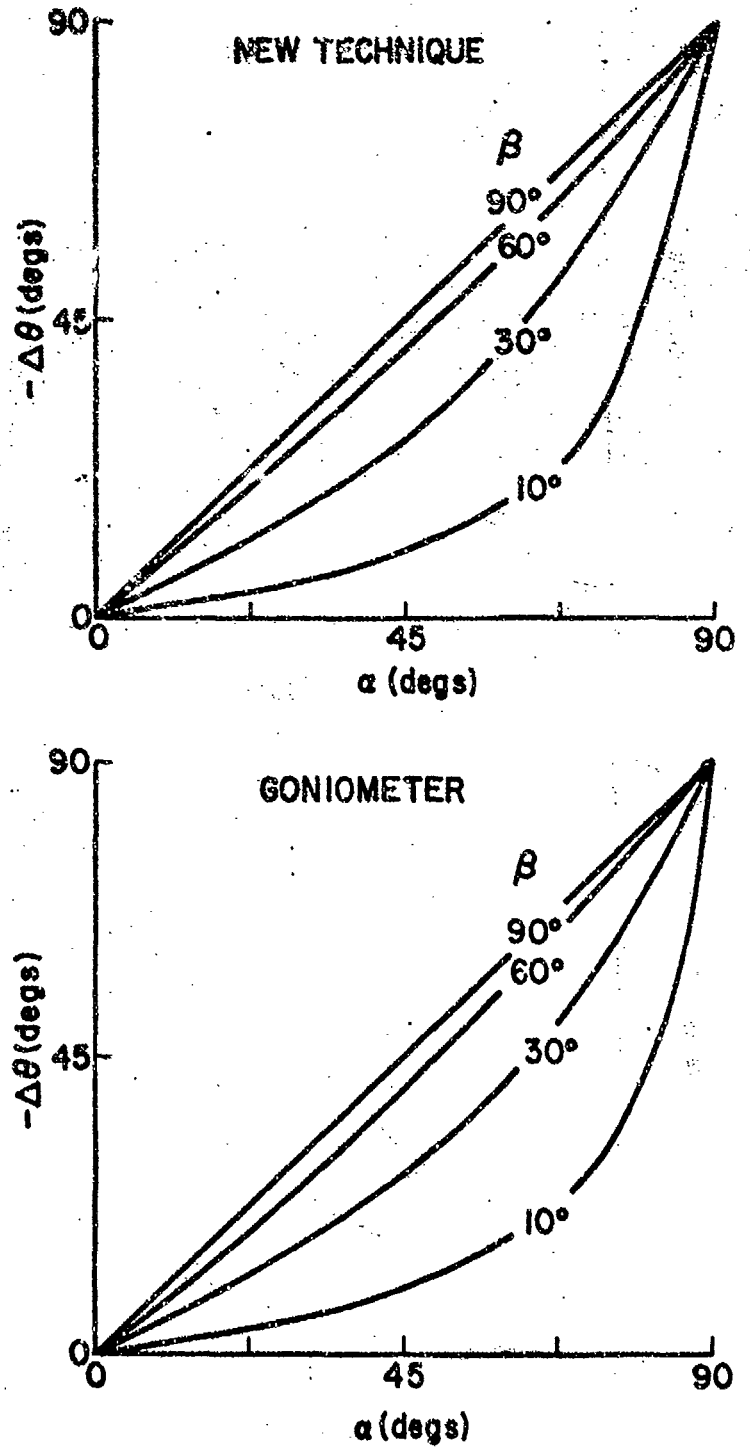


FIGURE 2.14(a). POLARIZATION ERROR FOR NEW TECHNIQUE AND CONVENTIONAL GONIOMETER AS A FUNCTION OF ELEVATION ANGLE AND POLARIZATION ELLIPSE AXIS TILT FOR R = 0.

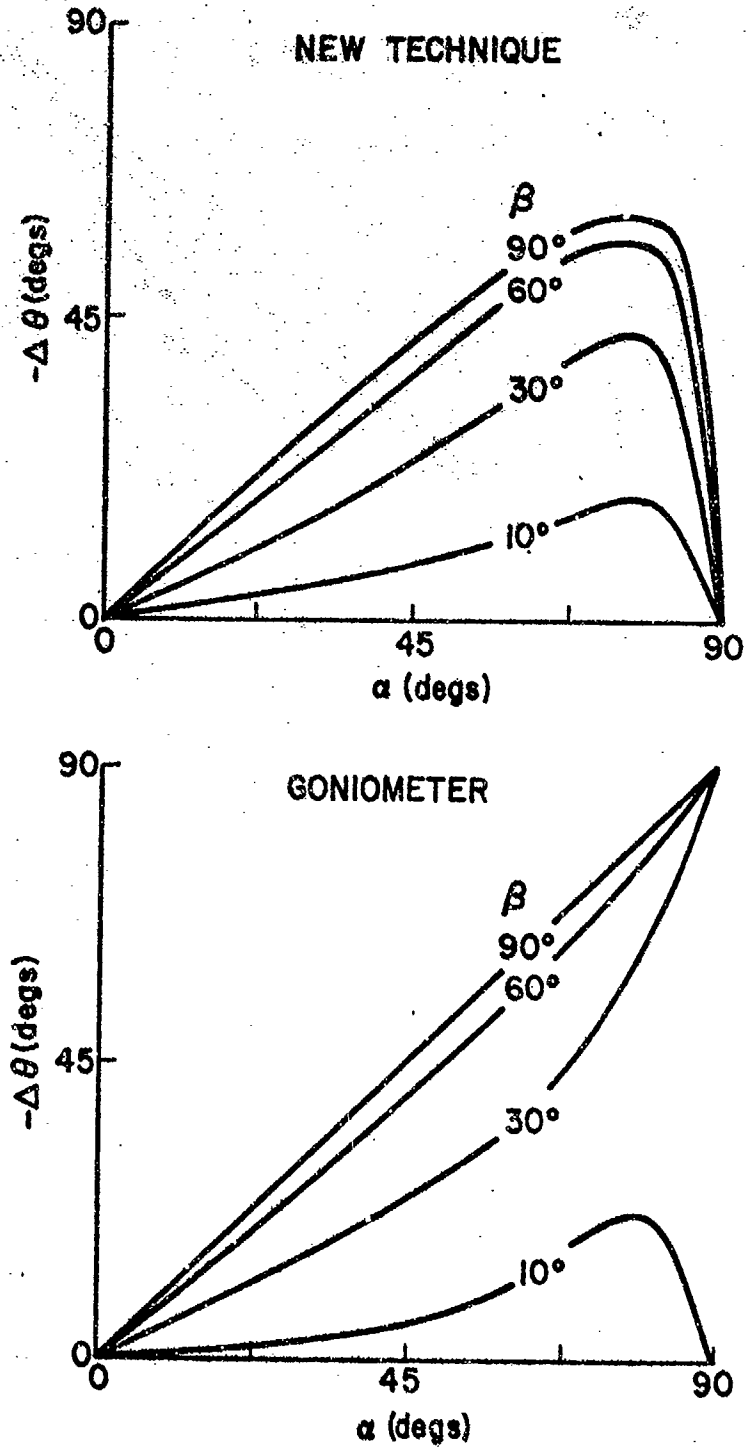


FIGURE 2.14(b). POLARIZATION ERROR FOR NEW TECHNIQUE AND CONVENTIONAL GONIOMETER AS A FUNCTION OF ELEVATION ANGLE AND POLARIZATION ELLIPSE AXIS TILT, FOR R = ½.

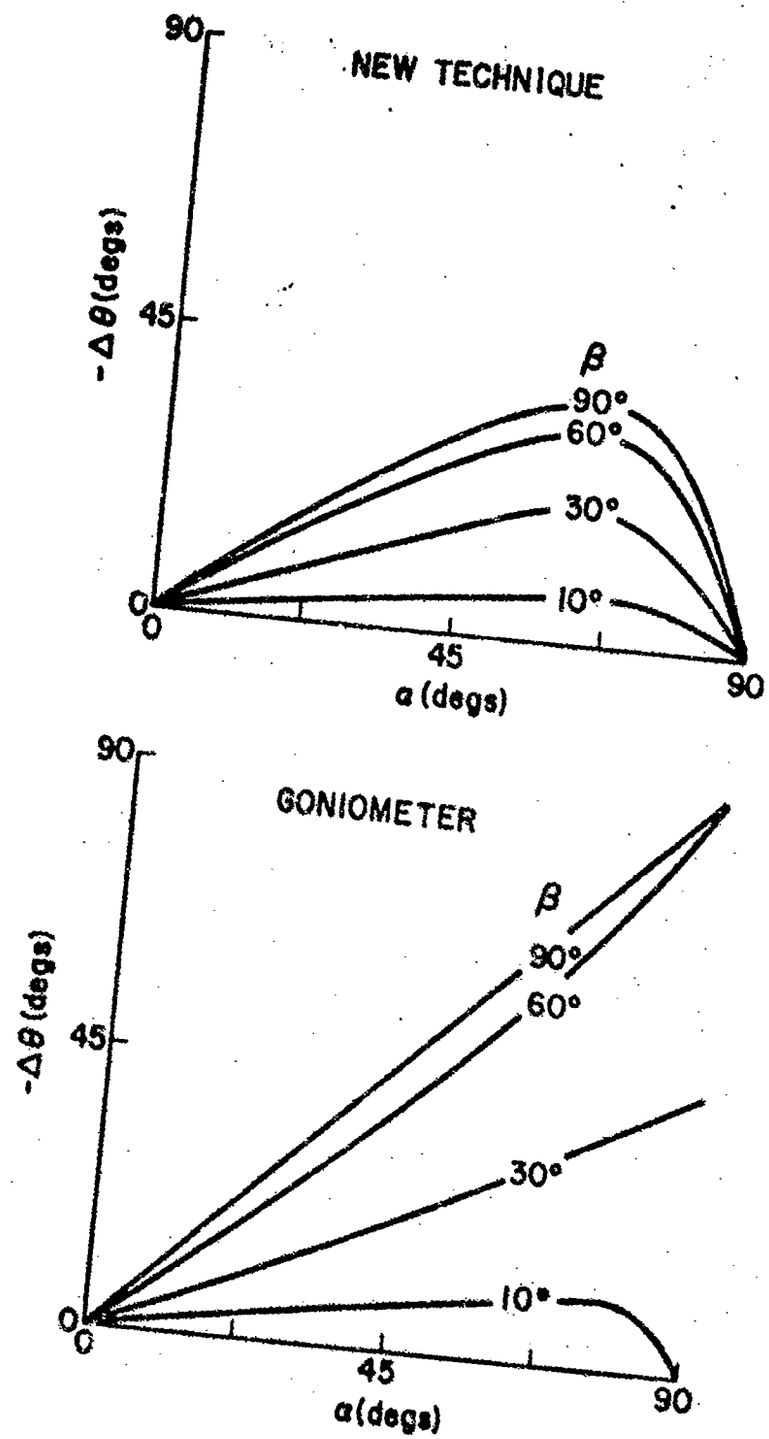


FIGURE 2.14(c). POLARIZATION ERROR FOR NEW TECHNIQUE AND CONVENTIONAL GONIOMETER AS A FUNCTION OF ELEVATION ANGLE AND POLARIZATION ELLIPSE AXIS TILT, FOR R = ½.

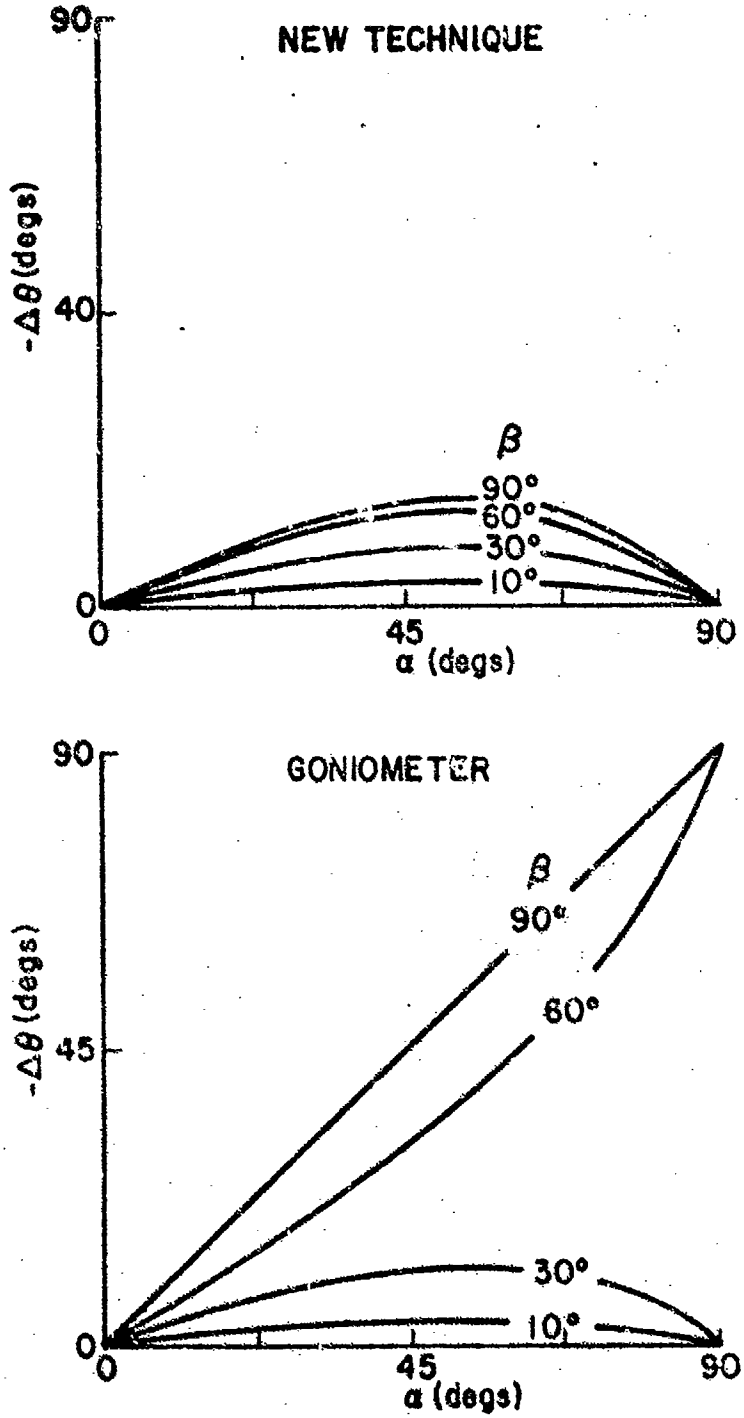


FIGURE 2.14(d). POLARIZATION ERROR FOR NEW TECHNIQUE AND CONVENTIONAL GONIOMETER AS A FUNCTION OF ELEVATION ANGLE AND POLARIZATION ELLIPSE AXIS TILT, FOR R = 3/4.

4. Antenna Misalignment Errors.

In Section II.B.3 it was pointed out that the sensitive axes of the antennas may differ from the desired directions. Consider a system of antennas where the antennas measuring $H_x$ and $H_y$ are misaligned, because of mechanical or electrical asymmetries, so that the sensitive axes are perturbed. Referring to Fig. 2.15, the projections of the misaligned axes on the xy plane are displaced by angles $\delta$ and $\epsilon$ (in radians). Now the fields measured by the antennas are in error, as follows:

$$\begin{aligned} \hat{H}_x &= H_x \cos\delta + H_y \sin\delta \\ \hat{H}_y &= H_y \cos\epsilon - H_x \sin\epsilon \ . \end{aligned} \tag{2.63}$$

Substituting the actual fields from equations (2.18), and assuming $\alpha = 0$ and $R = 0$ for simplicity, the IF voltages will be given by

$$\begin{aligned} V_1 &= -E_1 \cos\beta \\ V_2 &= E_1 \sin\theta \cos\delta - E_1 \cos\theta \sin\delta \\ V_3 &= -E_1 \cos\theta\cos\epsilon - E_1 \sin\theta\sin\epsilon \ . \end{aligned} \tag{2.64}$$

The cross-multiplications then yield,

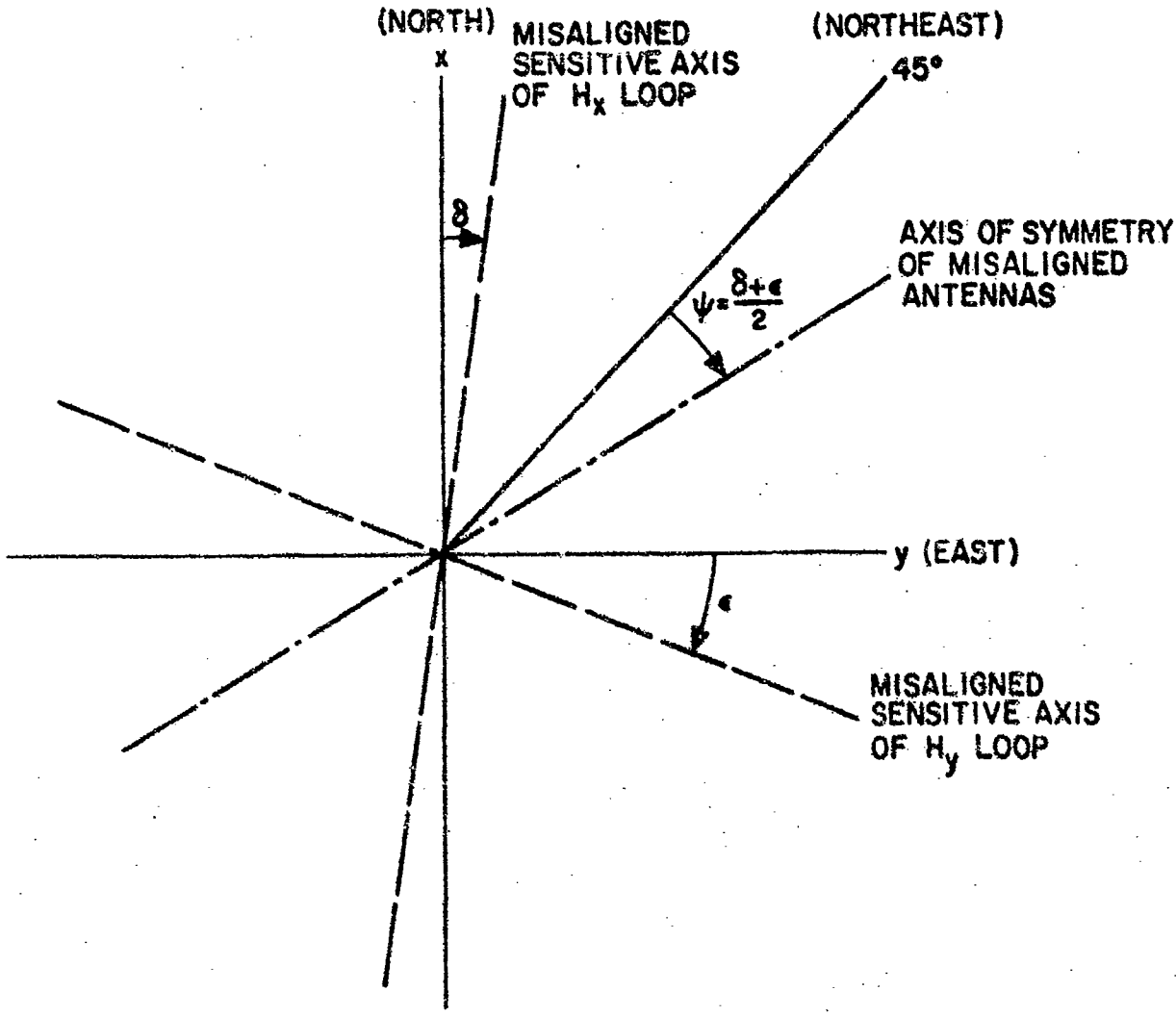


FIGURE 2.15 PLAN VIEW OF HORIZONTAL PLANE SHOWING MISALIGNMENT IN SENSITIVE AXES OF LOOP ANTENNAS

$$\eta\hat{\overline{P}}_x = -\tfrac{1}{2}E_1^2 (\cos\beta \cos\theta \cos\epsilon + \cos\beta \sin\theta \sin\epsilon)$$

$$\eta\hat{\overline{P}}_y = \tfrac{1}{2}E_1^2 (-\cos\beta \sin\theta \cos\delta + \cos\beta \cos\theta \sin\delta)$$

Resolving the angle, and assuming $\delta$ and $\epsilon$ are small, $\cos\delta$, $\cos\epsilon \cong 1$,

$$\hat{\theta} = \underline{/e^{j\theta} + \sin\epsilon \sin\theta - j\sin\delta \cos\theta} . \qquad (2.65)$$

Denote two new angles $\psi$ and $\chi$ as follows:

$$\psi = (\epsilon + \delta)/2$$
$$\chi = (\epsilon - \delta)/2 \qquad (2.66)$$

Note that $\psi$ is the rotation of the axis of symmetry of the antennas due to the misalignment, and $\chi$ is the misalignment of the y-axis antenna relative to the new axis of symmetry. With these quantities,

$$\hat{\theta} = \underline{/e^{j\theta} + \sin(\chi+\psi) \sin\theta + j \sin(\chi-\psi) \cos\theta}$$

and using trigonometric identities,

$$\hat{\theta} = \underline{/e^{j\theta} + \sin\chi \cos\psi\, je^{-j\theta} - \sin\psi \cos\chi\, je^{j\theta}} .$$

Since $\psi$ and $\chi$ are small

$$\hat{\theta} = \angle\left(e^{j\theta} + \chi e^{j(\pi/2 - \theta)} + \psi e^{j(\theta - \pi/2)}\right) \quad (2.67)$$

Expressing this as

$$Ae^{j\hat{\theta}} = e^{j\theta} + j\chi e^{-j\theta} - j\psi e^{j\theta}$$

and dividing by $e^{j\theta}$,

$$Ae^{j(\hat{\theta}-\theta)} = 1 + j\chi e^{-j2\theta} - j\psi \quad .$$

we can see that for $\chi$ and $\psi$ small,

$$\hat{\theta}-\theta = \chi \cos 2\theta - \psi$$

or

$$\Delta\theta = -\psi + \chi \cos 2\theta \quad (2.68)$$

The mean value corresponds to the misalignment of the axis of symmetry. The periodic (quadrantal) component has a peak value corresponding to the misalignment of the y-axis antenna relative to the axis of symmetry.

Now consider a misalignment of the loop antennas corresponding to non-horizontality of the equivalent axes of the loops, as shown in Fig 2.16.

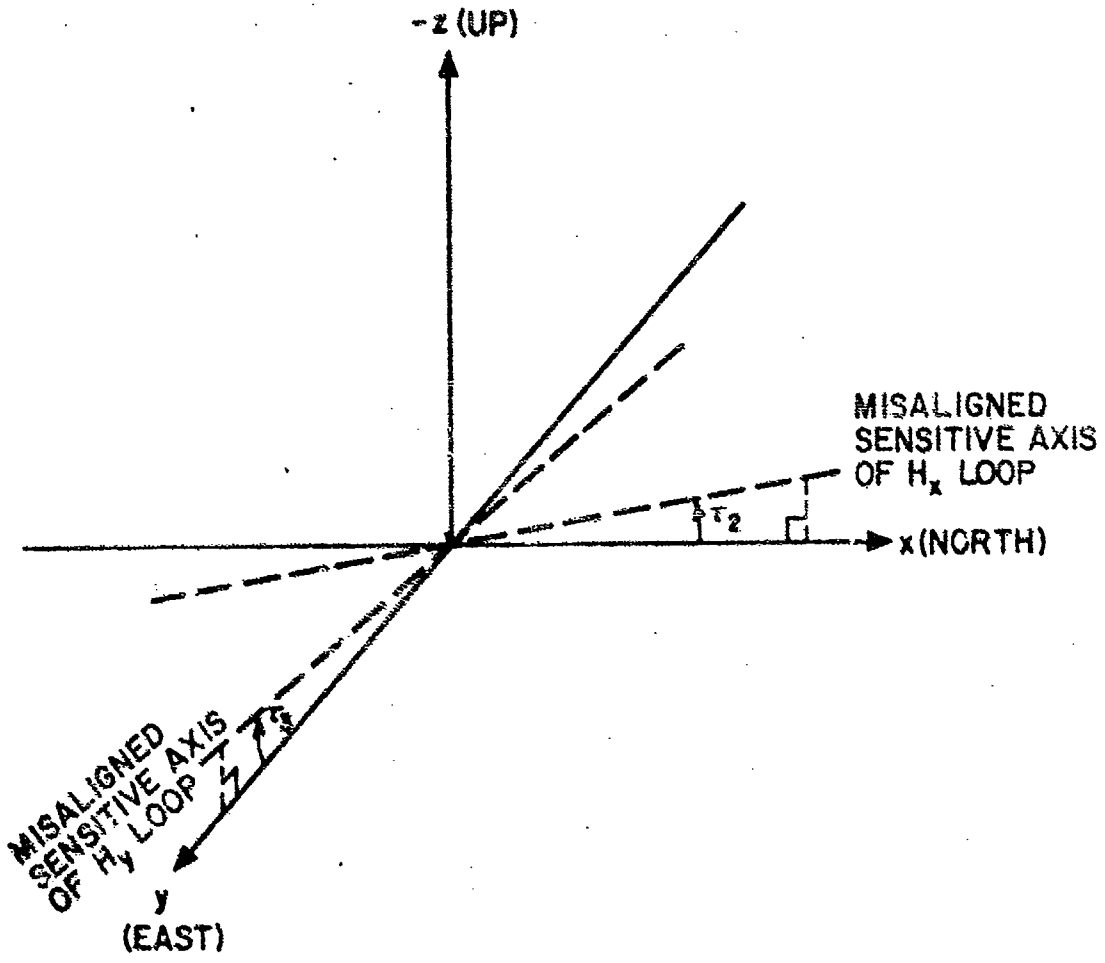


FIGURE 2.16. ISOMETRIC VIEW OF DIRECTION FINDER SITE SHOWING TILT IN SENSITIVE AXES OF LOOP ANTENNAS.

Let the tilt angles of the $H_x$ and $H_y$ loops be denoted by $\tau_2$ and $\tau_3$ (in radians). Then the Poynting vector estimates will again be in error, as

$$P_x = -E_z \left[ H_y \cos \tau_3 - H_z \sin \tau_3 \right]$$

$$P_y = E_z \left[ H_x \cos \tau_2 - H_z \sin \tau_2 \right]$$

Assuming the tilts are small, and using the field quantities from equation (2.29) for $\alpha = R = 0$, the resolved angle is given by

$$\hat{\theta} = \angle \overline{e^{j\theta} - \tau_3 + j\tau_2} \quad .$$

or, equivalently,

$$\Delta\theta \cong \tau_2 \cos\theta - \tau_3 \sin\theta \quad . \tag{2.69}$$

Finally, consider the alignment of the vertical antenna. In the new direction-finding signal processing technique presented herein, a small error in the measurement of $E_z$ does not produce any first-order effect on the direction-finding error, since the measurement discrepancy simply appears as a common factor in $\hat{P}_x$ and $\hat{P}_y$. The polarization error characteristics will be slightly modified but only in nature and not in overall magnitude. This is fortunate, as it was pointed out in Section II.B.3 that the vertical electric dipole is especially susceptible to axis perturbation. However, techniques have been proposed which depend critically on the vertical antenna performance, and this is the topic of the next section.

## 5. Errors in "Quadrature Direction-Finders" Due to Antenna Axis Perturbation

Cousins [1972] and Tsuruda and Hayashi [1974] among others, have proposed and/or implemented VLF direction-finder systems designed to have zero polarization error. They are based on utilization of the loop signal components which are in exact quadrature with the signal on the vertical antenna, as opposed to the present system which uses the in-phase component. Recalling the expressions for the IF voltages, they can be recast as

$$\begin{aligned} V_1 &= E_1 \left[ A \, (-\cos \beta) \right] \\ V_2 &= E_1 \left[ A \, (\sin \theta) + B \, (-\sin \beta \cos \theta) \right] \\ V_3 &= E_1 \left[ A \, (-\cos \theta) + B \, (-\sin \beta \sin \theta) \right] \end{aligned} \tag{2.70}$$

where:

$$\begin{aligned} A &= \cos \alpha - jR \sin \alpha \\ B &= \sin \alpha + jR \cos \alpha \end{aligned} \tag{2.71}$$

The B-components are not wanted in the in-phase technique. That portion of B which is in phase with A, that is, $A \cdot B$, causes polarization error. By contrast, in the quadrature technique, the A components are rejected by

shifting the $V_1$ signal phase by $90^\circ$ before the cross-multiplications. With only the B components left, the angle is resolved in a different way. Representing the operations mathematically,

$$\hat{\theta}' = \angle \frac{1}{4}\left[jV_1 V_2^* + (jV_1)^* V_2\right] + \frac{j}{4}\left[jV_1 V_3^* + (jV_1)^* V_3\right] \qquad (2.72)$$

or

$$\hat{\theta}' = \angle j\left[AB^* - A^* B\right] \frac{E_1^2}{4} \sin\beta \cos\beta \,(\cos\theta + j\sin\theta) \qquad (2.73)$$

yielding

$$\hat{\theta}' = \angle \frac{E_1^2}{2} R \cos\beta \sin\beta \, e^{j\theta}$$

so

$$\hat{\theta}' = \theta \,.$$

The quadrature direction finder displays no polarization error according to the formula shown. However, note that the quadrature direction finder does not produce a directional indication for linear polarization ($R = 0$), or if $\beta = 0^\circ$ or $90^\circ$; whereas the in-phase technique only fails if the polarization is pure linear horizontal ($R = 0$ and $\alpha = 90^\circ$ simultaneously), or if $\beta = 90^\circ$.

Now introduce a slight tilt in the sensitive axis of the vertical electric antenna, by an angle $\tau$ (in radians). The tilt will be assumed to be toward the x-axis, for simplicity, but the analysis is easily extended for general titls. The erroneous field measurement is

$$\hat{E}_z = E_z + \tau E_x \quad .$$

The measured voltage $V_1$ is now

$$V_1 = E_1 \left[ A(-\cos\beta) + \tau B(-\sin\theta) + \tau A(-\sin\beta\cos\theta) \right]$$

The resolved angle is now modified by the addition of the extraneous component, so that

$$\hat{\theta}' = \frac{\frac{E_1^2}{2}\left[ R\cos\beta\sin\beta\, e^{j\theta} + \tau R\sin^2\beta\cos\theta e^{j\theta} \right. \ldots}{\ldots \left. + \tau R(\cos^2\alpha - \sin^2\alpha)\sin\theta\, e^{j(\theta-\pi/2)} \right]} \quad . \tag{2.74}$$

The error under this condition, for $\tau$ small, is given by

$$\Delta\theta' = -\tau\left[\frac{2\cos(2\alpha)\sin\theta}{\sin 2\beta}\right] \quad . \tag{2.75}$$

The directional error is sinusoidal with azimuth, with the maximum error occurring at azimuths perpendicular to the direction toward which the antenna is tilted. The peak directional error in degrees per degree of axis tilt is given by the ratio $\Delta\theta'/\tau \sin\theta$, which is plotted in Fig. 2.17. The sensitivity of the system to vertical antenna orientation and perturbation is demonstrated by the high values of this ratio.

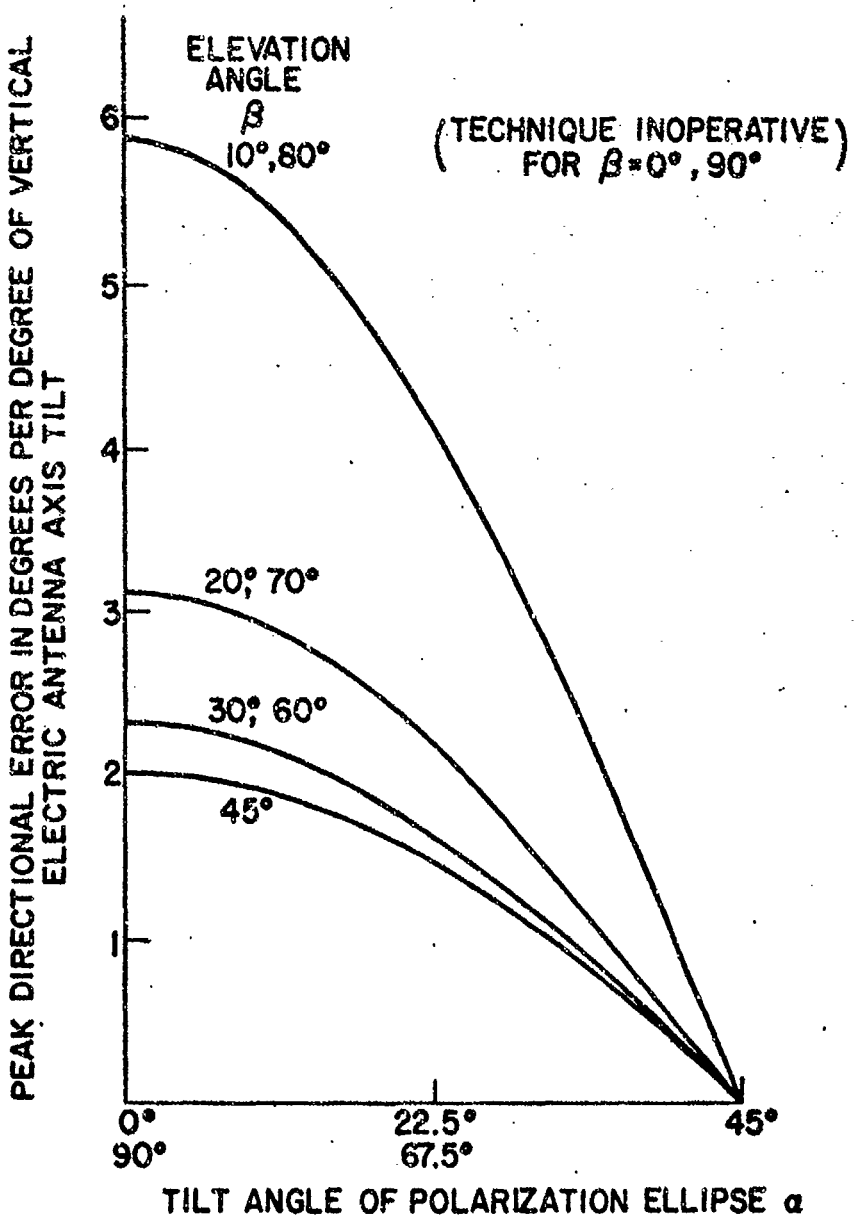


FIGURE 2.17. DIRECTION OF ARRIVAL ERROR IN THE QUADRATURE DIRECTION FINDER DUE TO A TILT IN THE EQUIVALENT AXIS OF THE VERTICAL ELECTRIC ANTENNA, FOR VARIOUS VALUES OF ELEVATION ANGLE AND POLARIZATION OF THE INCIDENT WAVE.

# III. DESCRIPTION OF THE APPARATUS

To demonstrate the feasibility of the new approach to VLF direction-finding and data gathering described in Fig. 1.3, a prototype instrument embodying the new principles and techniques presented was designed and constructed by the author at Stanford Electronics Laboratories. In this chapter, a description of the apparatus at the block diagram level, with some insight into the more novel circuits, will be provided. Detailed schematic diagrams are presented in Appendix B.

## A. SYSTEM DESIGN

A diagram of the instrument emphasizing the functional blocks is presented in Fig. 3.1.

The output voltages from the antenna block contain the desired signal in addition to the undesired energy in the remainder of the VLF spectrum. The translation and filtering block serves first to translate the input spectrum so that the desired signal lies at the intermediate frequency (IF); then by passing the translated spectrum through the IF bandpass filter, a filtered version of the desired signal ($V_1 e^{j\omega_{IF} t}$) is obtained. The filtered signals from the three antenna elements are applied to the direction-finding processor in which the estimated direction of arrival is resolved.

Turning to the lower part of the diagram, the parameter extraction block makes measurements of the frequency error ($\Delta f$), signal strength (SS), and signal-to-noise ratio (SNR) existing in the IF. Based on the latter two quantities, the signal detection block makes a decision as to whether a

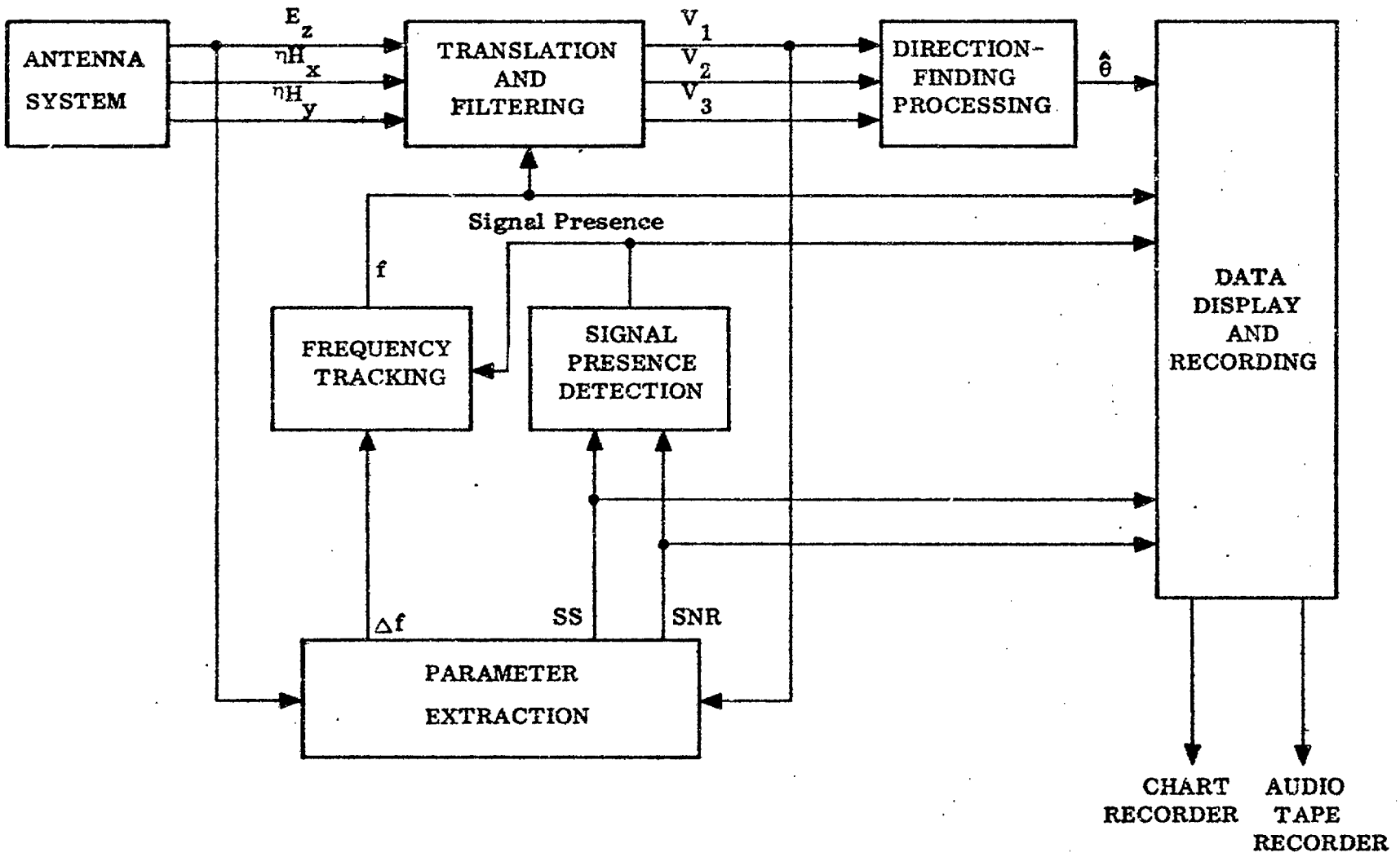


FIGURE 3.1. BLOCK DIAGRAM OF THE APPARATUS.

desired signal is present. If an affirmative decision is made, the frequency tracking block is enabled. Under this condition, the frequency error information from the parameter extraction block is permitted to control the tuning frequency of the receiver to accomplish frequency tracking of the signal.

In the data display and recording block, the directional data and additional parameters of interest are made available for display and chart recording. In addition, the analog voltages are converted into a frequency-modulation format and frequency-multiplexed into a single composite signal which can be recorded on an ordinary audio tape. This approach facilitates the storage and correlation of the data with the raw VLF spectrum from which it was extracted.

## B. ANTENNA SYSTEM

The instrument was designed to operate with the existing antenna and preamplifier systems at the Stanford, California, and Roberval, Quebec, observing sites. The physical design of the antenna system is shown in Fig. 3.2. The preamplifiers are designed so that the voltage outputs from the loops and vertical antennas are equal and in-phase for a given incident signal (allowing for the directional patterns of the elements). These outputs therefore correspond to $E_z$, $\eta H_x$, and $\eta H_y$.

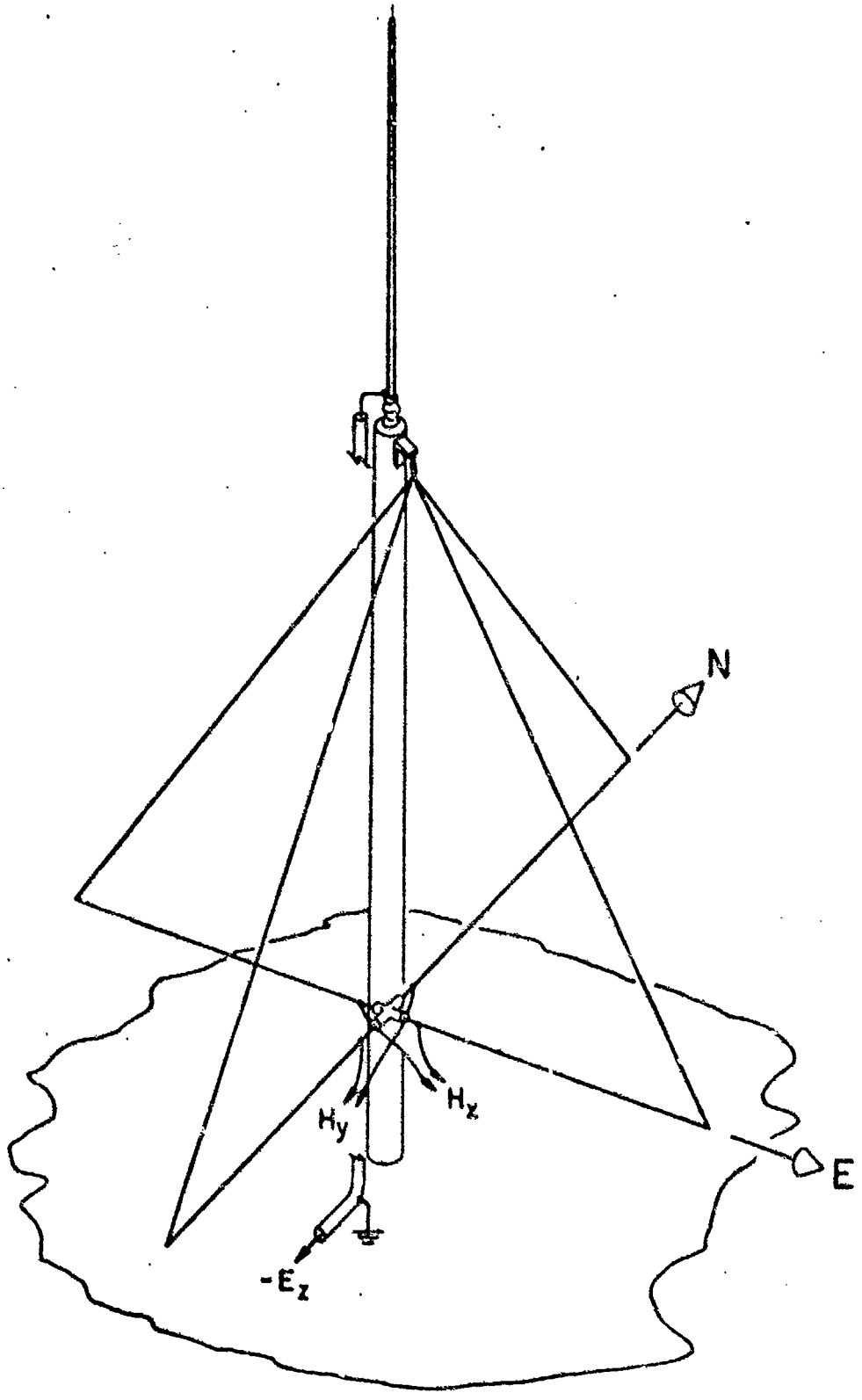


FIGURE 3.2 PHYSICAL DESIGN OF THE ANTENNA SYSTEM.

## C. TRANSLATION AND FILTERING

The operations accomplished within the translation and filtering block are illustrated in Fig. 3.3. The local oscillator signal is split and heterodyned against each of the preamplified antenna signals, generating sum and difference frequency components. When the local oscillator frequency is set higher than the signal frequency by an amount exactly equal to the intermediate frequency, the difference component falls in the passband of the IF filters and the signal is passed.

The bandpass filtering is accomplished by active filter circuits [Tow, 1969] constructed from operational amplifiers. To provide a response with a flat top and steep skirts, two resonators are stagger-tuned to frequencies just above the below the IF center frequency. The response characteristic obtained is shown in Fig. 3.4. The selection of the IF filter bandwidth was the result of a compromise between rejection of interference and tracking capability for signals which change frequency rapidly. According to the relationship derived in equation ( 2.7 ), the 340 Hz bandwidth selected permits tracking of frequency changes up to 57.8 kHz per second.

## D. DIRECTION-FINDING PROCESSING

The direction-finding technique has been analyzed in Section II.C.1. The illustration of Fig. 2.10 provides a model for the processing operation, but in practice the use of analog multipliers is avoided by applying the novel implementation shown in Fig. 3.5. The IF signal from the vertical antenna

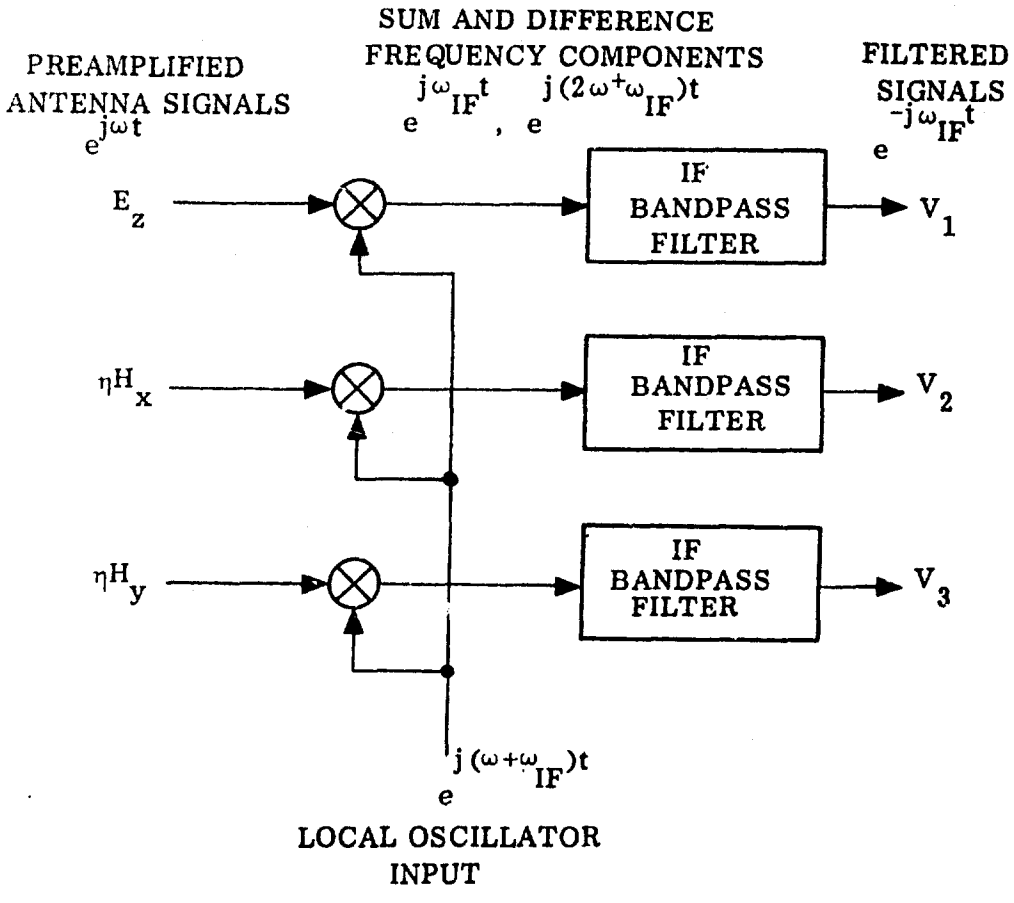


FIGURE 3.3 OPERATIONS WITHIN THE TRANSLATION AND FILTERING BLOCK.

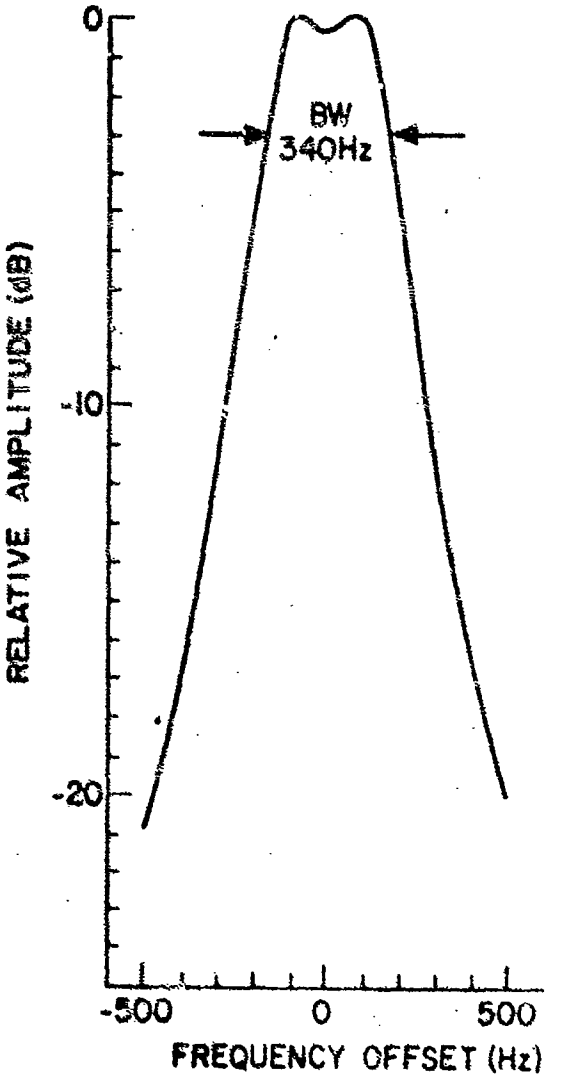


FIGURE 3.4 FREQUENCY RESPONSE CHARACTERISTIC OF IF BANDPASS FILTER.

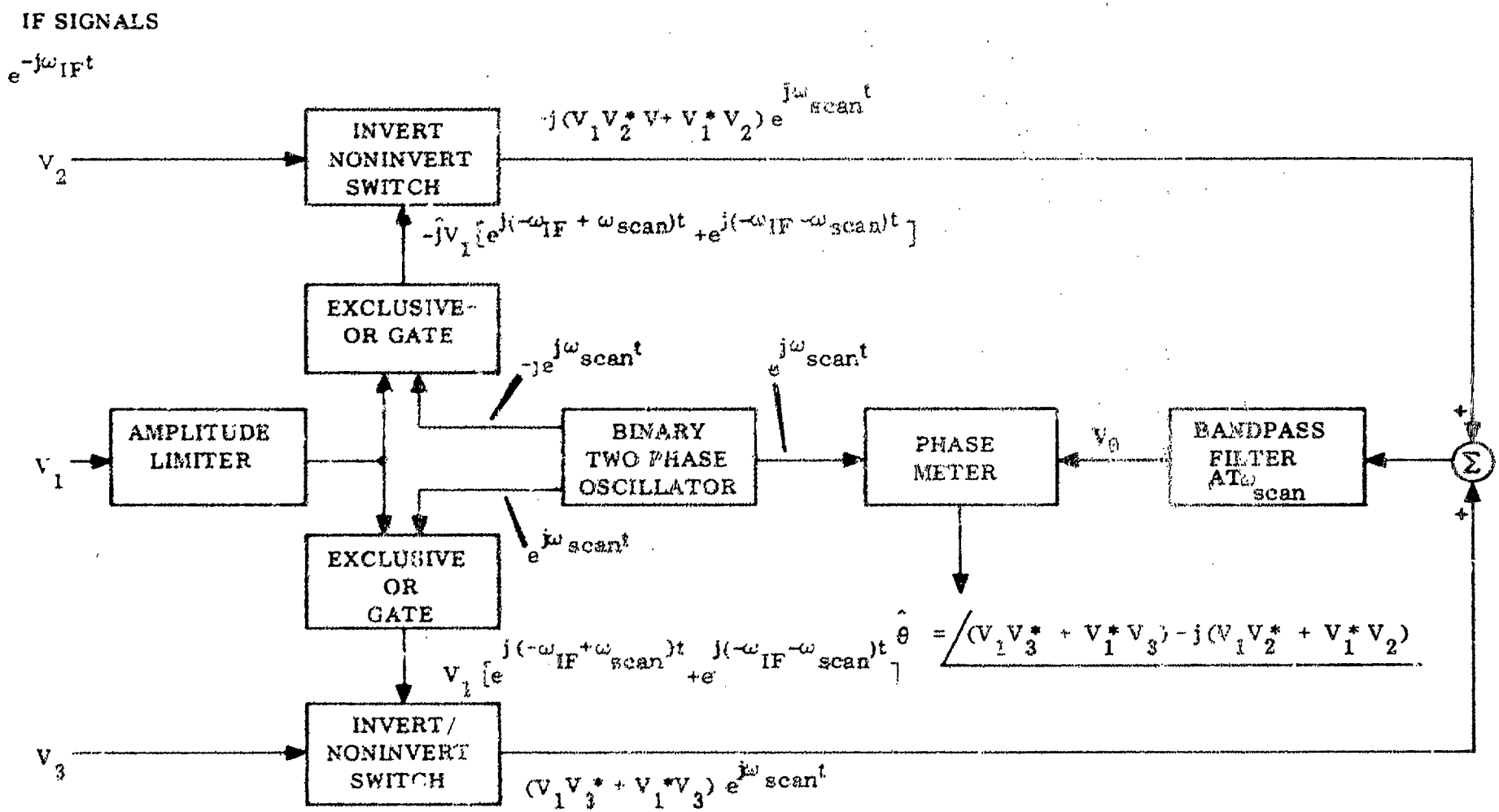


FIGURE 3.5 DIRECTION-FINDER PROCESSING BLOCK DIAGRAM

is applied to an amplitude limiter to convert it into a binary waveform retaining only the phase information from the signal. Similarly, the multiphase oscillator produces binary waveforms corresponding in phase to the sinusoids $e^{j\omega_{scan}t}$ and $-je^{j\omega_{scan}t}$. The multiplications can then be perform between the binary waveforms by using digital exclusive-or gates, and multiplication of the binary waveform with the analog signals $V_2$ and $V_3$ requires only an inverting/noninverting switch. Upon bandpass filtering of the combined output at the frequency $\omega_{scan}$, the higher harmonics generated by the use of binary waveforms are removed and the summed voltage corresponds to

$$V_\theta = \left[ (V_1 V_3^* + V_1^* V_3) - j (V_1 V_2^* + V_1^* V_2) \right] e^{j\omega_{scan}t},$$

When the phase of this voltage is measured relative to $e^{j\omega_{scan}t}$, the angle estimate is produced,

$$\hat{\theta} = \angle (V_1 V_3^* + V_1^* V_3) - j (V_1 V_2^* + V_1^* V_2)$$

## E. PARAMETER EXTRACTION

The operational functions of the parameter extraction block are shown in Fig. 3.6. The filtered IF signal from the vertical antenna channel is applied to a frequency discriminator to measure the frequency error $\Delta f$. The signal strength SS is determined by applying the same signal to a logarithmic

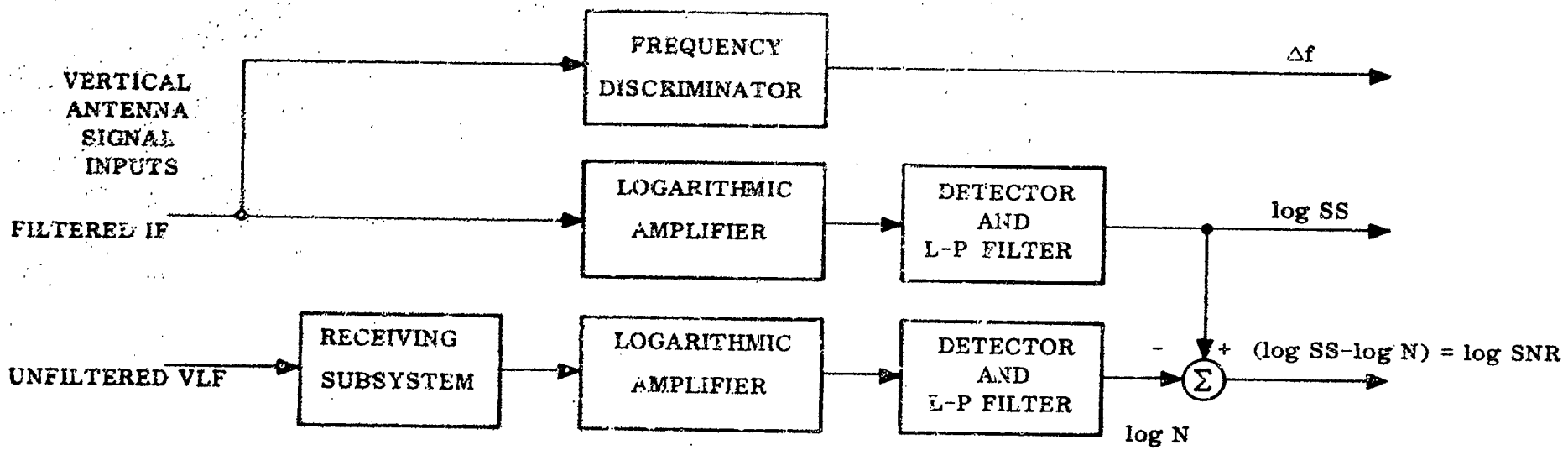


FIGURE 3.6 OPERATIONS WITHIN THE PARAMETER EXTRACTION BLOCK

amplifier, detector, and low-pass filter. The use of a logarithmic amplifier permits the detector to operate on signals over a 60 dB dynamic range.

The unfiltered VLF spectrum from the vertical antenna is applied to a receiving subsystem identical to the local oscillator, mixer, and IF filter used for the three primary channels. This receiving subsystem is independently tuned, manually, to a region of the VLF spectrum where the signals of interest are absent; broadband noise originating in spheric activity, however, is present in this region. Thus, when this independent channel is applied to a logarithmic amplifier, detector, and low-pass filter, a measure of the noise amplitude is obtained. By subtracting this logarithmic value from the logarithmic signal strength, the logarithmic signal-to-noise ratio is calculated.

F. SIGNAL PRESENCE DETECTION

The function of this block is to determine whether a signal of interest is present. Thresholds are set for signal strength SS and signal-to-noise ratio SNR which must be exceeded to cause the transition from a no-signal decision to a signal-present decision. The reverse process can be initiated by a loss of signal strength or signal-to-noise ratio, in addition to auxiliary checks on the signal frequency and the time duration of the signal.

G. FREQUENCY TRACKING

The frequency tracking block consists of an integrator with a presettable initial condition and with electronically switched integrate/hold modes.

The input to the integrator is the frequency error information from the parameter extraction block. The output is a voltage which controls the frequency of the receiver local oscillator.

In operation, the operator selects the initial condition as a frequency which the signal of interest is likely to pass through. When the signal first appears in the receiver passband and is detected by the signal presence detection block, the integrator is enabled. Thereafter, any offset between the signal frequency and the center frequency of the receiver passband is detected by the parameter extraction block and applied to the integrator to correct the tuning frequency of the receiver. When the signal has terminated, the integrator is reset to the initial condition frequency to await another signal.

## H. DATA DISPLAY AND RECORDING

The direction-of-arrival data and signal parameters of interest (frequency, signal strength, and signal-to-noise ratio) are made available for display on a panel meter, digital readout, or external analog chart recorder. In addition, the frequency, direction-of-arrival, and either signal strength or signal-to-noise ratio are converted to a frequency-modulation format and combined into a single audio channel suitable for recording on a track adjacent to the recording of the broadband VLF spectrum which produced the data.

The tape data interface is diagrammed in Fig. 3.7. The local oscillator is heterodyned against an oscillator operating at the IF frequency

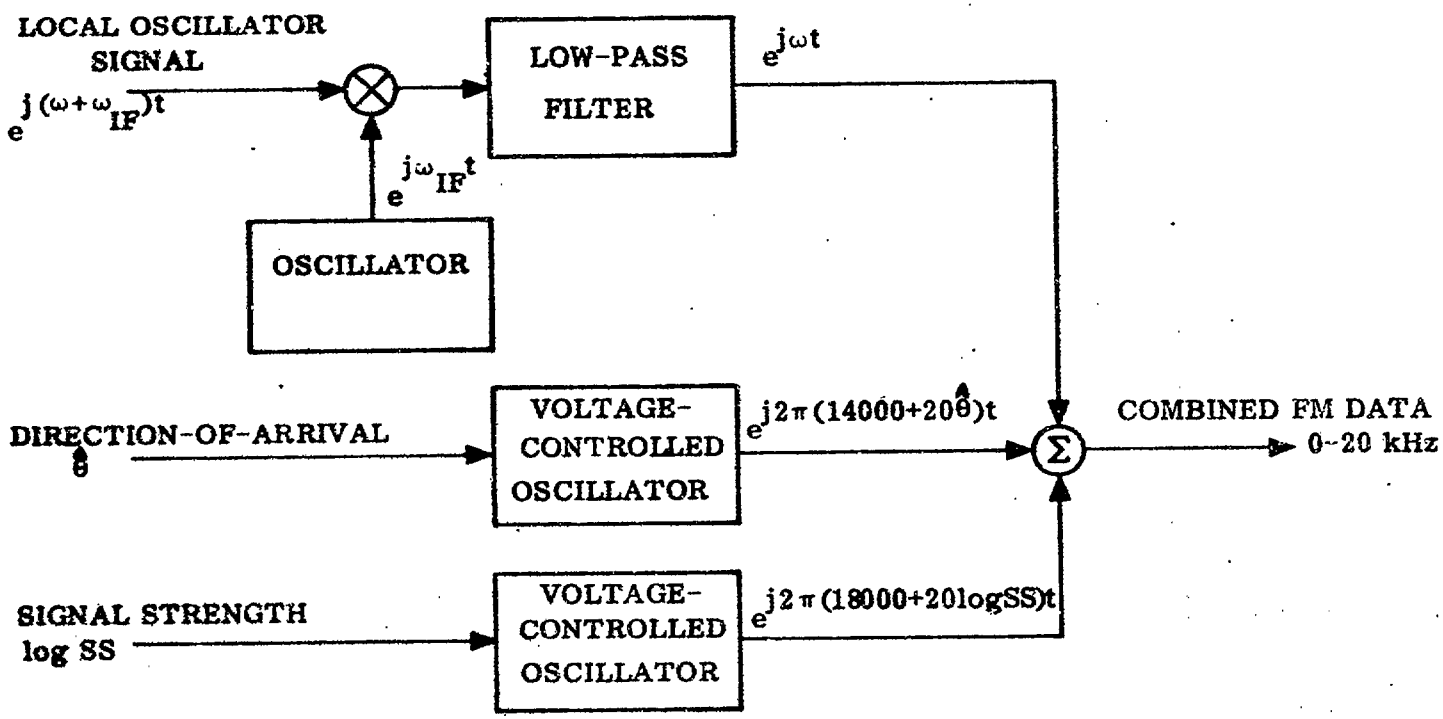


FIGURE 3.7 CONVERSION OF DATA TO A FREQUENCY-MODULATION FORMAT

to produce a difference frequency component at the signal frequency. The sum frequency component is removed by a low-pass filter. Thus, the tracking frequency of the receiver is represented by a sine-wave at the tracking frequency itself. The directional and signal strength data are applied to voltage-controlled oscillators to generate frequency modulated sine waves representing $\hat{\theta}$ and log SS. The directional data reside in the 10.4 to 17.6 kHz band and the signal strength data are in the 18.0 to 19.2 kHz region. Both of these signals can be combined with the frequency-indicating signal, which is confined to the 0 to 10 kHz band, by a simple addition. The resultant signal carries all the information in a 0 to 20 kHz bandwidth.

In Fig. 3.8, an example is presented showing a spectrum analysis of the data channel adjacent to a spectrum analysis of the raw VLF spectrum from which the data were extracted. A useful method for applying the data channel is also shown, in which the raw VLF spectrum is mixed with the data channel before spectrum analysis. The tracking of the whistler is evidenced by the superposition of the tracking frequency trace and the whistler trace. For detailed examination of the direction-finding and signal strength data, a separate expanded analysis of the 10 to 20 kHz region of the data track can be performed as will be demonstrated on the field data records in Section IV.

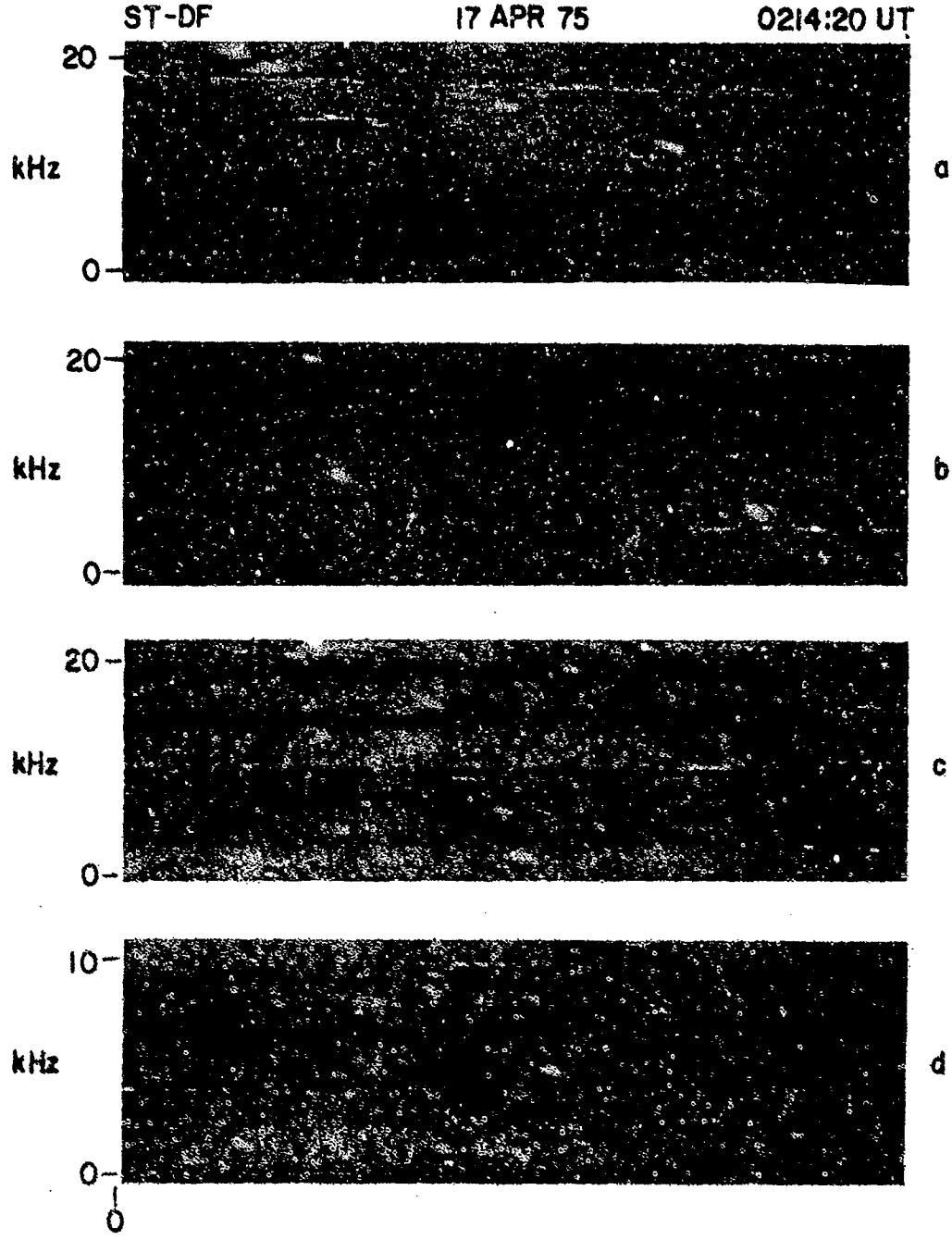


FIGURE 3.8 UTILIZATION OF FM DATA CHANNEL. (a) Conventional VLF spectrum analysis of a whistler received at Stanford. (b) Spectrum analysis of the FM data channel produced during reception of the whistler. Traces indicate, top to bottom, the relative signal strength, direction of arrival, and frequency of the signal. (c) Analysis of composite audio formed by mixing the raw VLF data with the FM data track. Tracking of the signal is evidenced by the superposition of the tracking frequency trace and the whistler trace. (d) Expanded version of (c). This record also shows the 100 Hz tone used to mark the event for rapid access at a later date.

## IV. EXPERIMENTAL OBSERVATIONS AND RESULTS

After initial testing of the prototype frequency-tracking direction-finder in the laboratory, the equipment was installed first at Stanford, California, and then at the Stanford-operated observing site at Roberval, Quebec, Canada. These testing programs are discussed herein according to chronological order. The quality and degree of interest in the results actually follows the reverse order; partly because the development of the equipment was still in progress during the Stanford program, and partly because of the greater abundance of VLF signals of interest at Roberval.

### A. LABORATORY TESTING

#### 1. Frequency Tracking

After testing of the individual circuits and functional subsystems of the instrument, a test was conceived to demonstrate the overall capabilities of the frequency tracking function. An artificial whistler generator was constructed by connecting a discharging R-C circuit to a voltage-controlled oscillator to produce a sine-wave sweeping from 10 kHz down to zero frequency with an exponential profile resembling a whistler. The output of this oscillator was mixed with a white-noise generator to simulate VLF background noise. By restricting the noise bandwidth to 10 kHz with a low-pass filter, a quantitative measure of the noise power spectral density could be made.

With the whistler-and-noise simulator connected to the instrument and the controls adjusted so that the receiver would intercept the whistler at 9.2 kHz and track it down to 500 Hz, the speed of the whistler and the level of the noise were increased until the limits of the tracking capability were reached. The initial frequency excursion rate of the whistler was 32 kHz per second and the noise power spectral density was -32 dBm/Hz for this condition. (The signal level was 0 dBm.) This corresponds to a signal-to-noise ratio of -8 dB in the full 10 kHz VLF bandwidth, or +6.7 dB in the 340 Hz IF bandwidth. Fig. 4.1 shows analog chart records produced during this experiment demonstrating the tracking action and the correct measurement of the signal-to-noise ratio by the parameter extraction circuitry.

Further experimentation revealed that higher tracking rates and lower signal-to-noise ratios could be tolerated once the instrument was locked onto a signal, approaching the theoretical limits derived in Section II. For practical purposes, however, when an unknown signal must be acquired by the instrument, the limits determined by the test are more realistic.

To test the ability of the instrument to track whistlers and other VLF emissions in an actual spectral environment, tape recordings from Vandenberg, California; Eights Station, Antarctica; and Roberval, Quebec were played as input to the equipment. Successful tracking was achieved on strong whistlers, weak whistlers, nose whistlers, and magnetospherically propagated signals from the transmitter at Siple Station, Antarctica received at Roberval. Since a demonstration of the frequency-tracking capability is even more

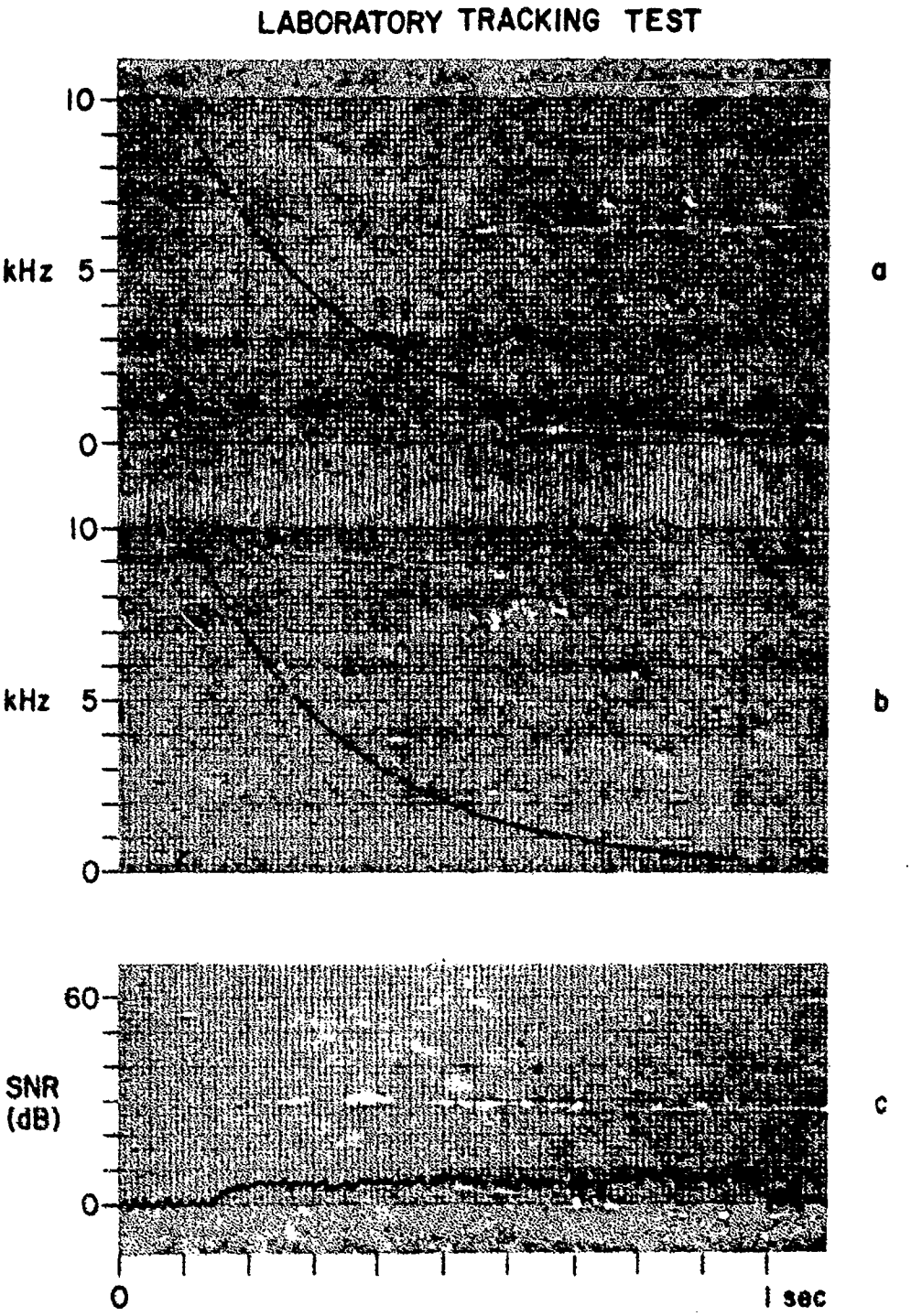


FIGURE 4.1 LABORATORY TRACKING TEST. (a) Frequency of electronically simulated whistler. Initial slope is -32 kHz per second. (b) Frequency of tracking receiver, showing capture of the "whistler" at 9.2 kHz and successful tracking down to lower operating frequency limit. (c) Signal to noise ratio indicated by parameter extraction circuitry. The indication agrees well with the measured signal to noise ratio of 6.7 dB.

convincingly presented from actual real time field operations, which are discussed in the following sections, the data records from these laboratory experiments will not be reproduced here.

2. Direction-Finding.

The instrumental accuracy of the direction-finder was measured using simulated directional signal inputs. Inverted and noninverted versions of a sine-wave signal were generated by operational amplifiers. The vertical antenna (channel 1) input was connected to the noninverted signal. By connecting the two loop inputs (channels 2 and 3) either to the noninverted signal, the inverted signal, or ground, signal directions of arrival of 0, $\pm 45^{\circ}$, $\pm 90^{\circ}$, $\pm 135^{\circ}$ and $180^{\circ}$ could be simulated. The instrumental errors for these angles, measured over a 40 dB range of signal levels, are shown in Table 4.1. Overall the RMS error for all the measurements was $1.25^{\circ}$.

TABLE 4.1 INSTRUMENTAL ERRORS OF DIRECTION-FINDER.

| Simulated Angle | $-135^{\circ}$ | $-90^{\circ}$ | $-45^{\circ}$ | $0^{\circ}$ | $+45^{\circ}$ | $+90^{\circ}$ | $+135^{\circ}$ | $180^{\circ}$ |
|---|---|---|---|---|---|---|---|---|
| Relative Signal Level (dB) | Instrumental Error (Degrees) | | | | | | | |
| 0 | 0.0 | +0.5 | +0.5 | -0.5 | +1.0 | 0.0 | 0.0 | +1.0 |
| -10 | +0.5 | -0.5 | -1.5 | -0.5 | +2.0 | -0.5 | -1.5 | 0.0 |
| -20 | -0.5 | -1.0 | -0.5 | -1.0 | +1.0 | -1.0 | -0.5 | -0.5 |
| -30 | -2.5 | -1.5 | 0.0 | -1.0 | -1.5 | -1.0 | +0.5 | +1.0 |
| -40 | +0.5 | +4.0 | +0.5 | -1.5 | +1.0 | -2.0 | -2.0 | -2.0 |

Again, as in the case of the frequency-tracking capability, the most convincing demonstration of the direction-finding operation of the instrument is provided by the actual real-time records presented in the sections which follow.

## B. FIELD OBSERVATIONS AT STANFORD, CALIFORNIA

The prototype frequency-tracking direction-finder was installed at the Stanford VLF observing site and operated during the period from 28 March to 9 June 1975. Observations were made on subionospherically propagated VLF transmitter signals and on whistlers.

### 1. Site Corrections

As no survey data were available for the antenna system at Stanford, no corrections could be applied for antenna misalignment. Earlier work at this site by Cousins [1972] indicated site errors up to $5^{\circ}$ according to bearings taken on VLF stations. The position of the feedlines running from the antennas to the equipment building had since been modified, however, so no attempt was made to apply his data as a correction factor.

### 2. VLF Transmitters

On 19 March 1975, bearings were taken on four VLF transmitters. Portions of the chart record showing the bearing indications for the stations Omega/Hawaii, Omega/North Dakota, NPG, and NAA are presented in Fig. 4.2. The bearing angles extracted from the chart are compared with the calculated great circle bearings of these stations in Table 4.2. The errors may be attributed mainly to site errors and antenna misalignment, and their magnitudes

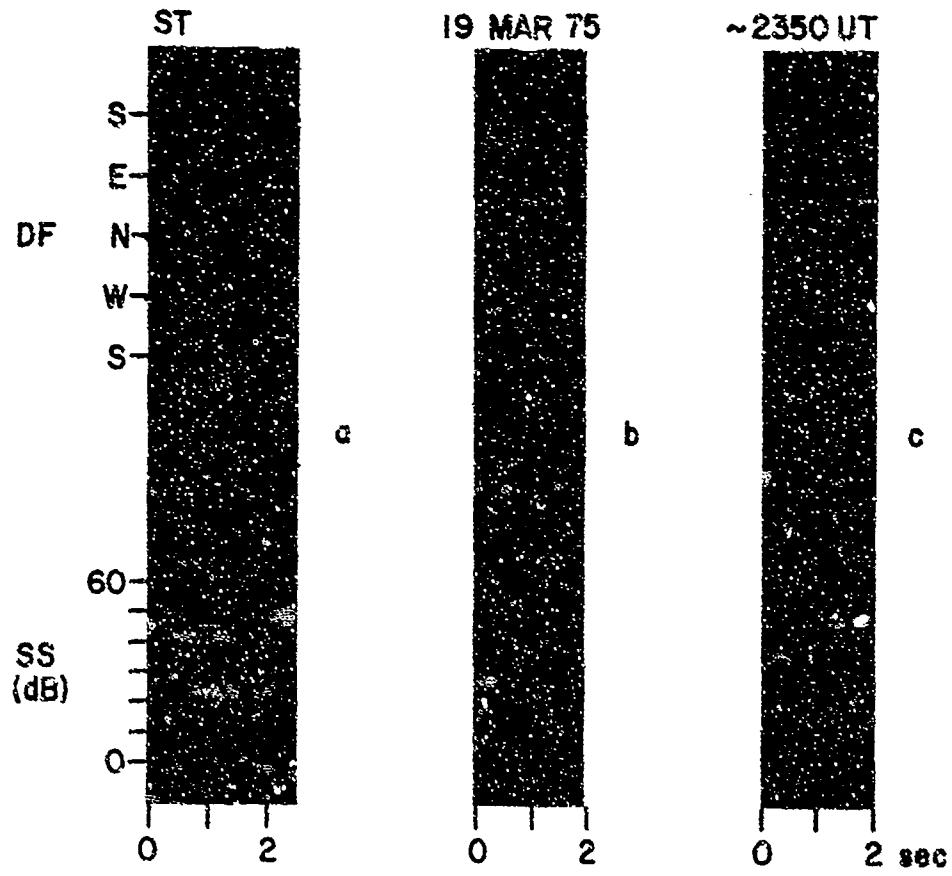


FIGURE 4.2 DIRECTION-FINDING ON VLF STATIONS RECEIVED AT STANFORD. Chart data show direction of arrival and relative signal strength. (a) OMEGA stations in Hawaii and North Dakota transmitting in sequence on 11.33 kHz. (b) NPG, 18.6 kHz. (c) NAA, 17.8 kHz. Results are given in Table 4.2.

TABLE 4.2 DIRECTION-FINDING RESULTS ON VLF STATIONS RECEIVED AT STANFORD.

| Station | Frequency | Location | Indicated Bearing | True Bearing | Error |
|---|---|---|---|---|---|
| OMEGA/H. | 11.33 | Hawaii | $257.0^{\circ}$ | $252.6^{\circ}$ | $+4.4^{\circ}$ |
| OMEGA/N.D. | 11.33 | N. Dakota | $59.4^{\circ}$ | $55.6^{\circ}$ | $+3.8^{\circ}$ |
| NPG | 18.60 | Washington | $1.7^{\circ}$ | $1.0^{\circ}$ | $+0.7^{\circ}$ |
| NAA | 17.80 | Maine | $68.4^{\circ}$ | $62.0^{\circ}$ | $+6.4^{\circ}$ |

are close to those of Cousins' results. For the signals from NAA and Omega/North Dakota, polarization error may also have been a factor, as sunset was occurring along the path and this condition was shown by Horner [1957] to be conducive to such errors.

To further demonstrate the usefulness of the instrument in direction-finding studies of polarization error on the signals from VLF transmitters continuous records of the bearings for several stations were made over 24-hour periods. In agreement with Horner's results, the daytime errors were low, rising at sunset and varying cyclically through the night, and falling off at sunrise. A particularly interesting example for station NPG showing a dramatic change in the behavior of the polarization error just before sunrise is presented in Fig. 4.3.

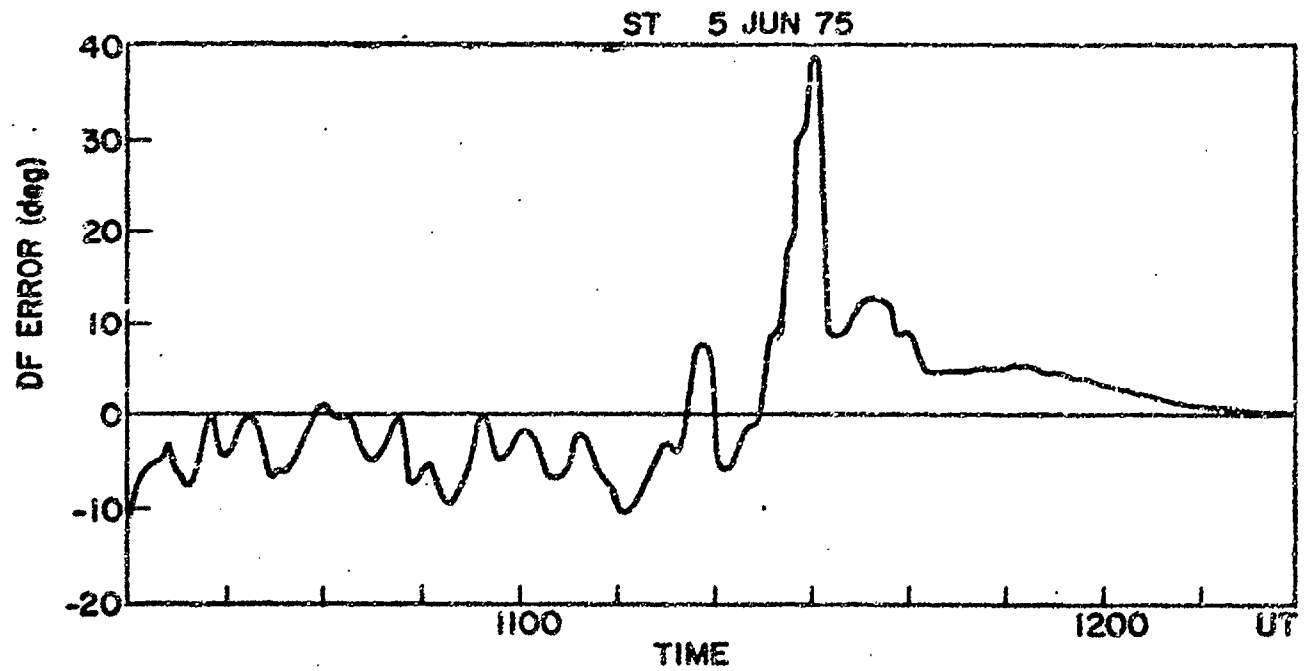


FIGURE 4.3 POLARIZATION ERROR BEHAVIOR IN THE HOURS BEFORE LOCAL SUNRISE (1246 UT) FOR STATION NPG RECEIVED AT STANFORD.

### 3. Whistlers

The VLF observing site at Stanford was unattended during the whistler monitoring program. Human attention was limited to one brief visit every two days, at which time the operator could mount one new reel of tape (holding 1½ hours of data) and change the equipment adjustments or select a different time period for the next monitoring run. The actual recording was triggered automatically by a clock to occur during an early morning hour, since that period was known to be favorable for whistler reception. These conditions made it imperative that the operator have immediate data on the results of the previous run so that he could intelligently modify the equipment adjustments or the recording time period for the next run.

To fulfill this requirement, the signal presence detection capability of the instrument was applied to cause a pen deflection on a chart recorder running at a very slow speed. With this arrangement, the operator could scan an entire two-day period quickly to determine if signals were being tracked. If any occurred during the 1½ hour tape recording period, they could be located immediately and aurally reviewed without listening to or spectrum analyzing the entire tape.

A total of 18 recordings were made, containing 27 hours of VLF data. Eleven whistlers were found which were tracked by the equipment, most of them in the latter part of the program when the equipment settings had been optimized. Two examples are shown in Fig. 4.4. While both bearing indications show considerable variability, the example of 9 May shows a

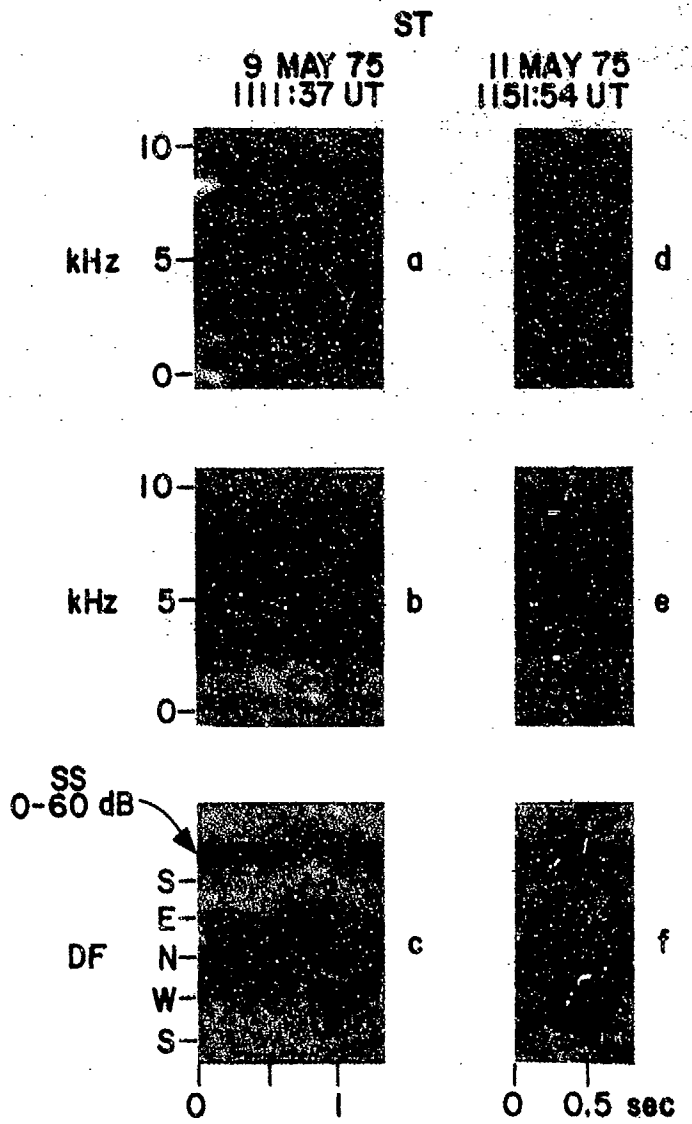


FIGURE 4.4 WHISTLERS RECEIVED AT STANFORD. (a) VLF spectrum showing whistler on 9 May 1975. (b) Spectrum analysis of VLF mixed with FM data channel showing tracking of whistler frequency. (c) Signal strength and direction of arrival data for the whistler. Bearing data show considerable variability but a predominance toward northeast to east. (d), (e), and (f) Similar records for a whistler on 11 May 75, showing predominantly western bearing. Both examples show evidence of multiple components which may be responsible for variability of bearing indication. (Blanking of DF trace in the absence of a signal was not included at this time.)

general easterly direction, while the whistler of 11 May displays generally west to southwest bearings. The variability within each example is attributable to multiple whistler components, which are clearly demonstrated by the rather diffuse spectral trace of the whistlers. The performance of the direction-finder in the presence of multiple signals was discussed in Section II.C.2, where it was shown that the average bearing would tend to be that of the strongest signal component, with periodic variations about the average having a magnitude dependent on the relative amplitude and bearing angles of the interfering components, and with a periodic rate corresponding to the difference frequency between the primary component and the interference While specific components cannot be identified in the examples, the bearing displays are consistent with such an explanation.

## C. FIELD OBSERVATIONS AT ROBERVAL, QUEBEC

The prototype frequency-tracking direction-finder was installed at Roberval, Quebec and operated during the period from 26 June until the end of August 1975. Observations were made on VLF transmitters, natural VLF activity including whistlers, emissions, and chorus, and on artificially stimulated emissions produced by the signals from the Stanford-operated transmitter at Siple Station, Antarctica.

1. Site Corrections

A survey of the mounting points for the loop antennas revealed their orientation to be toward magnetic north rather than true north. Accordingly, the analysis of misalignment effects presented in Section II.C.4 was applied based on the survey data. The quantities $\delta = -19.92^{\circ}$ and $\epsilon = -17.56^{\circ}$ were obtained from the survey. From equation (2.68), the measured direction-of-arrival $\hat{\theta}$, contains an error,

$$\Delta\theta = 18.74^{\circ} + 1.18^{\circ} \cos 2\theta.$$

Solving for $\theta$ in terms of $\hat{\theta}$,

$$\theta = \hat{\theta} - 18.74^{\circ} - 1.18^{\circ} \cos 2 (\hat{\theta} - 18.74^{\circ}).$$

The raw data records presented herein show the indicated bearing $\hat{\theta}$; in all tabulated data and discussions of results, however, the corrected bearings are used.

2. VLF Transmitters

Bearing data were taken on stations NPG, GBR, and four Omega stations which could be received at Roberval. The chart records produced

during these observations are shown in Fig. 4.5, with the corrected bearings and a comparison to the calculated great circle bearings given in Table 4.3. Bearings on the VLF stations were found to be quite accurate and highly repeatable from day to day.

TABLE 4.3 DIRECTION-FINDING RESULTS ON VLF STATIONS RECEIVED AT ROBERVAL, QUEBEC.

| Station | Frequency | Location | Indicated Bearing | Corrected Bearing | True Bearing | Error |
|---|---|---|---|---|---|---|
| GBR | 16.0 | England | $74.3^{\circ}$ | $56.0^{\circ}$ | $56.8^{\circ}$ | $-0.8^{\circ}$ |
| NPG | 18.6 | Washington | $307.5^{\circ}$ | $289.7^{\circ}$ | $238.7^{\circ}$ | $+1.0^{\circ}$ |
| OMEGA/NOR | 10.2 | Norway | $53.4^{\circ}$ | $34.3^{\circ}$ | $34.3^{\circ}$ | $0.0^{\circ}$ |
| OMEGA/TRI | 10.2 | Trinidad | $189.7^{\circ}$ | $169.0^{\circ}$ | $163.0^{\circ}$ | $+6.8^{\circ}$ |
| OMEGA/H. | 10.2 | Hawaii | $297.9^{\circ}$ | $280.3^{\circ}$ | $281.1^{\circ}$ | $-0.8^{\circ}$ |
| OMEGA/N.D. | 10.2 | N. Dakota | $286.2^{\circ}$ | $268.6^{\circ}$ | $273.1^{\circ}$ | $-4.5^{\circ}$ |

### 3. Whistlers and Other Natural Activity

Conditions for observations at Roberval were considerably more favorable than at Stanford. A greater abundance of VLF activity was available, and the site was constantly manned during regular daily operating periods, permitting the instrument to be adjusted to meet the changing signal environment. In addition, a general confirmation of direction-finding results

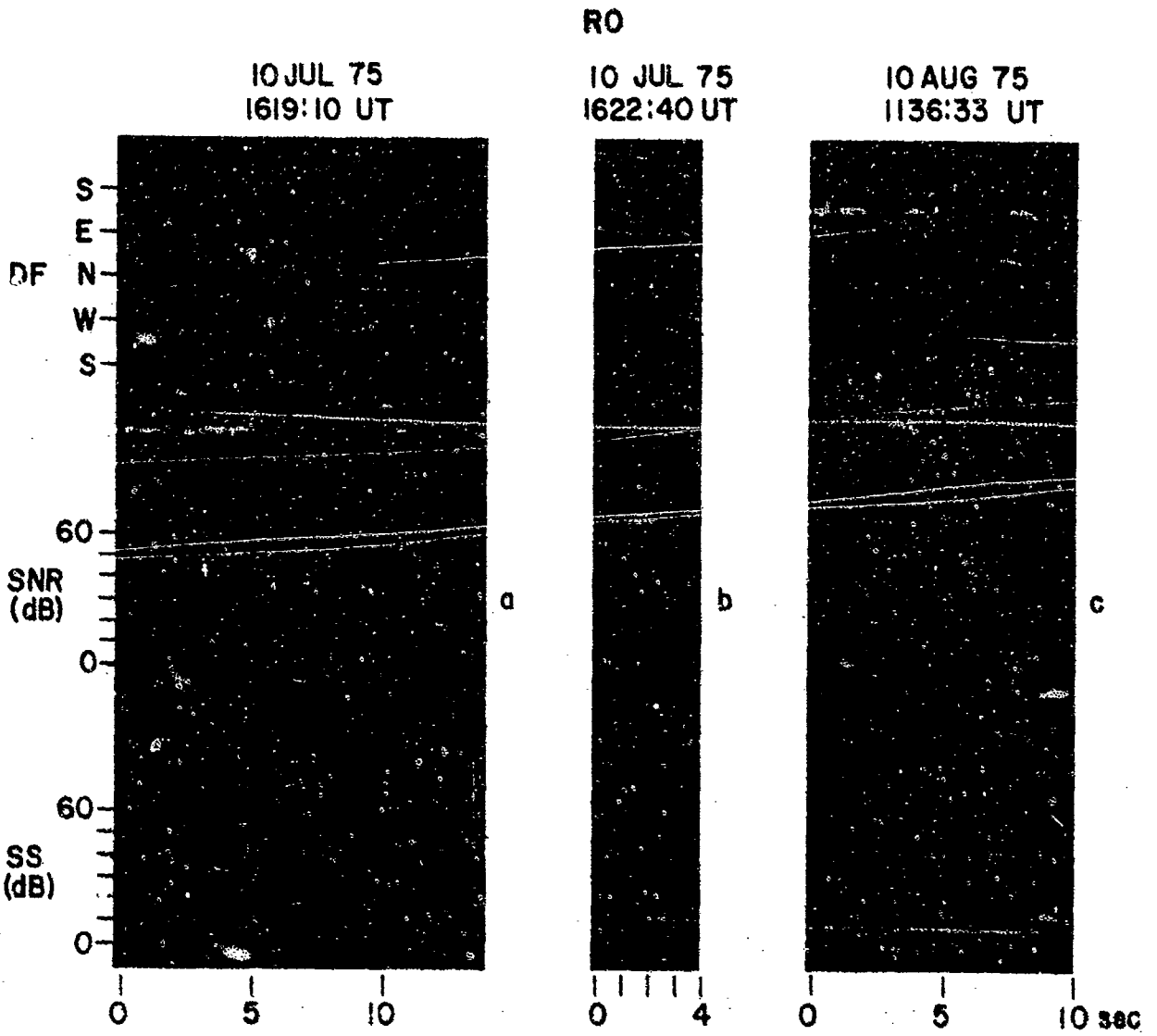


FIGURE 4.5 DIRECTION-FINDING ON VLF STATIONS RECEIVED AT ROBERVAL. Chart data show direction of arrival, measured signal-to-noise ratio, and relative signal strength. (a) Station GBR on 16.0 kHz. (b) NPG, 18.6 kHz. (c) OMEGA stations in Norway, Trinidad, Hawaii, and North Dakota transmitting in sequence on 10.2 kHz. Results are given in Table 4.3.

was made possible by comparing the bearings with the indicated magnetic latitude of the signal paths based on whistler nose frequency analysis. For the purposes of this comparison, a propagation model set up by Seely [1975] predicting nose frequencies of 3.5 to 3.6 kHz at the Roberval latitude was employed. Whistlers with higher nose frequencies would be expected to show southerly bearings, while those with lower nose frequencies should be found to the north. Signals with comparable nose frequencies might display any bearing, although if the bearing were near north or south the signal would have to be nearly overhead; in this case other signs might be present, such as high polarization error, indicating a high elevation angle of arrival. For non-whistler signals believed to propagate in the same ducts as whistlers, such as triggered emissions, the nose frequencies can be taken from whistlers occurring in the same time period for the purposes of this comparison.

An example of nose whistlers and associated emissions is given in Fig. 4.6. In many cases, the instrument was surprisingly successful in tracking the frequency of weak whistler components and emissions; this is demonstrated by the mixed record (b) in which components which were faint in the VLF spectrum are made clearly visible by the superposition of the tracker frequency trace. Within this record one can see cases of highly variable bearings (1.0 second) and relatively consistent bearings (5.5 seconds). These differences are attributable to multiple- versus single-component reception. Later examples will illuminate this more clearly.

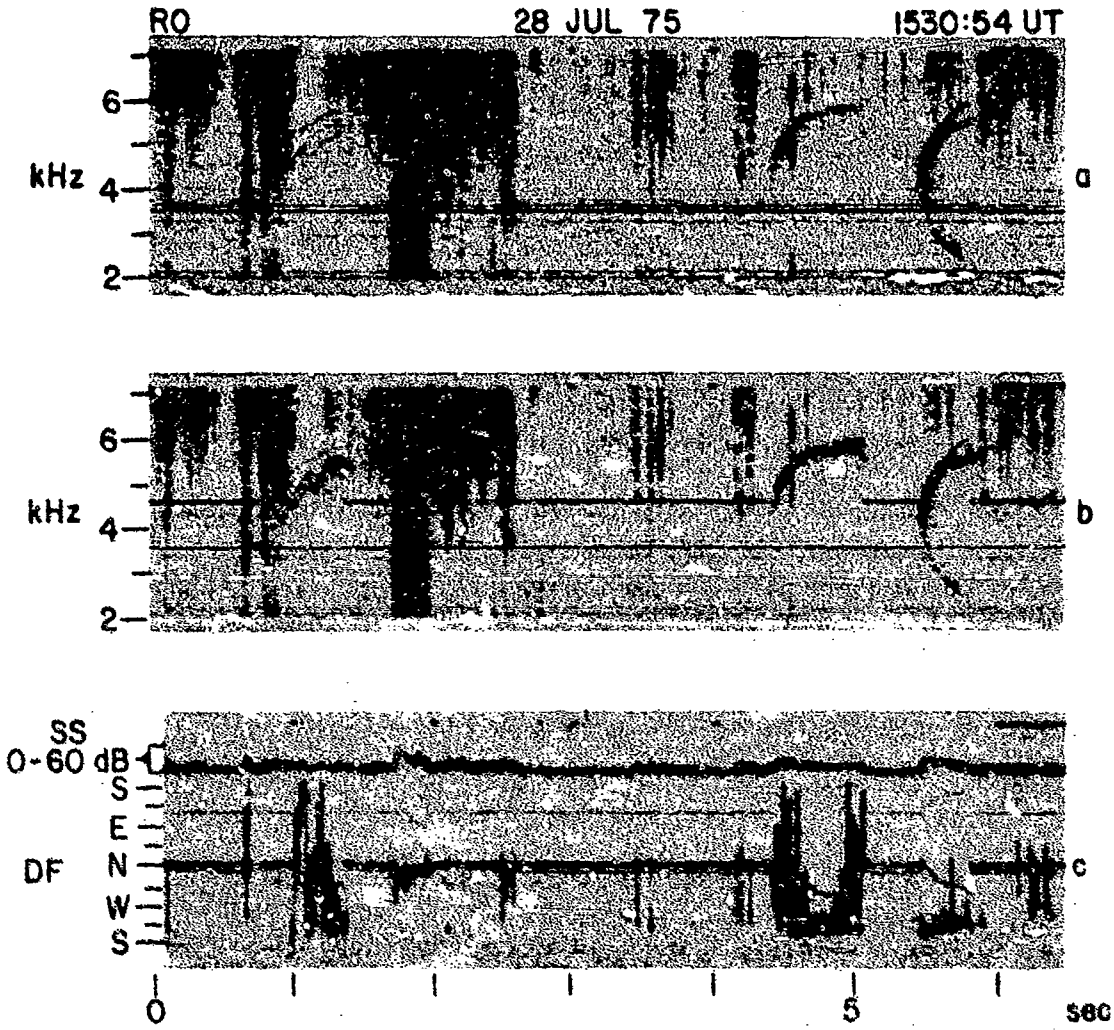


FIGURE 4.6 NOSE WHISTLERS AND ASSOCIATED EMISSIONS. (a) VLF spectrum analysis showing whistlers and associated emissions. (b) Spectrum analysis of VLF mixed with tracking frequency trace demonstrating tracking of signals. (c) Signal strength and direction-of-arrival data. The signals display a predominantly south-southwest bearing, in agreement with the indication by the whistler nose frequencies (~4.3 kHz) that the paths are southward of Roberval

The consistent bearings indicate a south-southwest (corrected) direction, in agreement with the nose frequencies at 4.3 kHz which indicate an exit point south of Reberval.

In the next example, Fig. 4.7, taken one minute later on the same day, a different perspective is provided. A 30-second time period is displayed to demonstrate the consistent south-southwest (corrected) bearings indicated for repeated excitations of the same whistler ducts. Also visible on this record are some strong spheric pairs (at 7 seconds and 13 seconds) which caused the two-hop whistler pairs at 11 seconds and 17 seconds. Bearings are indicated for these spherics also: south and then northwest for the first pair; south and then northeast for the second pair. The very strong whistler-associated emission at 27 seconds is the subject of the next example.

The VLF spectrum in Fig. 4.8(a) shows some weak whistler components and an intense emission triggered by one of these. The intensity of the emission is also evident from the signal strength trace in (c). In accordance with the high signal-to-noise ratio which exists for such a strong signal, the bearing indication is extremely steady. The direction is identical to the whistlers of Fig. 4.7, evidence that the emission has propagated through the same duct as the whistlers.

Several cases were observed in which the omissions associated with whistlers displayed better coherency than the whistlers themselves. An illustration of this observation is presented in Fig. 4.9. The spectrum

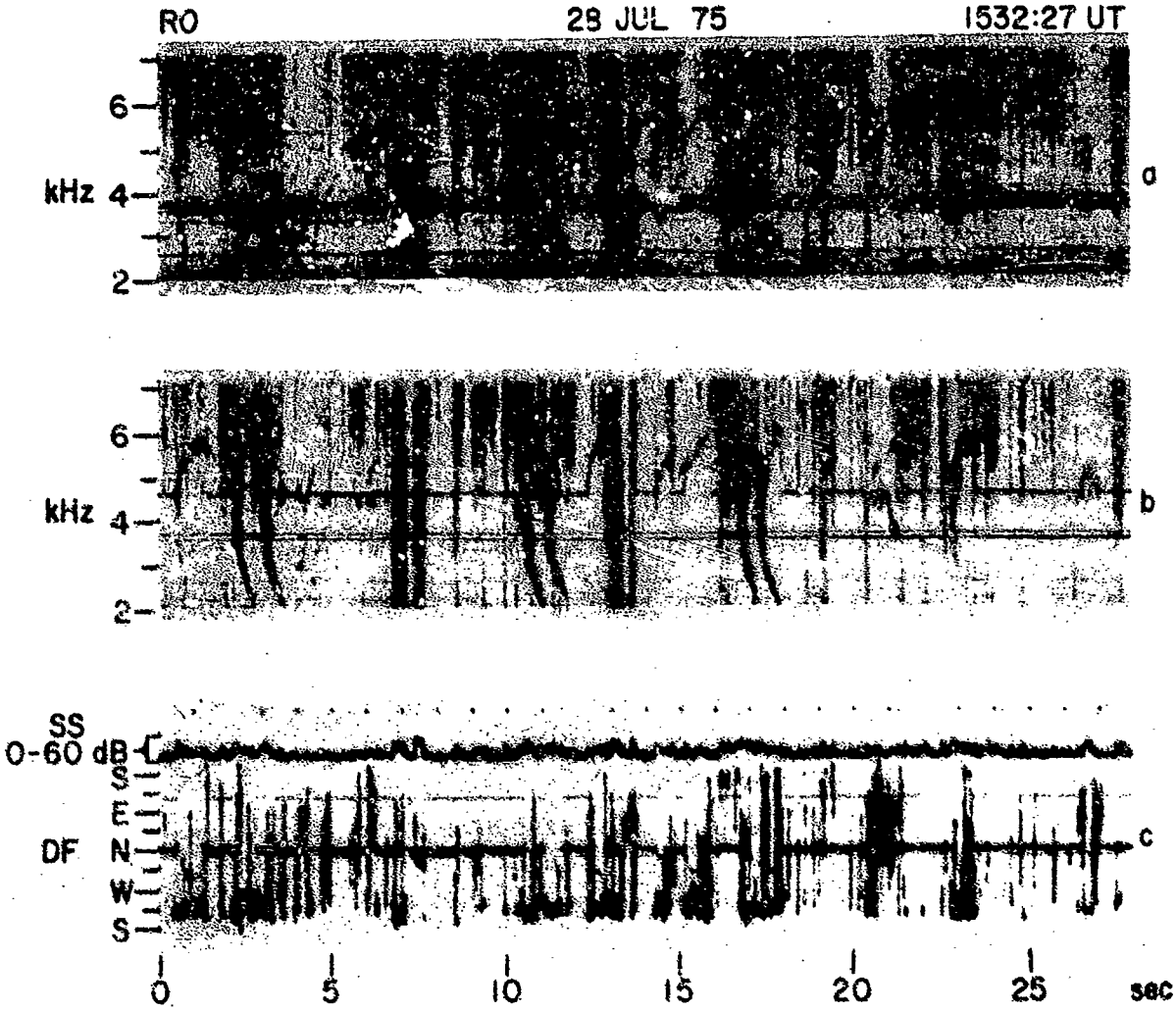


FIGURE 4.7 MULTIPLE WHISTLERS AND ASSOCIATED EMISSIONS. (a) VLF spectrum analysis showing repeated whistlers. The causative spherics are also visible. (b) Mixed VLF and frequency tracker showing tracking of whistlers. (c) Signal strength and direction-of-arrival data. Bearings are consistent between the repeated whistler excitations. The bearings of the causative spherics are also displayed.

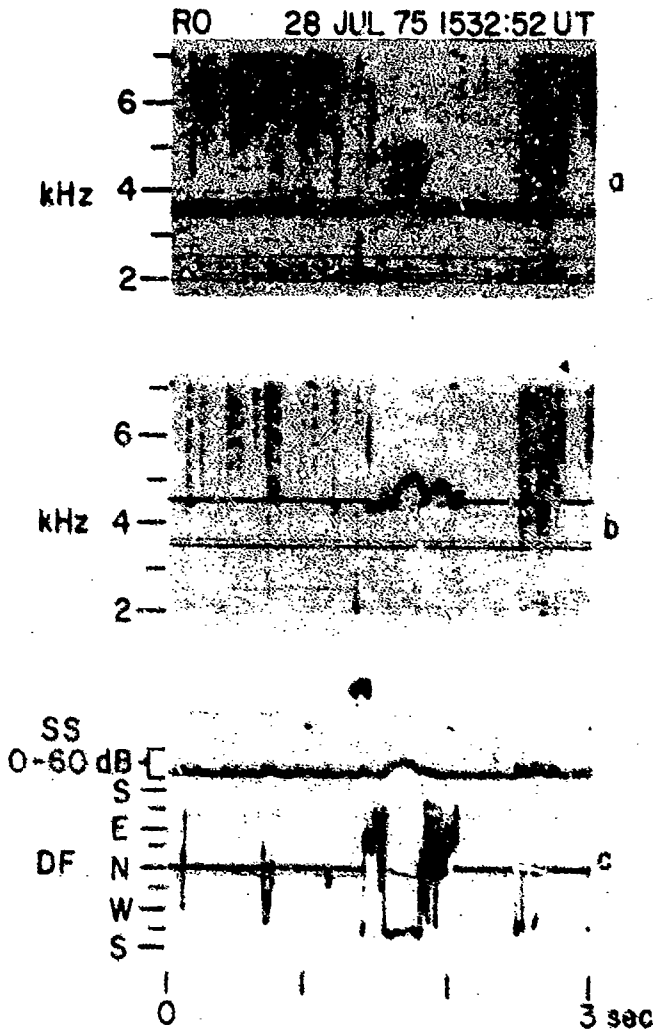


FIGURE 4.8 WHISTLERS AND ASSOCIATED EMISSION. (a) VLF spectrum analysis. (b) Mixed VLF spectrum and frequency tracking trace showing instrument tracking emission and weaker whistler components. (c) Signal strength trace demonstrates high intensity. Bearing indication is extremely steady in accord with high signal-to-noise ratio existing.

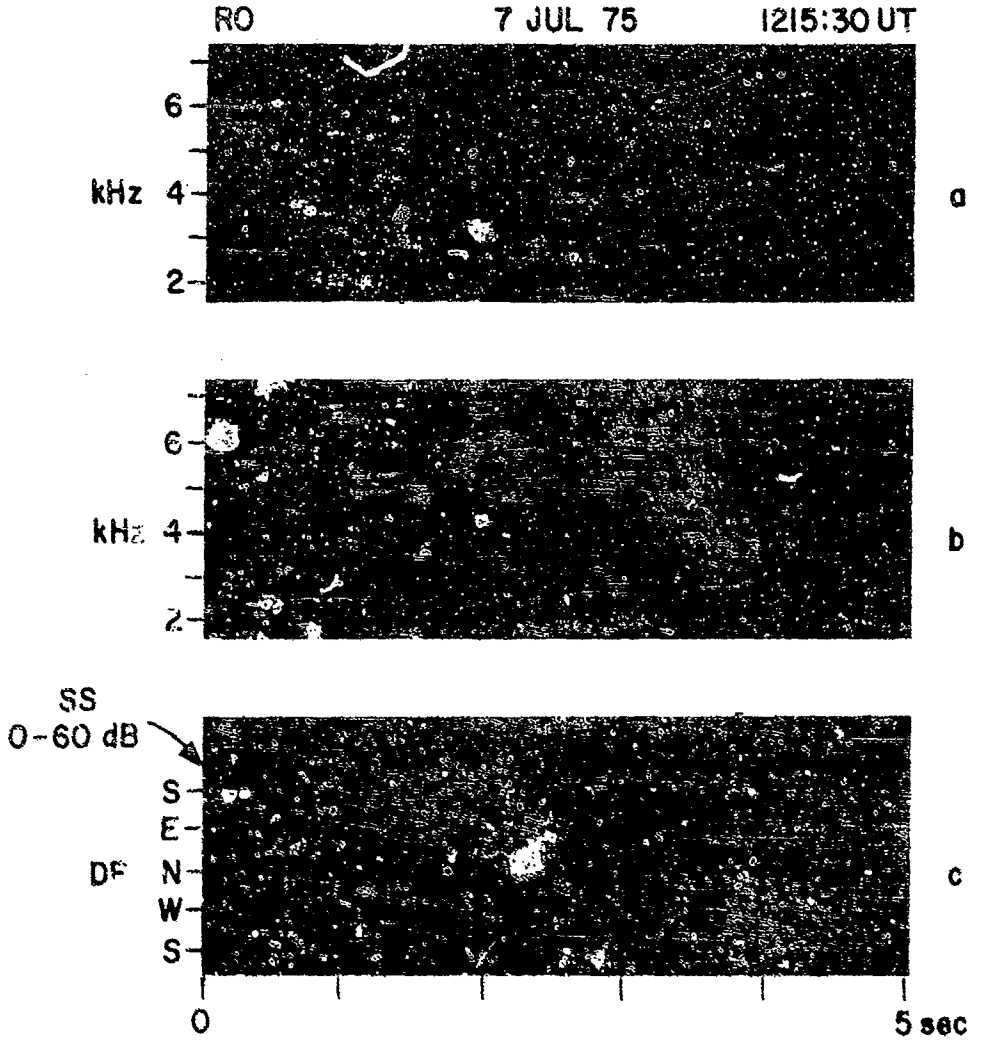


FIGURE 4.9 A DIFFUSE WHISTLER WITH STRONG PRECURSOR EMISSION. (a) Spectrum analysis showing diffuseness of whistler. (b) Mixed VLF and tracking frequency record. Diffuse nature of whistler causes tracker to follow only the general energy maximum. (c) Bearing indications showing gradually changing bearings from southwest to southeast on precursor and extremely confused bearing on whistler.

analysis in (a) shows a strong precursor emission and an extremely diffuse multicomponent nose whistler. The whistler was so diffuse that the frequency tracker could only follow the general energy maximum of the spectrum; the bearing indication in (c) is accordingly very confused. The precursor displays better coherency. Its bearing indication shows less rapid variation, although a pronounced variation with frequency is evident as the bearing drifts from southwest, through south, to a final reading near southeast. This frequency variation may be considered evidence of polarization error, which in turn suggests a moderately high elevation angle of arrival. As a broader data base is gathered, direction-finding studies may prove of value in determining the origin and propagation path of the less understood emissions such as precursors.

VLF emissions not associated with whistlers were also observed at Roberval. On 10 July 1975, a buildup of chorus activity occurred. Initially, the instrument had been set up to monitor for whistlers at 3.3 kHz. In Fig. 4.10, two hook-type emissions associated with chorus are tracked, as shown by the tracking frequency trace in (b), at 0 seconds and 4.5 seconds. Bearing indications in (c) are steady and consistent, displaying a (corrected) south-southwest direction. The operator then retuned the instrument to monitor at 2 kHz, causing tracking to occur on the chorus elements themselves as shown in Fig. 4.11. The bearing indications changed to west-southwest and displayed somewhat more variability, as one might expect from the multiplicity of components present in the chorus activity. Taken approximately

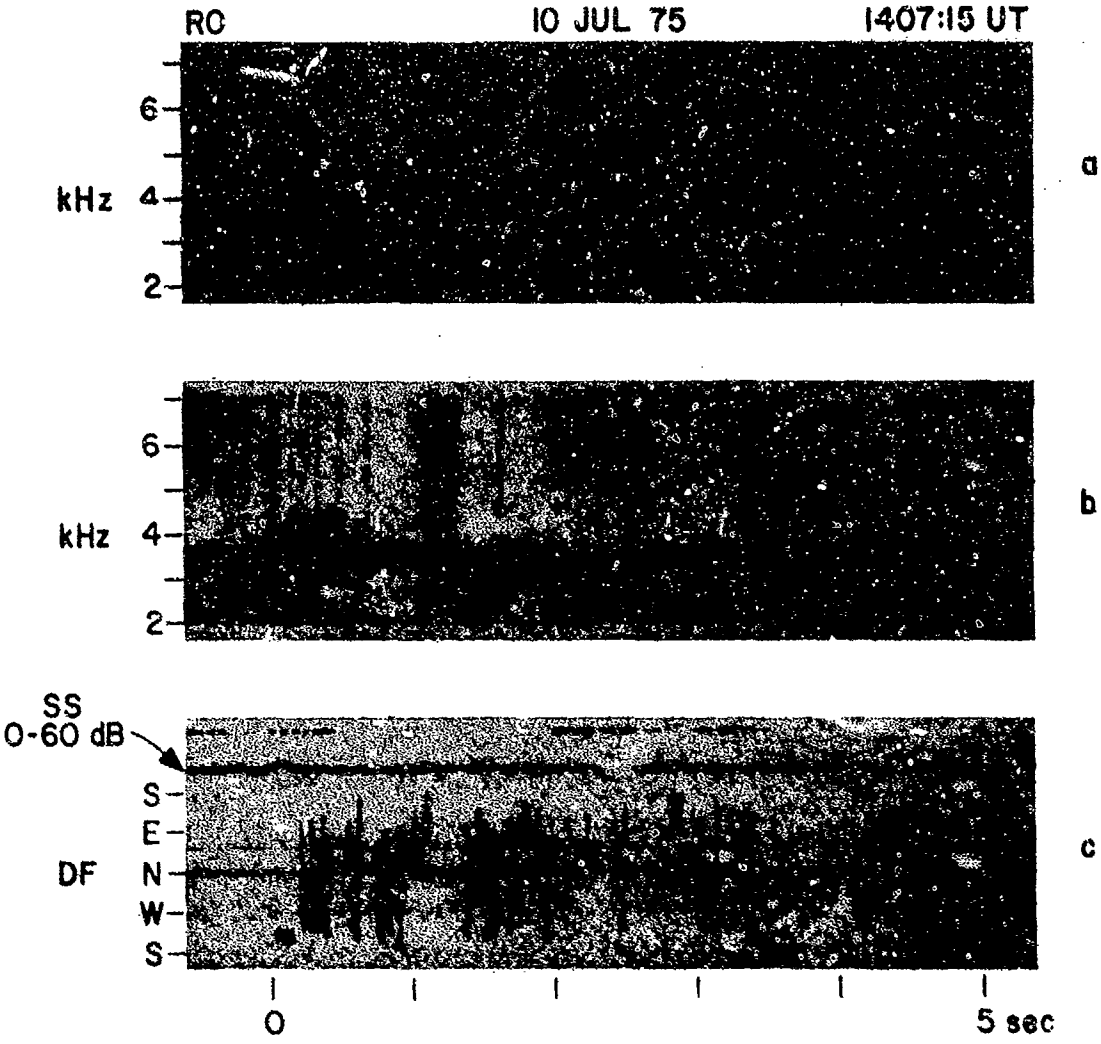


FIGURE 4.10 HOOK-TYPE EMISSIONS ASSOCIATED WITH CHORUS. (a) Spectrum analysis showing chorus and associated hooks at 0 and 4.5 seconds. (b) Mixed VLF and tracker record demonstrating capture of hooks by frequency-tracker waiting at 3.3 kHz. (d) Bearing indications showing steady south-southwest (corrected) direction for the hooks.

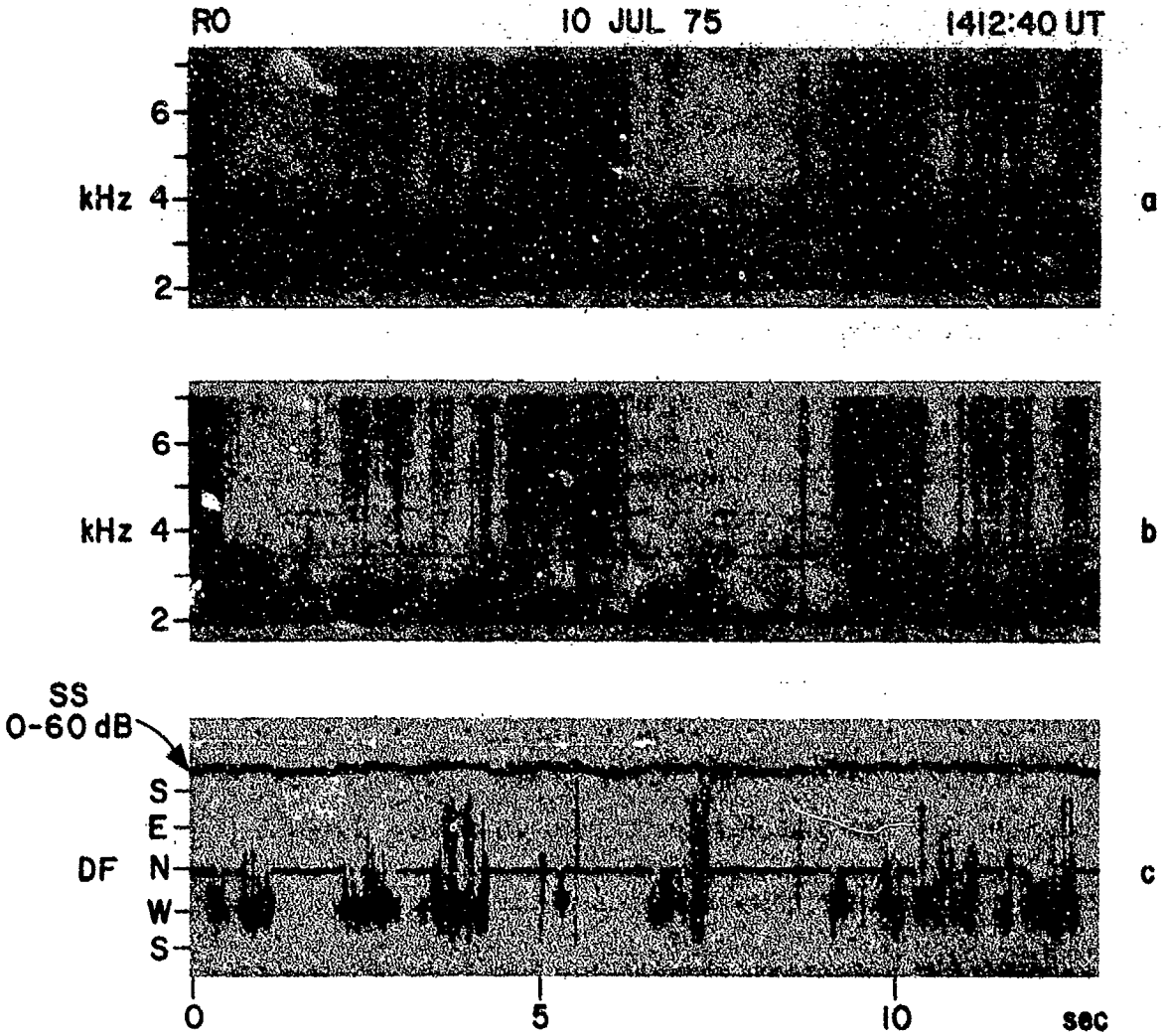


FIGURE 4.11 CHORUS. (a) VLF spectrum analysis. (b) Mixed VLF and tracker record shows tracking of chorus when instrument is adjusted to monitor at 2 kHz. (c) Bearing indications display predominantly west-southwest directions.

twelve minutes later, the example shown in Fig. 4.12 shows a bearing trace with a considerable amount of both rapid and slow variations indicative of polarization error. A possible explanation is a drift of the ducts carrying the chorus to a nearly overhead location. Drifts of this nature are of interest in studies of magnetospheric convection mentioned in Section I.B.1 as a motivating factor for direction-finding.

A more detailed example of temporal variations in the apparent angle of arrival is provided by Fig. 4.13, in which three successive 40-second samples taken 3 minutes apart on 28 July are displayed. In order to display the signals and directional data compactly, a single 0 to 20 kHz spectrum analysis of the VLF data mixed with the FM data channel is utilized. Sample (a) at 1539 hours shows whistlers and emissions displaying southerly bearings. In sample (b), the bearing data are frequently broken up due to the instrumental scale discontinuity at due south.† At 1545 hours, in sample (c), the signals have changed character, displaying more diffuseness and a lower whistler nose frequency; simultaneously, the bearing indications have moved to a south-southeast direction. Recalling from Figs. 4.6 and 4.7 the south-

†A scale discontinuity is unavoidable in representing a continuous angular variable on a finite linear scale. For signals incident near the discontinuity the indication may jump erratically between the extremes of the linear scale. If the choice of south as the discontinuity proves inconvenient, the phase of the vertical antenna signal can be reversed to reflect all angles through the origin, placing the discontinuity at north instead.

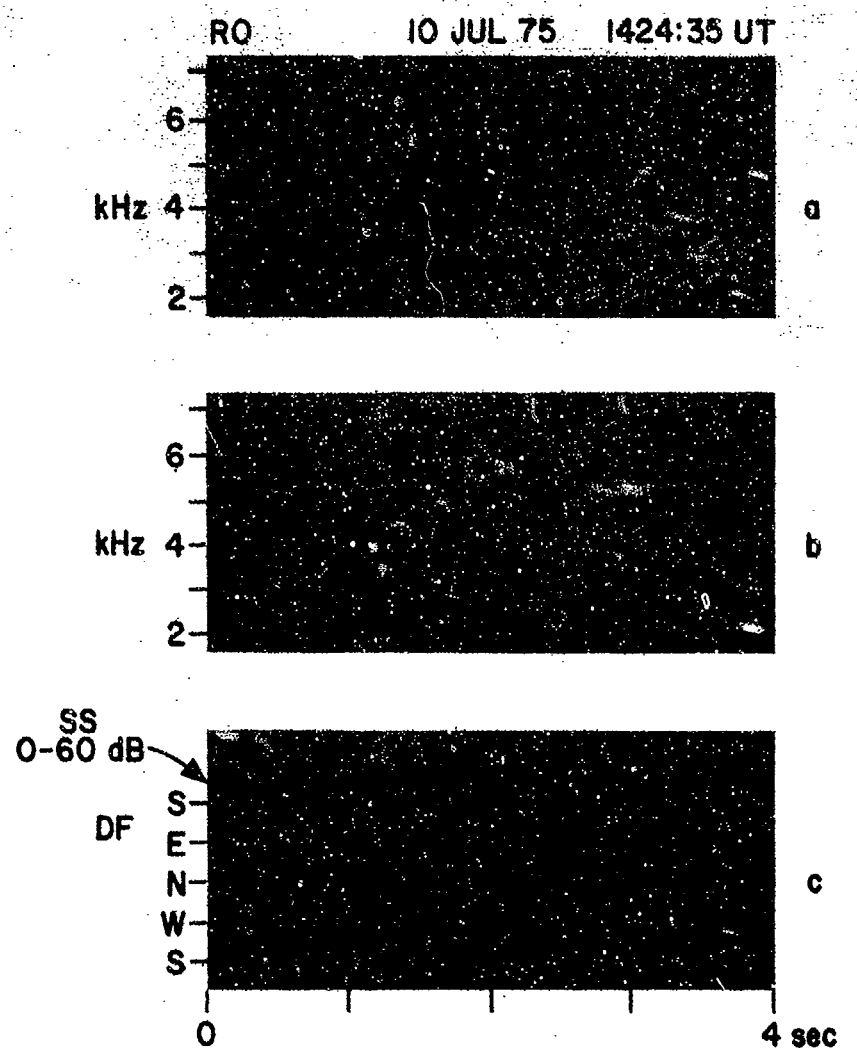


FIGURE 4.12 CHORUS. (a) VLF spectrum analysis. (b) Mixed record showing tracking of chorus elements. (c) Bearing indications show both slow and rapid variations suggestive of polarization error and a high elevation angle of arrival. Compared with Fig. 4.11, a drift from west to overhead may be indicated.

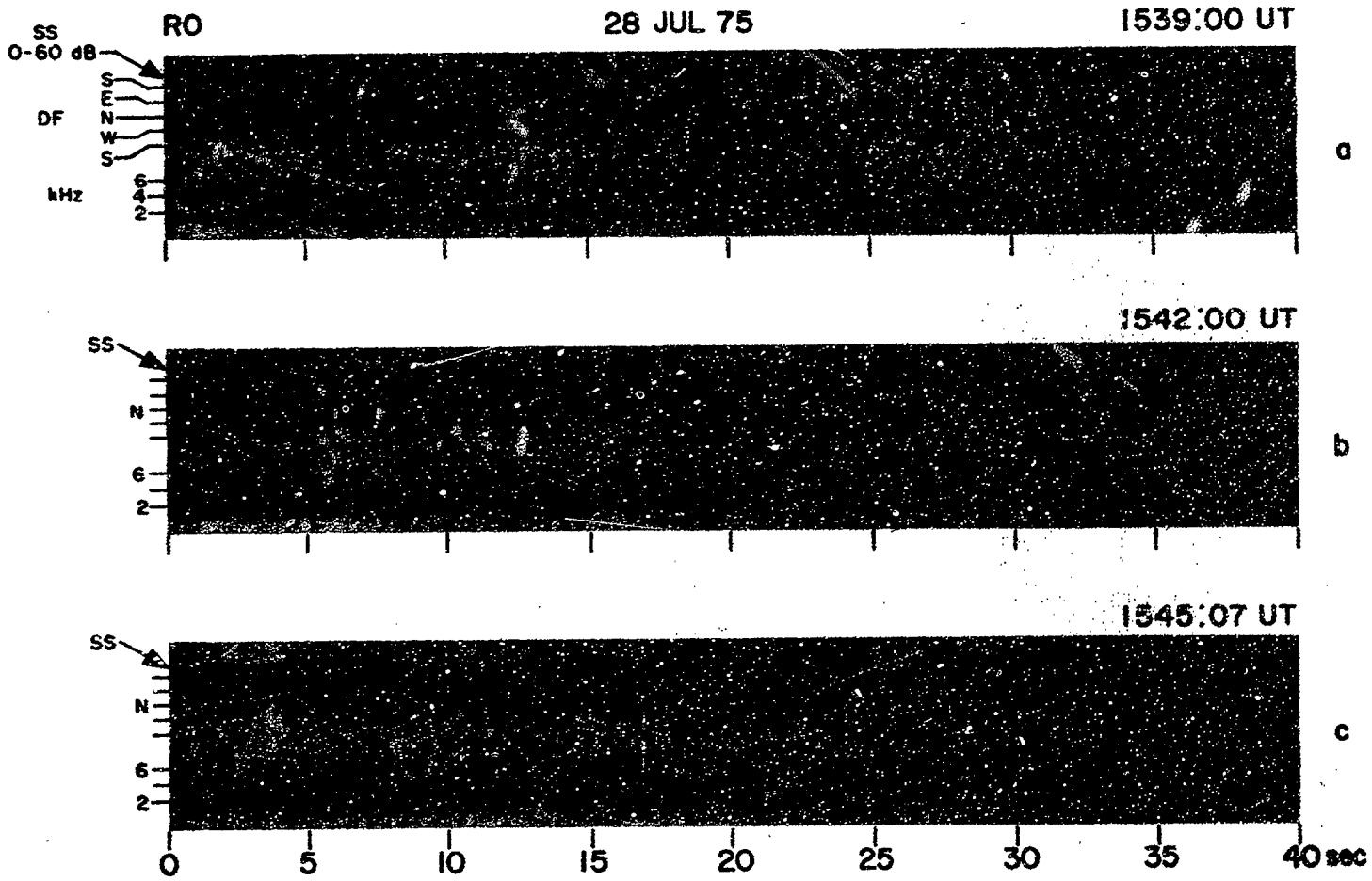


FIGURE 4.13 WHISTLERS AND EMISSIONS SHOWING DRIFT IN DIRECTION OF ARRIVAL. Each record includes VLF spectrum mixed with FM data channel containing tracking frequency, signal strength, and directional data. (a) Sample at 1539 shows south-southwest bearings. (b) Next sample at 1542 displays broken bearings due to scale discontinuity at due south. (c) Record at 1545 showing south-southeast bearings.

southwest bearings at 1530 hours, a possible picture of a northeast drift is evident. While further analysis and a broader data base are required before direct confirmation of duct drift theories can be presented, these examples do provide evidence of the usefulness of the direction-finder in such investigations.

4. Artificially Stimulated Emissions from Siple Station, Antarctica.

Roberval is located at the magnetically conjugate point to Siple Station, Antarctica, where Stanford University operates a 100 kW VLF transmitter for probing of the magnetosphere [Helliwell and Katsufrakis, 1974]. Signals transmitted at Siple stimulate emissions and display amplification when received at Roberval. The operation of the prototype frequency-tracking direction-finder at Roberval coincided with a campaign of experimentation employing the Siple transmitter, and signals from Siple were observed on several occasions. The programs transmitted included CW pulses, frequency ramps, and frequency sawtooth sequences.

A typical reception of frequency ramps from Siple is illustrated in Fig. 4.14. In (a), the VLF spectrum analysis shows the repeated ramps followed by a descending "staircase" sequence. Also visible are the idler pulses used during key-up conditions to maintain the load on the transmitter but which are amplified much less than the ramps. The mixed VLF and tracker record (b) demonstrates the successful tracking of the signal frequency by the instrument, including the ramps and descending staircase.

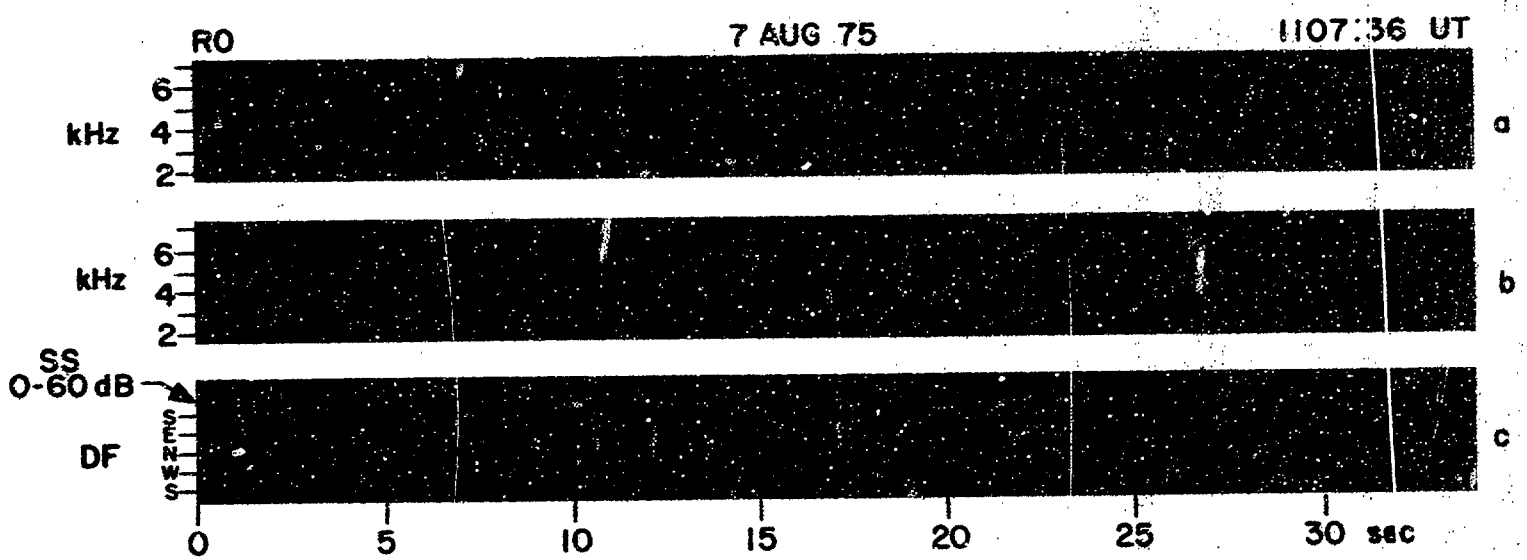


FIGURE 4.14 SIGNALS FROM SIPLE STATION RECEIVED AT ROBERVAL VIA MAGNETOSPHERIC PATHS. (a) Spectrum analysis displays frequency ramps and descending staircase sequence. (b) Mixed VLF and tracking-frequency record demonstrates tracking of signals by the instrument. (c) Direction-of-arrival indications are consistent from pulse to pulse and indicate a north-northwest corrected direction, with some frequency variation suggestive of polarization error caused by a high elevation angle of arrival from a duct nearly overhead.

The bearing trace in (c) shows a characteristic frequency-dependent variation during the first part of each pulse which may indicate polarization error due to a relatively high angle of arrival. The bearing signature repeats for each successive pulse. The bearings on the staircase steps agree with the bearing for the corresponding frequency within the ramps, although the changes are harder to detect due to the noisiness of the trace. From the north to northwest bearing and the presence of polarization error, an exit point near the station and to the north would be inferred. This is consistent with analyses of nose whistlers from the same period, which show nose frequencies of approximately 3.2 kHz.

Additional examples from the same date are provided in Figs. 4.15 and 4.16. In 4.15, an apparent short term change in the polarization error characteristics occurs. At 1108:51, the whistler and Siple signal show the same frequency-dependent bearing variations as in Fig. 4.14. At 1109:36, however, the bearing variation with frequency has changed in character. This rapid change is consistent with the sensitivity of the polarization ellipse to small changes in elevation angle as the multiple rays from the exit point to the receiver shift relative to one another. The example of Fig. 4.16 illustrates the effect of multipath versus single component reception conditions on the bearing indication. In the example at 1109:27, the spectrum analysis at (a) displays multipath conditions on the Siple ramp and nose whistler. The tracking frequency trace in (b) shows a characteristic fuzziness indicating low coherence. At (c) the directional indication, although indicating

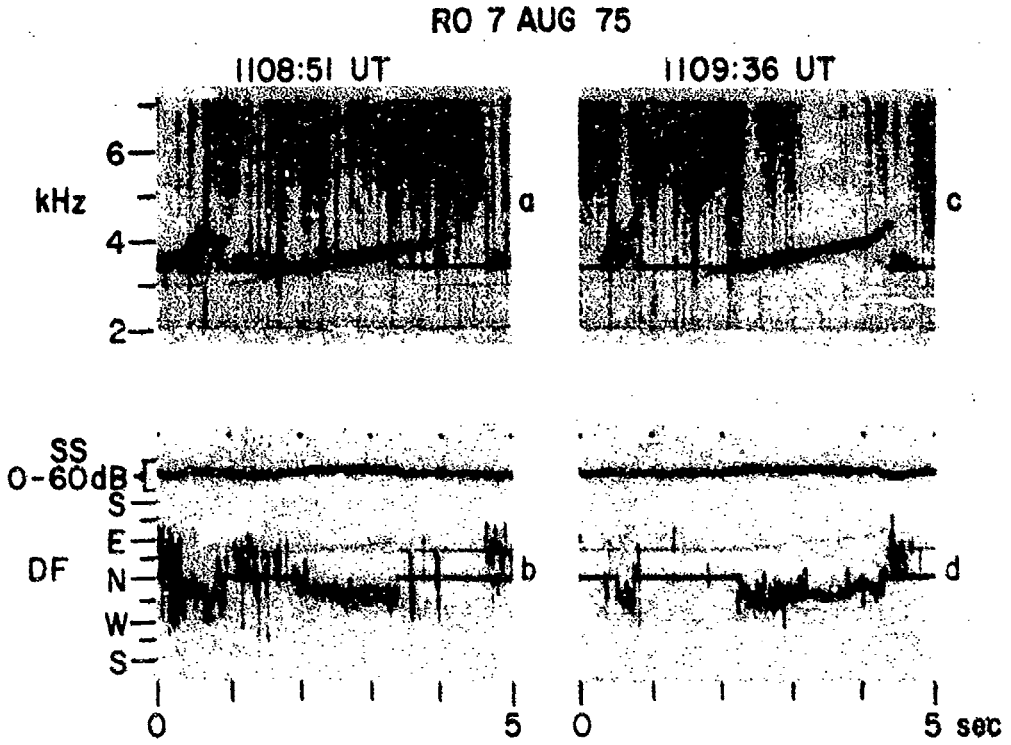


FIGURE 4.15 SIPLE SIGNALS SHOWING CHANGING POLARIZATION ERROR. (a) and (c) Spectrum analysis of VLF mixed with tracking frequency indication for two ramps separated by approximately one minute (b) and (d) Direction-of-arrival data showing a distinct difference in the bearing behavior through the ramp duration. A change in polarization conditions may be inferred.

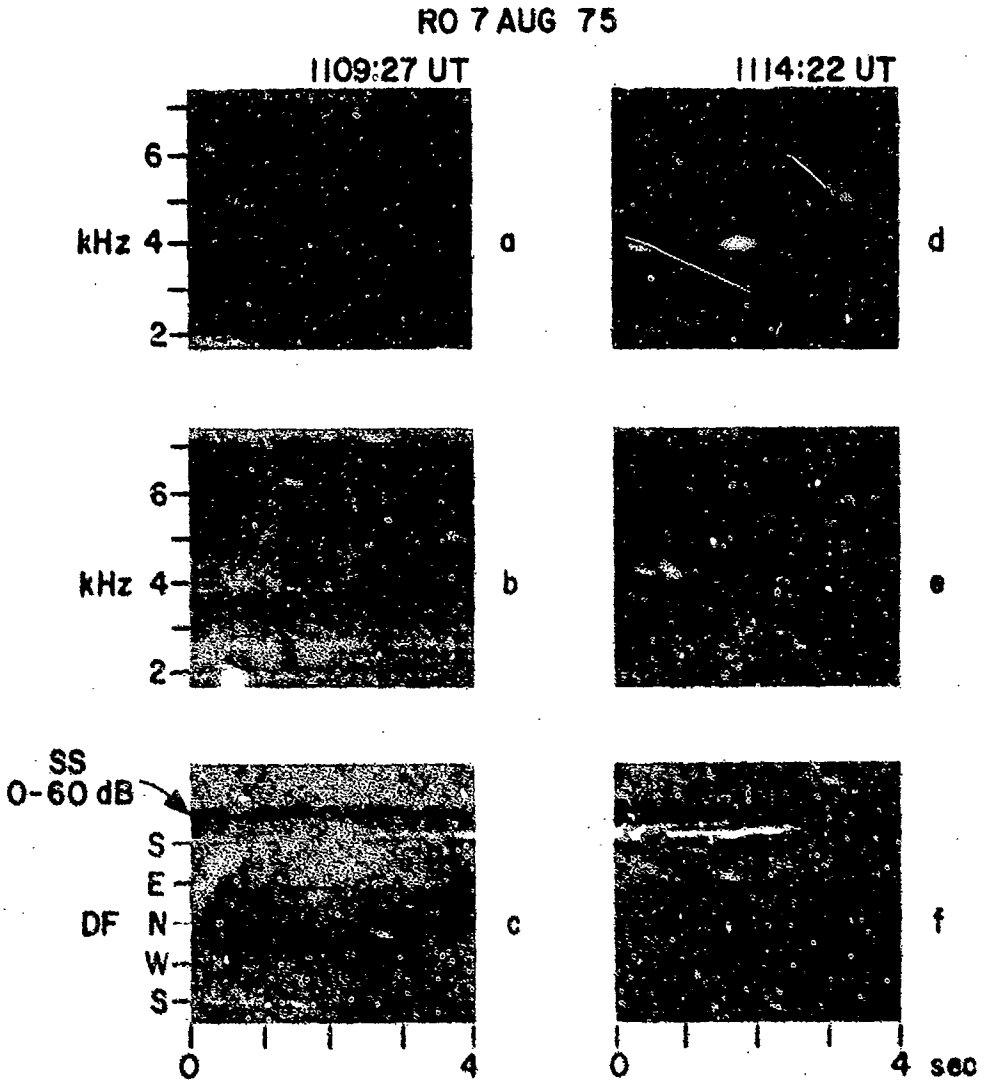


FIGURE 4.16 SIPLE SIGNALS SHOWING EFFECTS OF MULTIPATH. (a) Spectrum analysis of Siple ramp and a nose whistler displaying multipath conditions. (b) Tracking-frequency trace and VLF mixed record showing successful tracking but noisy trace indicative of low coherence. (c) Bearing indications show a consistent average but considerable rapid variation. The example of 1114 (d) shows less multipath. (e) Frequency tracking trace for latter part of ramp is sharply defined. (f) Bearing indication is more consistent.

a consistent average, is subject to a great deal of rapid periodic variation. In contrast, the example at 1114:22 shows less multipath in the spectrum analysis (d), and a more clearly defined tracking frequency trace in (e) for the lattern portion of the Siple ramp. The corresponding bearing indication (f) shows less variability.

An even more extreme case of multipath is given in Fig. 4.17. The bearing indication (c) is extremely confused except for brief instants at 2.0 seconds and 12.0 seconds. A study of the spectrum (a) and the tracking frequency record (b) shows that relatively coherent triggered emissions carried the tracker frequency away from the multicomponent sawtooth signal from Siple at these times. The tracking frequency trace as recorded on a chart recorder (b) shows a striking change from a fuzzy character to a clean trace during these emissions, indicating the higher degree of frequency coherence for the emissions.

A glimpse at another application of the instrument is provided in Fig. 4.18. In addition to the familiar quantities of direction-of-arrival (c), signal-to-noise ratio (d), signal strength (e), and tracking frequency (f), the real and imaginary parts of the ratio $(-H_x/H_y)$ (which are also measured by the instrument) are shown at (b) and (a). Noting that the imaginary part is negative and greater than the real part during reception of the ramps from Siple, one can conclude that the polarization is essentially circular. The handedness can also be ascertained from the sign of $H_x/H_y$: as $(-H_x/H_y)$ is

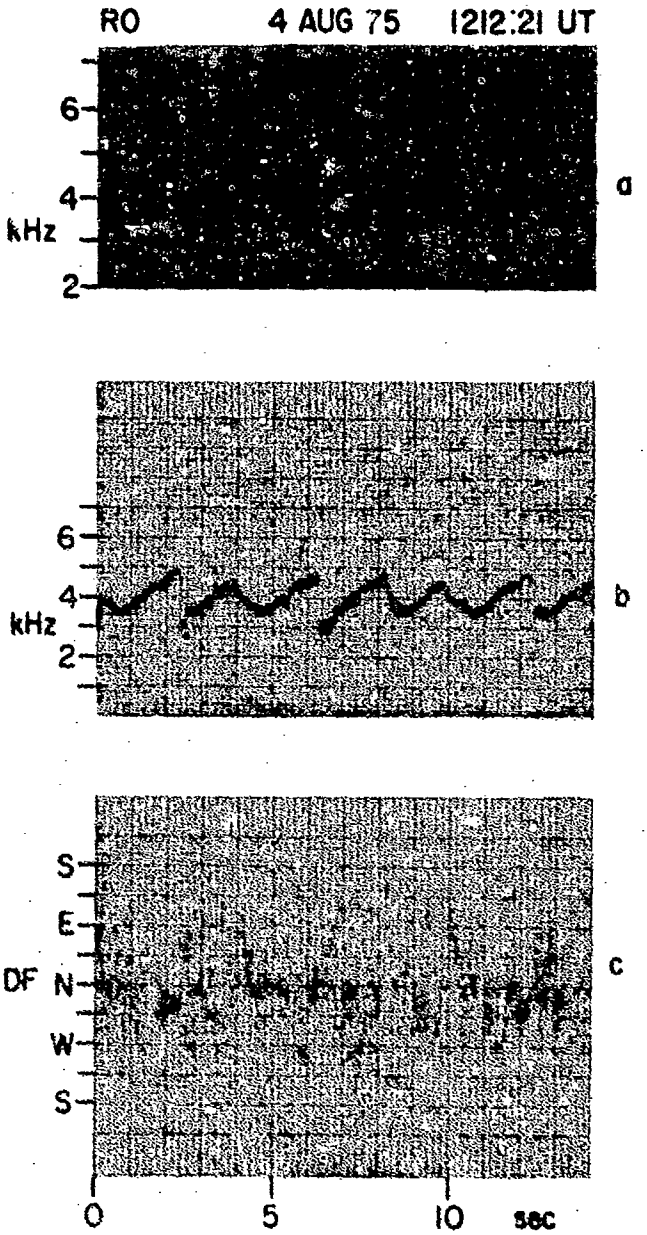


FIGURE 4.17 SAWTOOTH SIGNAL FROM SIPLE AND TRIGGERED EMISSIONS. (a) VLF spectrum analysis showing multipath reception of Siple sawtooth. (b) Tracking frequency chart record displays triggered emissions tracked at 2.0 and 12.0 seconds. Trace character becomes sharper indicating higher coherence for these emissions. (c) Bearing record is extremely confused due to multipath, with the exception of the two emissions.

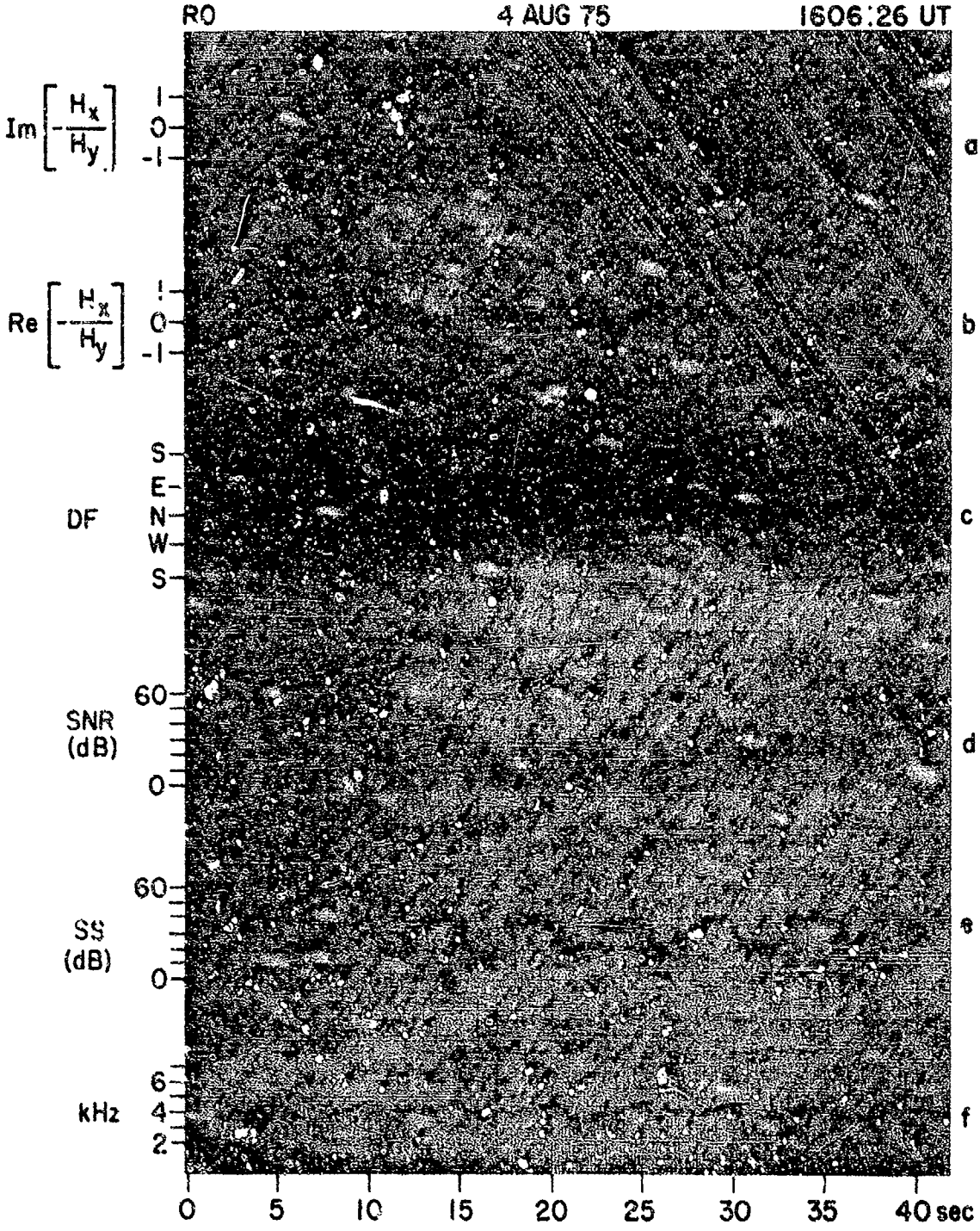


FIGURE 4.18 CHART RECORD INDICATING POLARIZATION OF RECEIVED SIPLE RAMPS. (a) and (b) Measurements of the real and imaginary parts of the ratio ($-H_x/H_y$) are recorded. (c) Bearing signature shows considerable frequency variation indicative of high elevation angle. (f) Frequency record showing tracking of ramps. The polarization of these signals is essentially right-hand circular as deduced from (a) and (b).

indicated as negative, $H_x/H_y$ must be positive; therefore, $H_x$ leads $H_y$. The polarization must be right hand circular (looking down at the receiving site, in the direction of propagation). This agrees with Helliwell's [1965] description of the polarization of whistler-mode waves. The indication of circular polarization strongly suggests a high elevation angle of arrival and a near-overhead duct. Again, this is in agreement with nose frequency observations of 3.1 to 3.6 kHz on this date.

# V. CONCLUSIONS

## A. SUMMARY OF RESULTS

A theory and technique for tracking the frequency of whistlers and related VLF emissions and extracting direction-of-arrival data in real time has been presented. A prototype instrument embodying these innovations has been designed and constructed, and tested both in the laboratory and at field observing sites.

Laboratory tests of the tracking capability show that, with a 340 Hz IF filter bandwidth, signals changing frequency at up to 32 kHz/second can be captured and tracked at signal-to-noise ratios as low as 6.7 dB. At field observing sites, successful tracking was achieved for whistlers, both above and below the nose frequency, and on a variety of emissions, chorus, and Siple transmitter signal formats, in the presence of both manmade and atmospheric noise.

Laboratory tests of the direction-finding capability show an instrumental accuracy of $1.25^{\circ}$ RMS. Field observations on several VLF transmitting stations show repeatable, accurate results, with the average magnitude of the error being $2.9^{\circ}$, most of which is attributable to site error.

Direction-finding bearings were obtained on whistlers, spherics, chorus, Siple signals, and related emissions. The behavior of the bearing indications agrees with the theoretical prediction of system behavior in the presence of noise, multipath, and polarization error. Under favorable conditions, repeated, consistent bearings were obtained.

The bearing results on these signals were consistent with the exit point latitudes predicted from whistler nose frequency analysis, without the necessity of invoking deviations of the ray path from the field line of the duct.

Some of the data display a temporal change in the indicated bearing which may be indicative of a duct drift.

## B. CONCLUSIONS

The new technique for VLF direction-finding presented herein fills a gap in the range of techniques currently available or under development. The directional data are of higher accuracy and temporal resolution than those produced by the goniometer technique. The instrument is of use against a wider variety of signals and wave incidence conditions than the multi-channel techniques of Cousins [1972] or Tsuruda and Hayashi [1974]. Finally, the availability of the information in real time and with a minimum of human analytical effort represents an advantage over both of the other methods. The practicality of the instrument has been demonstrated by the success of the field observation program. The frequency-tracking direction-finder promises to yield data hitherto unavailable on the location of the ducts which carry whistlers and related signals.

## C. FUTURE APPLICATIONS

A number of different opportunities for application of the instrument are apparent. To further exploit the direction-finding capability, it is recommended that a multistation network be employed. Two stations would permit location of sources by triangulation. Three of more stations would provide a further check on the system accuracy by examining the convergence of the bearings to a single point.

The capability of the instrument for measuring the apparent polarization of the incident wave, as illustrated in Fig. 4.18, could be further exploited. If a perfect circularly polarized source is assumed at the base of the ionosphere, the polarization of the received signal can be used to indicate the elevation angle to the source; the more nearly circular the polarization, the higher the elevation angle.

Another mode of operation has been tested, in which the signals from the three antenna elements are recorded on a three-channel tape recorder for later playback and processing by the frequency-tracking direction-finder. This method requires excellent phase and amplitude response matching between the recorder channels. However, the advantage is that only one direction-finding instrument is required to analyze data from any number of stations. Furthermore, more detailed analysis of signals is possible by replaying the tape with different adjustments of the instrument. Preliminary tests have shown this to be a feasible approach. The direction-finding errors introduced are on the order of a few degrees for a properly

operating recorder; for an improperly aligned machine, the errors may reach 5 to 15 degrees.

Apart from the direction-finding function the frequency-tracking receiver has demonstrated useful capabilities in the unattended detection and analysis of VLF activity. Unattended reception facilities at remote locations or on satellites employing the frequency-tracking principle can benefit from the reduction in data bandwidth made possible by automatic real-time extraction of frequency, amplitude, and signal-to-noise ratio information.

A more immediate application of the receiver is in the measurement of the growth rate of the artificially stimulated emissions from the Siple signal. Use of ordinary filtering techniques is hampered by the changing frequency of the emissions; using the tracking receiver, a continuous record of the amplitude of the emission can be produced with other noise filtered out. Preliminary experiments along this line have been carried out with success. A minor redesign of the IF filters to reduce their bandwidth to 100 Hz would optimize the instrument for this application; although the maximum tracking rate capability would be reduced by a factor of ten, it would still be adequate for the relatively slow frequency variations of the Siple signals.

## APPENDIX A. COMPARISON OF SMALL AND LARGE APERTURE DIRECTION-FINDERS

Assume two model direction-finding systems, one of the large-aperture interferometric type and the other of the small-aperture type.

The interferometric direction-finder consists of two pairs of antennas, each pair forming a baseline of length s. The two baselines are orthogonal. The phase difference $\phi$ between the two antennas constituting each baseline is measured. If baseline 1 is oriented along the north-south axis, and baseline 2 is oriented east-west, then

$$\phi_1 = (2\pi/\lambda)s \cos \theta$$

$$\phi_2 = (2\pi/\lambda)s \sin \theta$$

The small aperture system consists of crossed loop antennas. The amplitudes of the signals from the two elements are given by

$$A_1 = A \cos \theta$$

$$A_2 = A \sin \theta$$

In the presence of random noise and measurement errors, the effect $\epsilon$ on a phase measurement (in radians) is comparable to the fractional effect on an amplitude measurement. That is,

$$\Delta\phi \text{ (radians)} = \Delta A/A = \epsilon$$

The noisy measurements produced by the two systems are therefore given by

$$\hat{\phi}_1 = (2\pi/\lambda)\, s \cos\theta + \epsilon_1 \qquad \hat{A}_1 = A\cos\theta + \epsilon_1 A$$

$$\hat{\phi}_2 = (2\pi/\lambda)\, s \sin\theta + \epsilon_2 \qquad \hat{A}_2 = A\sin\theta + \epsilon_2 A \ .$$

The resolution of the angle of arrival from the sine and cosine components measured is performed as

$$\hat{\theta} = \angle\left(\hat{\phi}_1 + j\hat{\phi}_2\right) \qquad \hat{\theta} = \angle\left(\hat{A}_1 + j\hat{A}_2\right) \ .$$

Substituting the above quantities and rearranging,

$$e^{j\hat{\theta}} = e^{j\theta} + \frac{\epsilon_1 + j\epsilon_2}{(2\pi/\lambda)s} \qquad e^{j\hat{\theta}} = e^{j\theta} + \epsilon_1 + j\epsilon_2 \ ,$$

from which it can be seen that the influence of the noise will be comparable when $(2\pi/\lambda)\, s = 1$, or $s = \lambda/2\pi$.

## APPENDIX B. CIRCUIT DIAGRAMS OF THE APPARATUS

Schematic diagrams of the circuitry used to implement the prototype frequency-tracking direction-finder are presented herein. Fig. B.1 gives a block diagram of the apparatus showing the functions performed on each circuit card and the interrelationships between the cards. The actual schematics of the cards, PC1 through 25 and PC27, are given in Figs. B.2 through B.26. The backplane wiring of the card cages holding the circuit modules is diagrammed in B.27 and B.28. The wiring of the control panels for the equipment is described by Figs. B.29 and B.30. A further insight into the operation of the equipment is provided by the drawings of the actual front panel controls, with explanations, in Figs. B.31 and B.32.

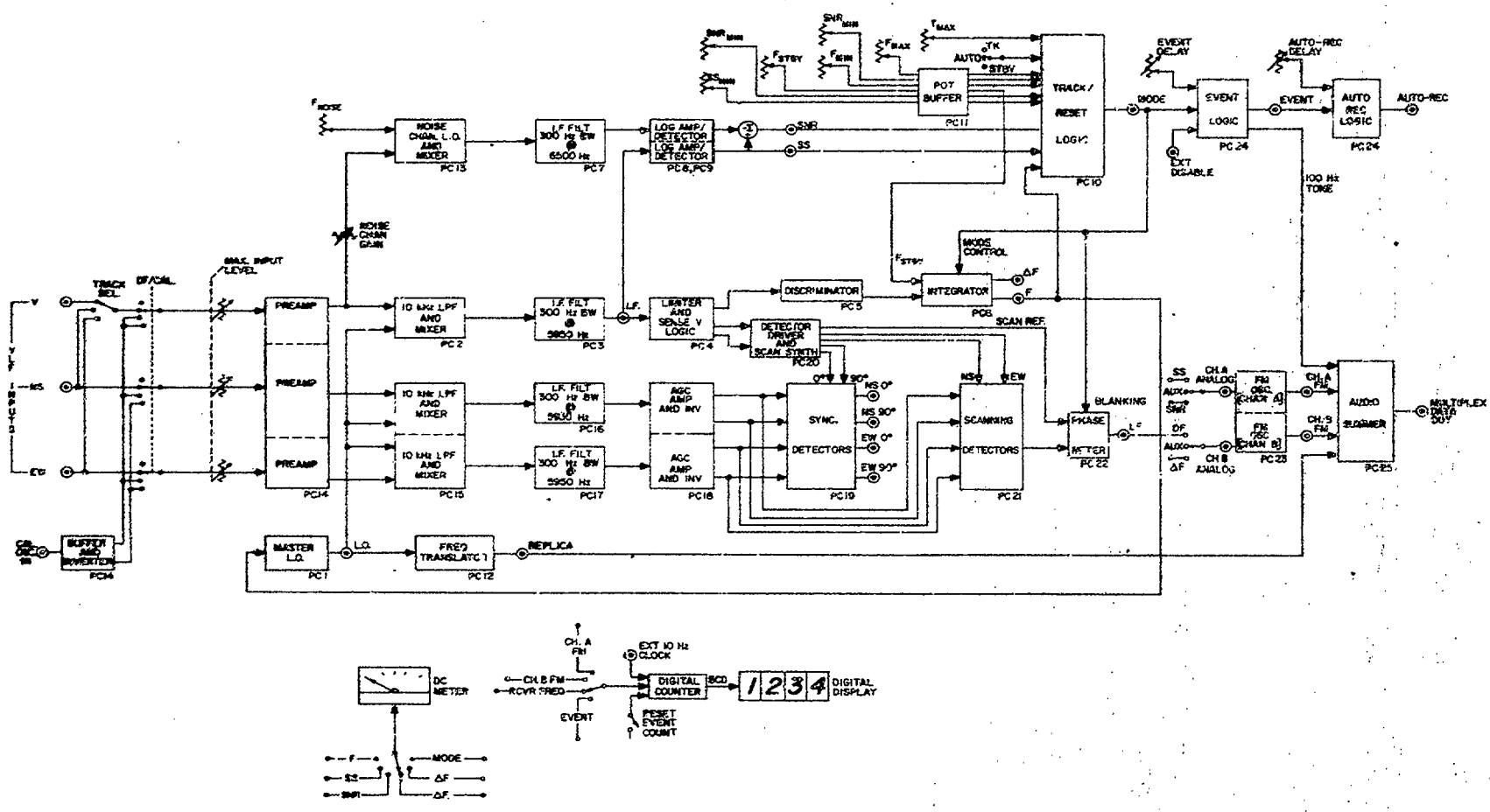


FIGURE B.1 BLOCK DIAGRAM OF THE INSTRUMENT SHOWING CIRCUIT CARD FUNCTIONS.

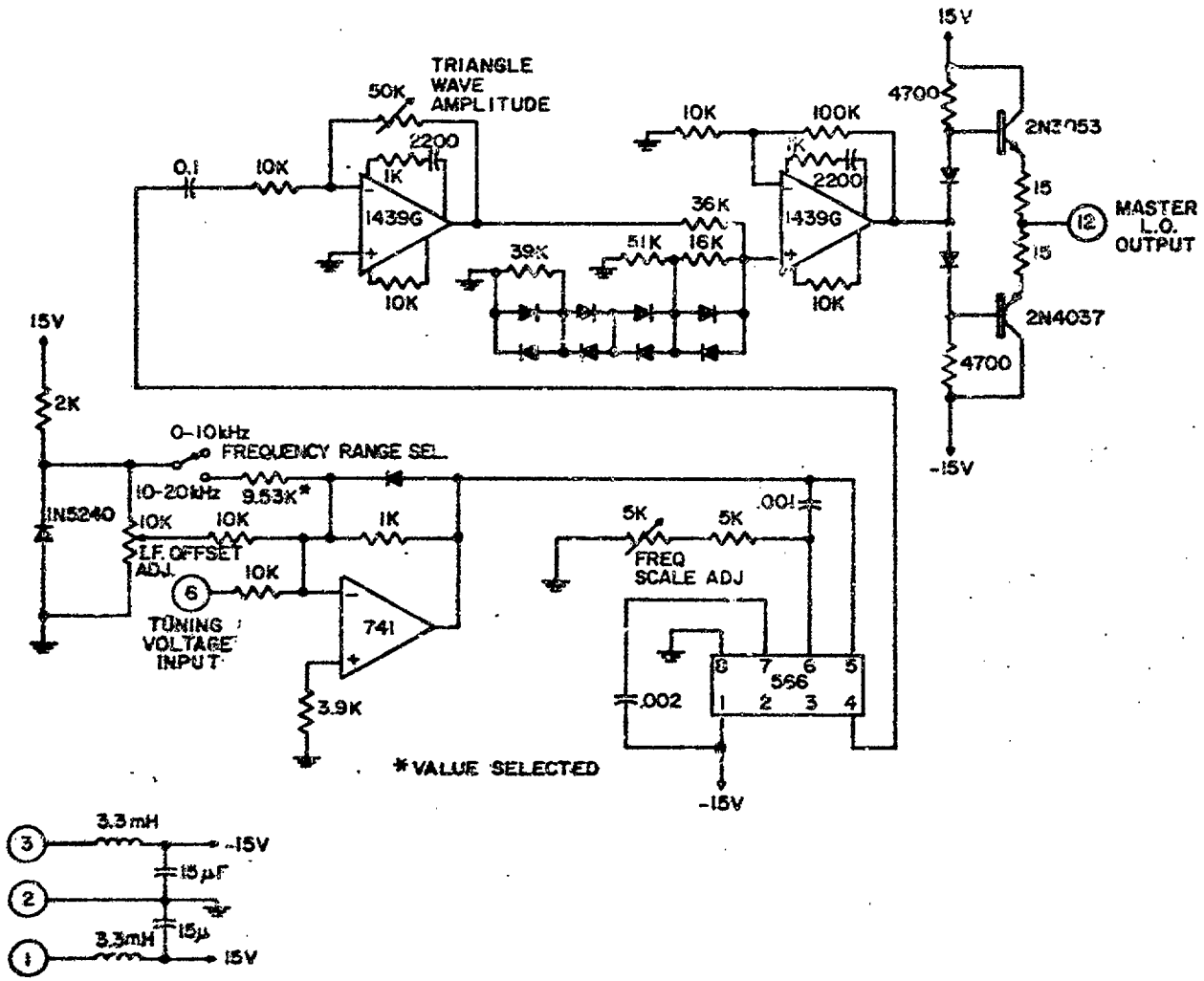


FIGURE B.2 SCHEMATIC OF MASTER LO CARD, PC1.

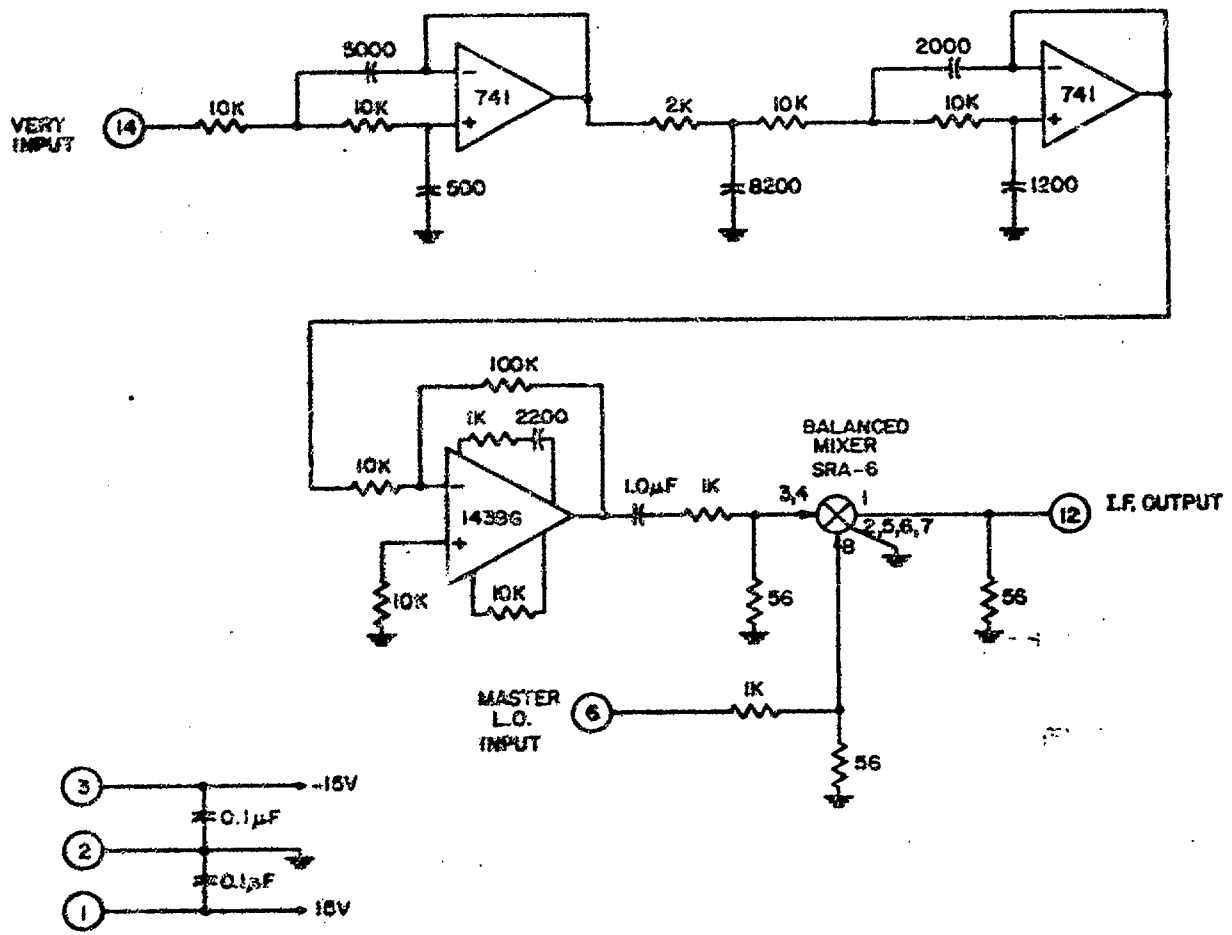


FIGURE B.3 SCHEMATIC OF MIXER-VERT CARD, PC2.

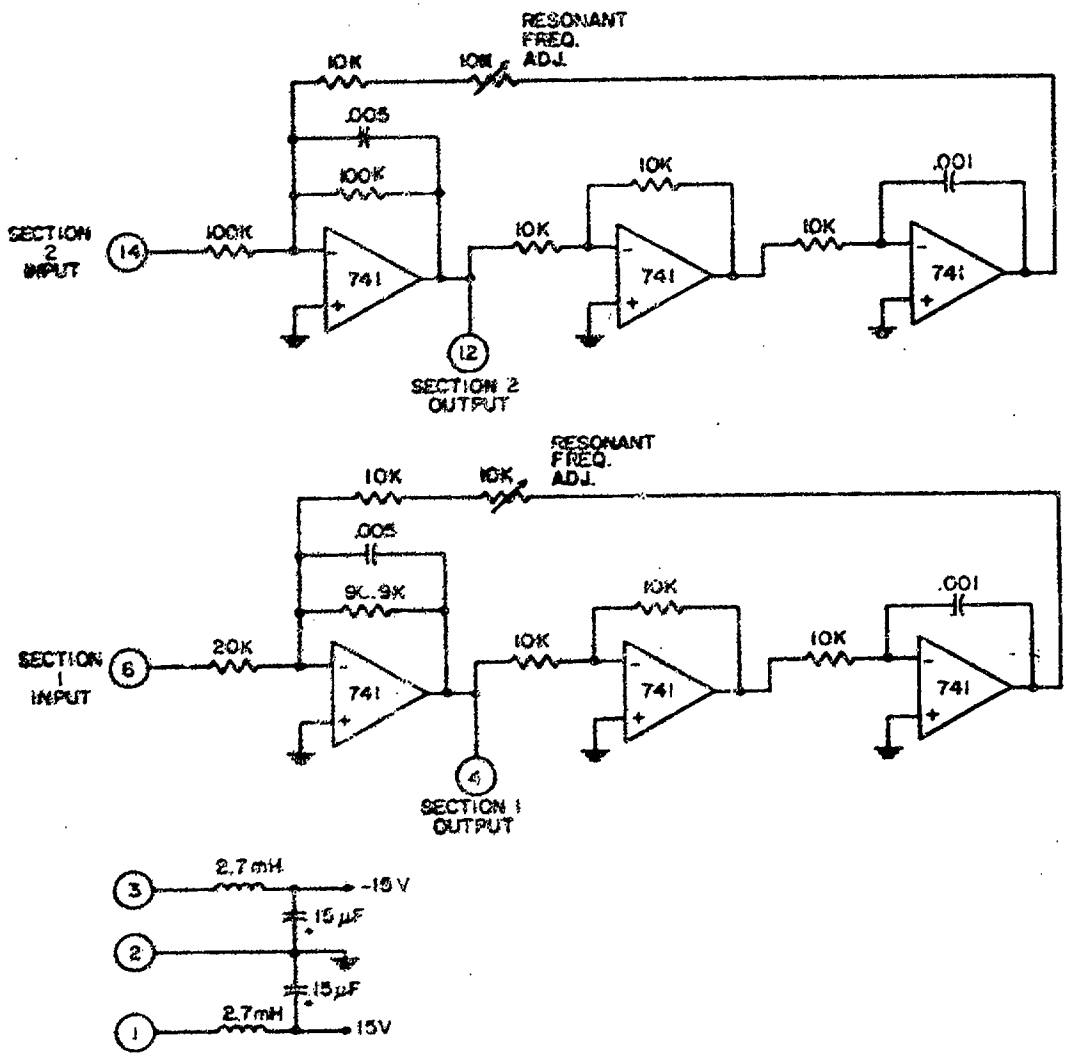


FIGURE B.4 SCHEMATIC OF IF FILTER-VERT CARD, PC3.

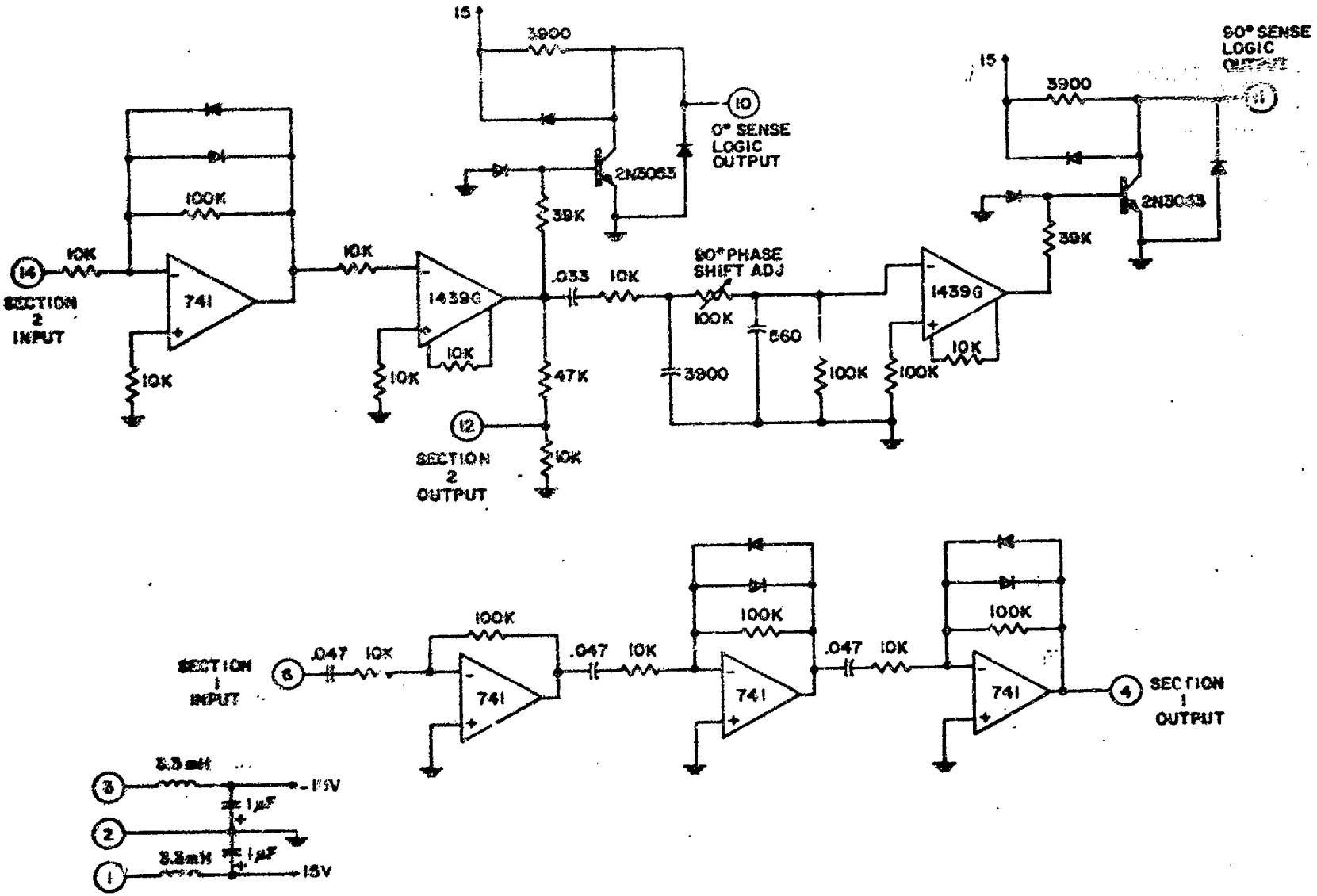


FIGURE B.5 SCHEMATIC OF LIMITER AMP CARD, PC4.

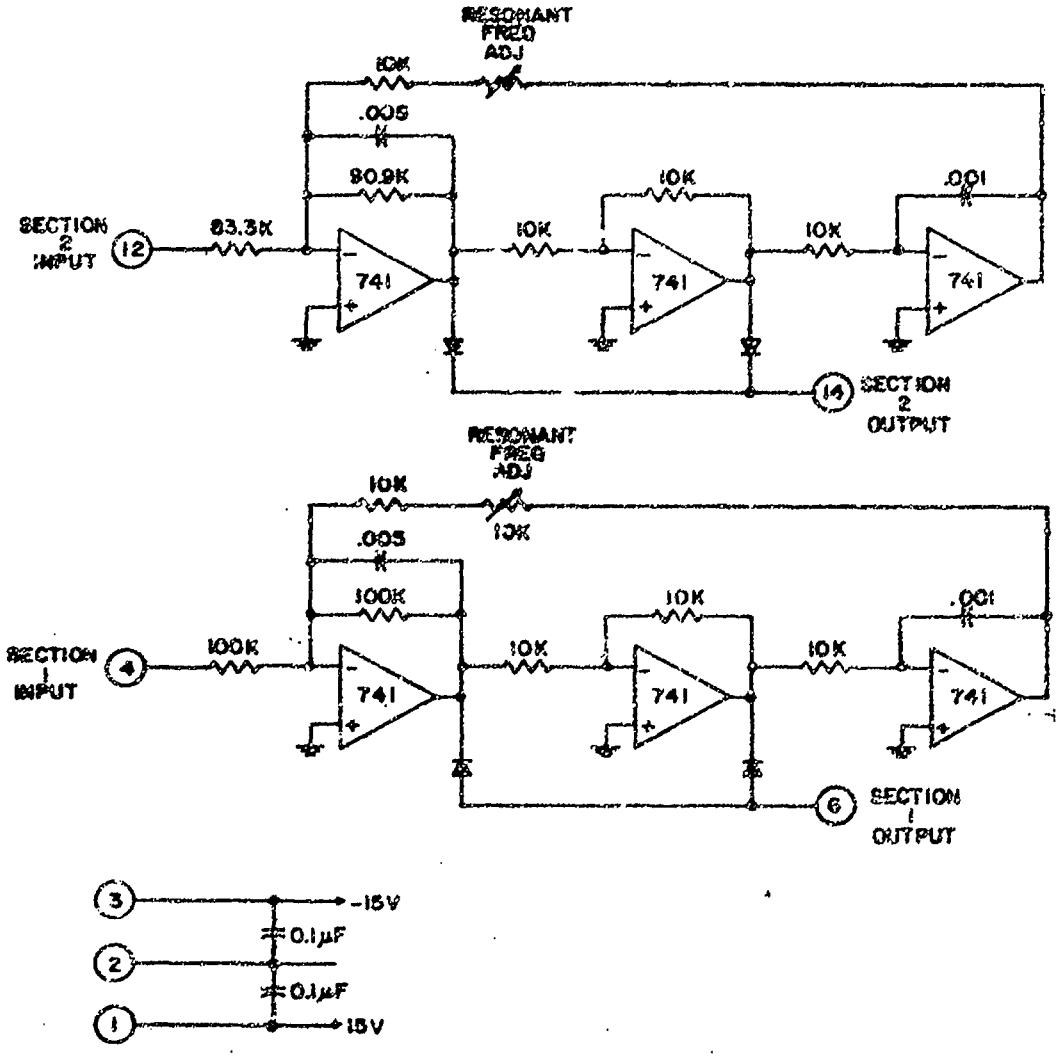


FIGURE B.6 SCHEMATIC OF DISCRIMINATOR CARD, PC 5.

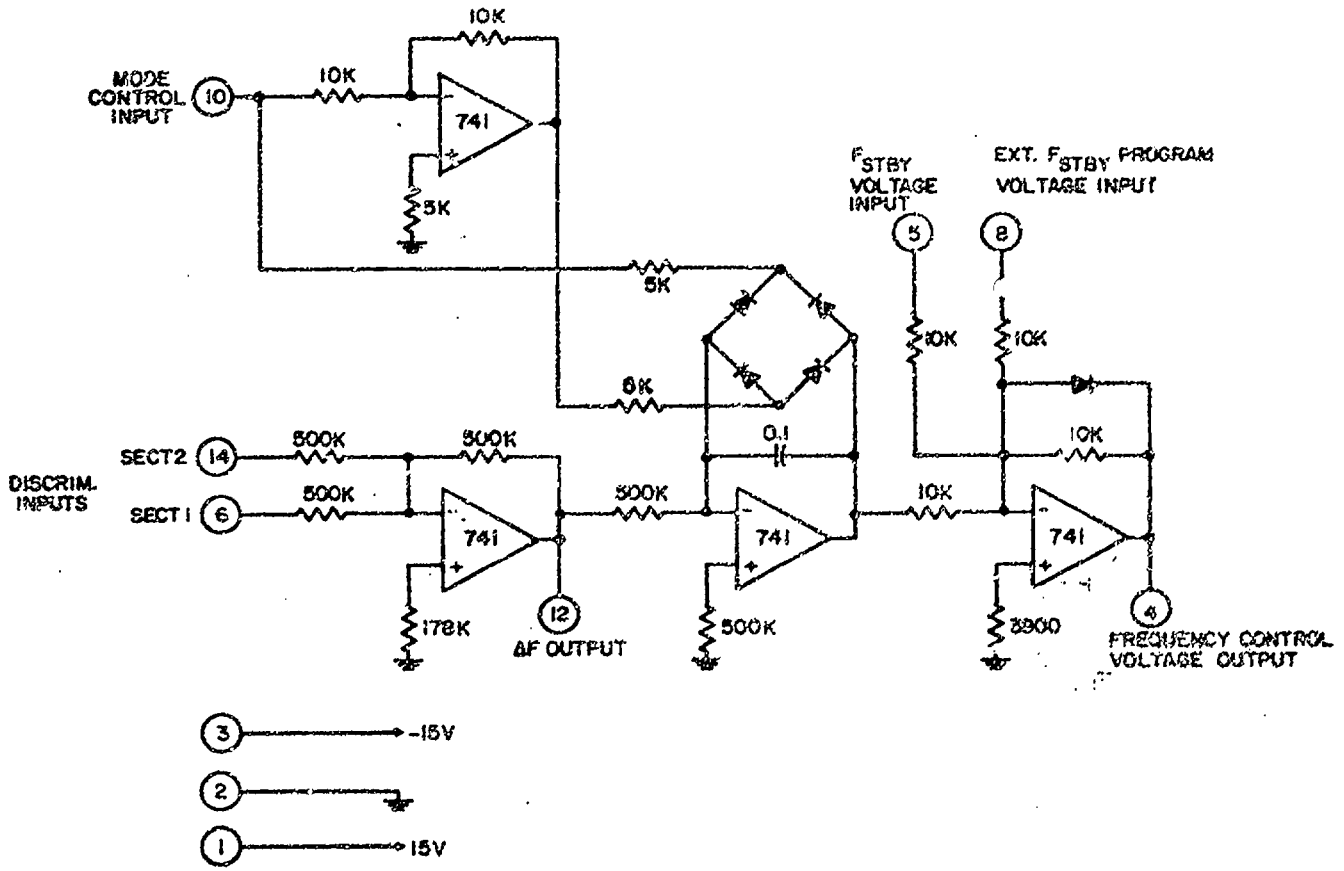


FIGURE B.7 SCHEMATIC OF INTEGRATOR CARD, PC6.

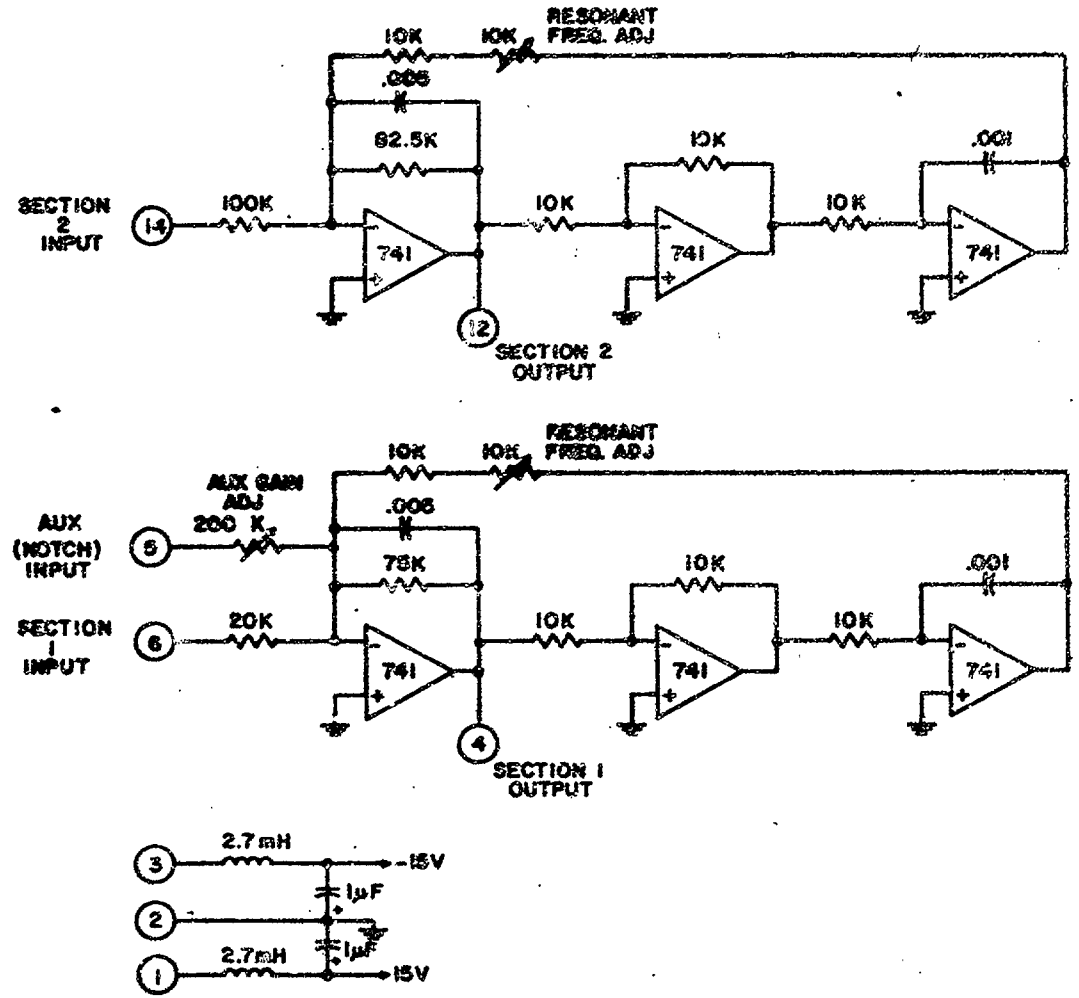


FIGURE B.8 SCHEMATIC OF IF FILTER NOISE CARD, PC7.

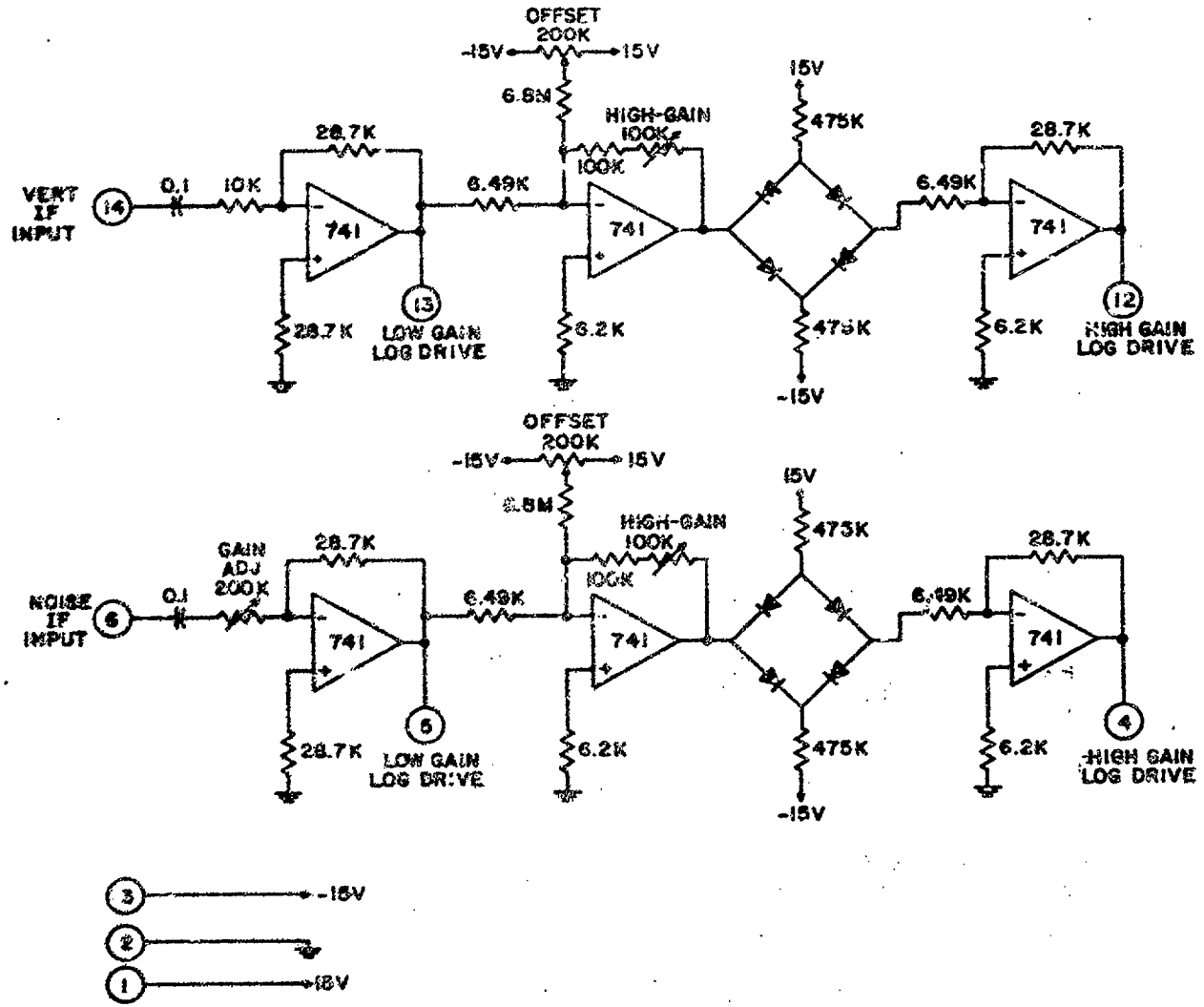


FIGURE B.8 SCHEMATIC OF LOG AMP DRIVER CARD, PC8.

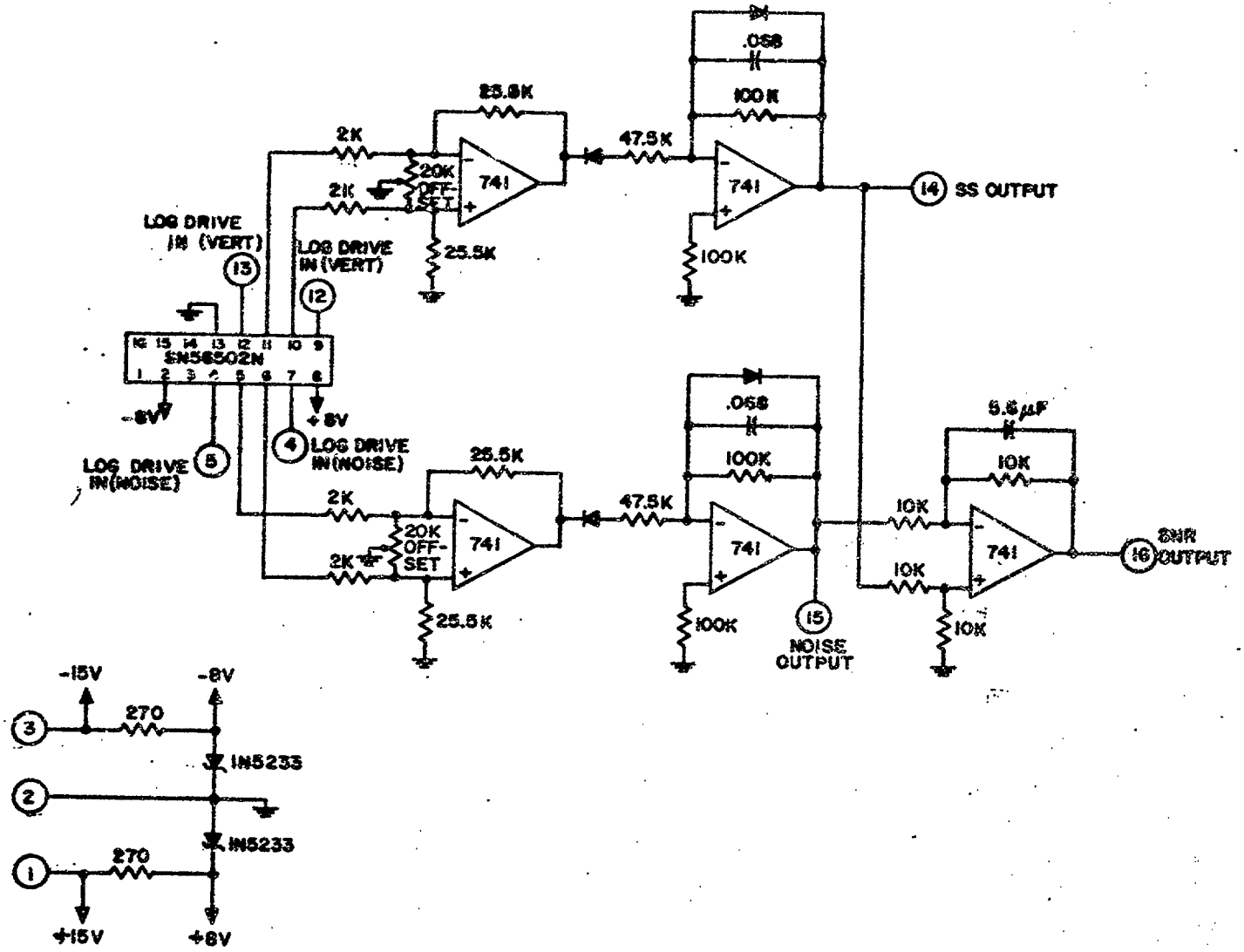


FIGURE B.10 SCHEMATIC OF LOG DETECTOR CARD, PC9

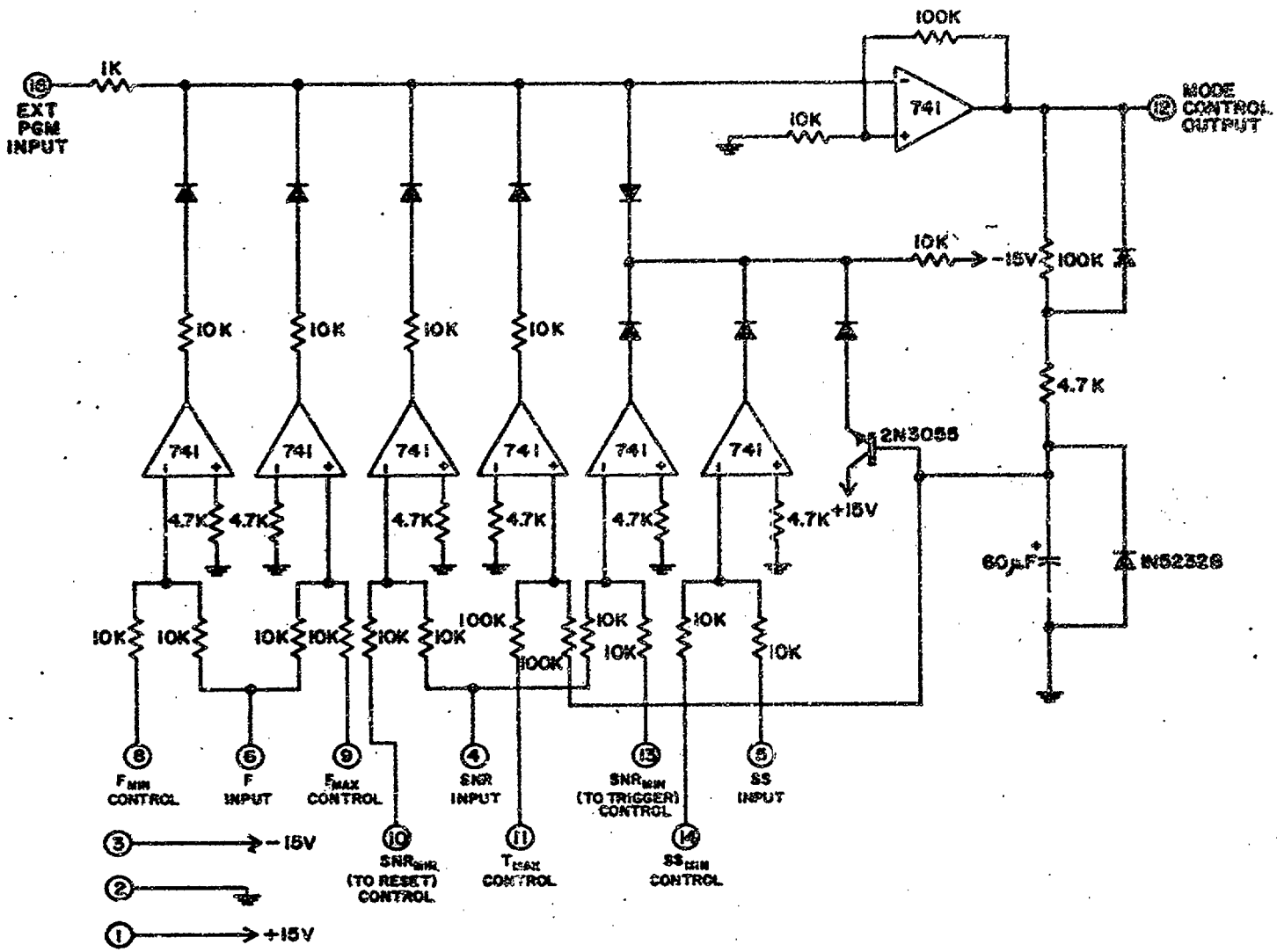


FIGURE B.11 SCHEMATIC OF TRACK/RESET LOGIC CARD, PC10.

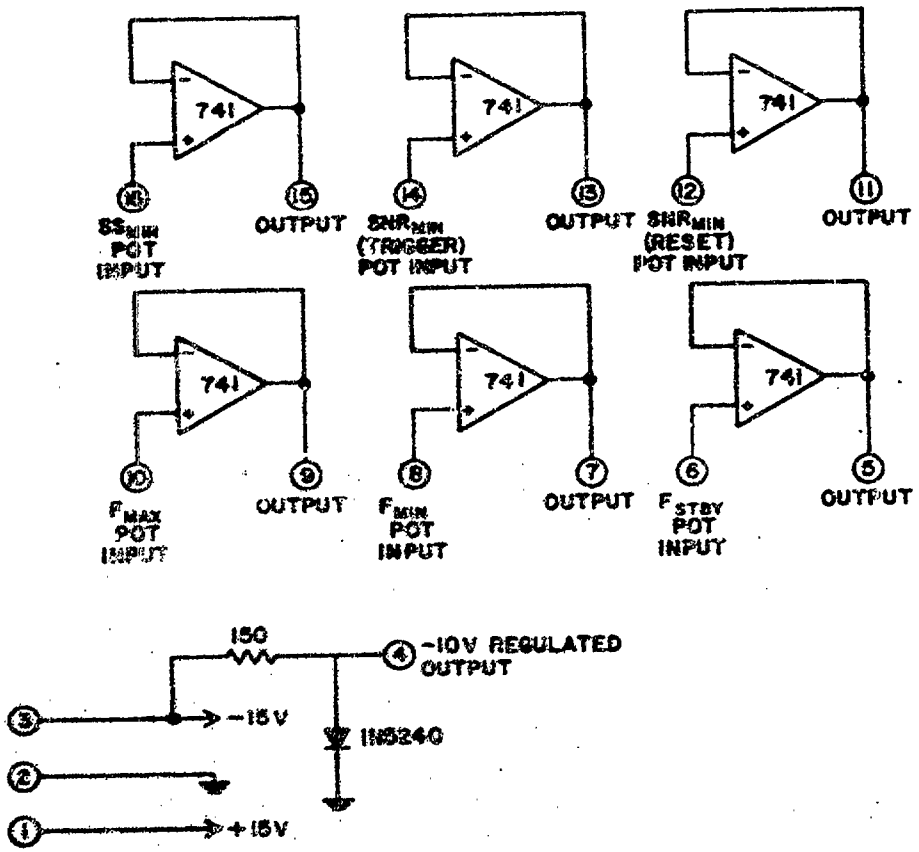


FIGURE B.12 SCHEMATIC OF POTENTIOMETER BUFFER CARD, PC11.

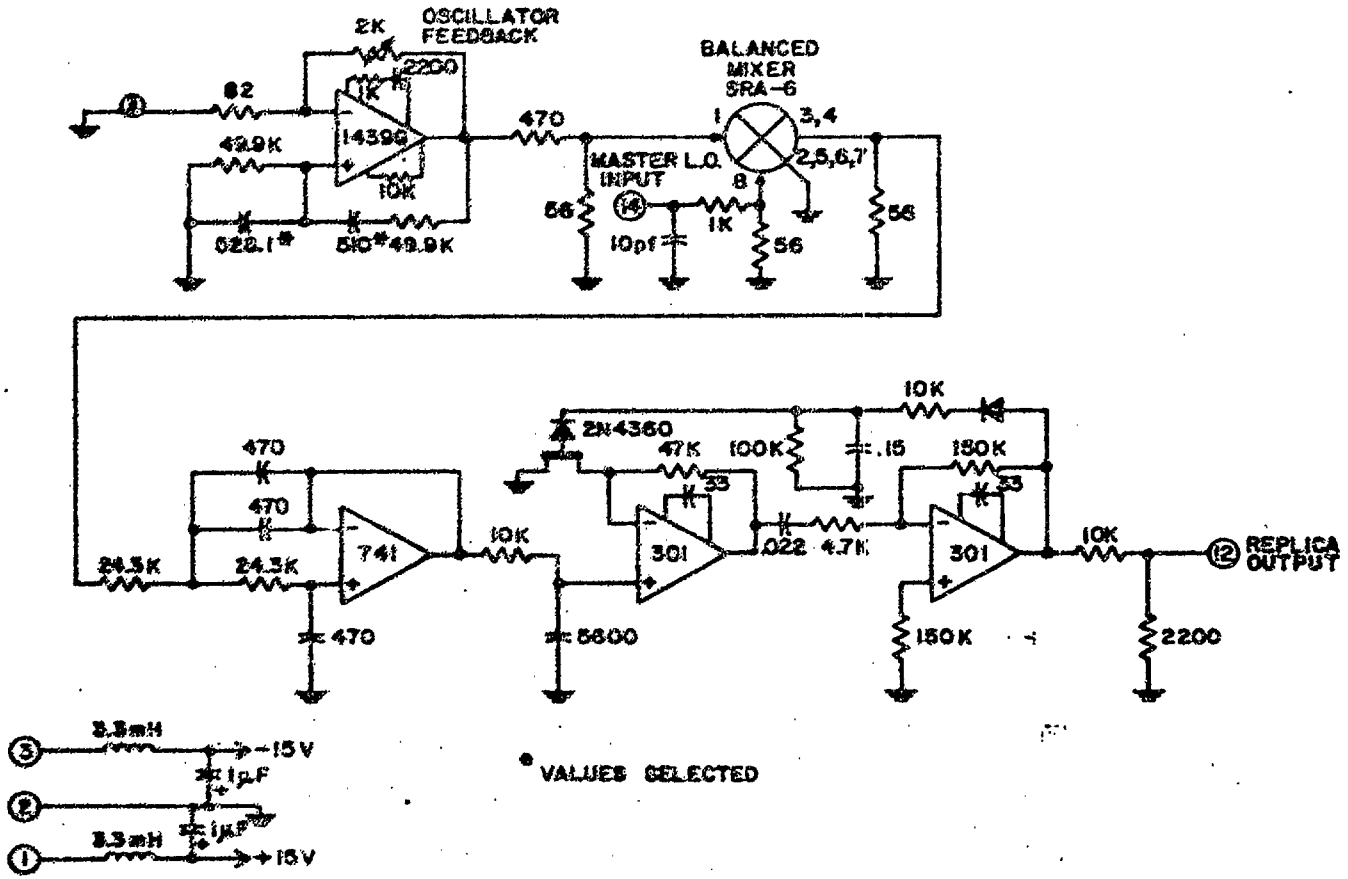


FIGURE B.13 SCHEMATIC OF FREQ TRANSLATOR CARD, PC12.

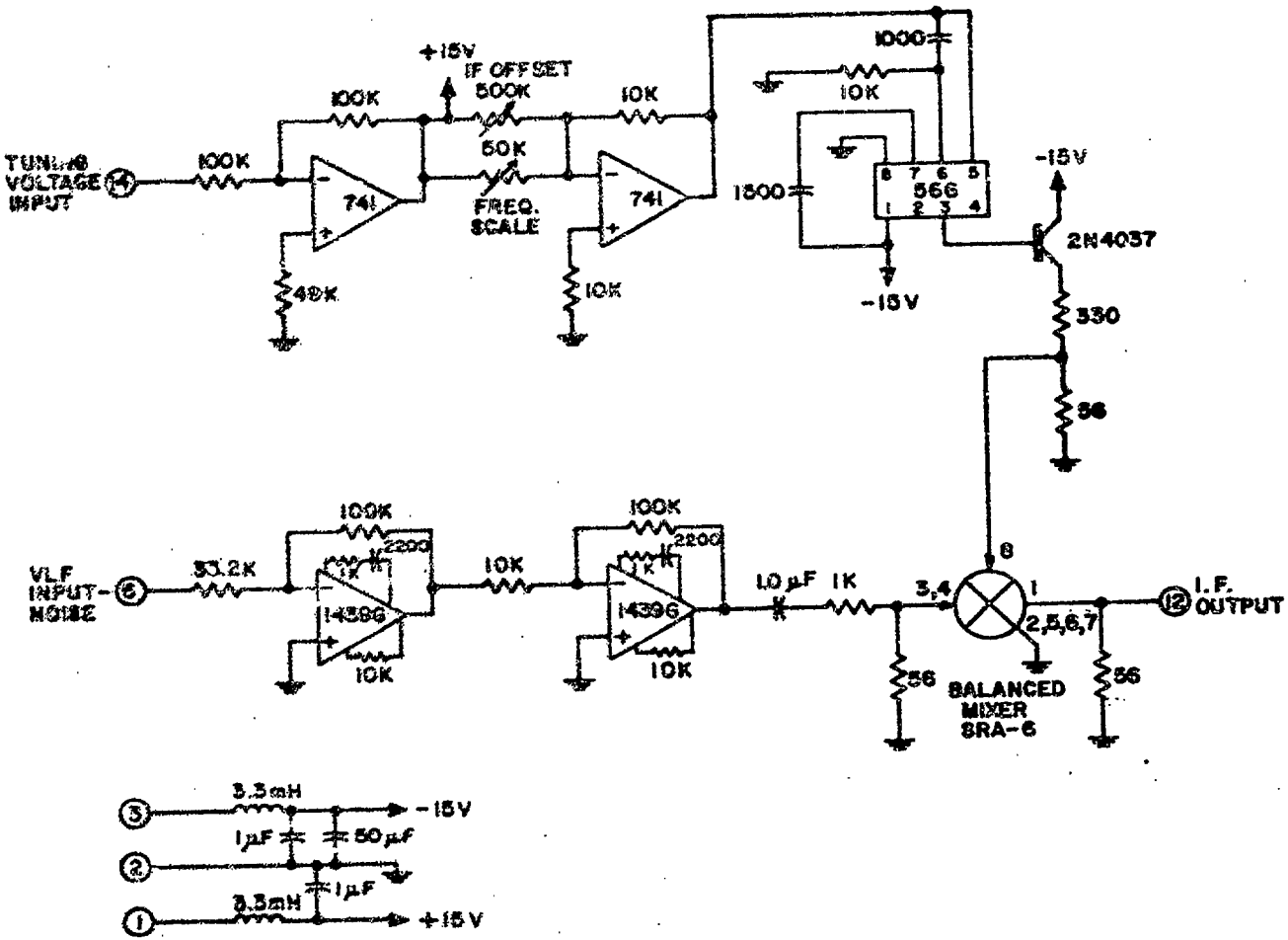


FIGURE B.14 SCHEMATIC OF NOISE LO/MIXER CARD, PC13.

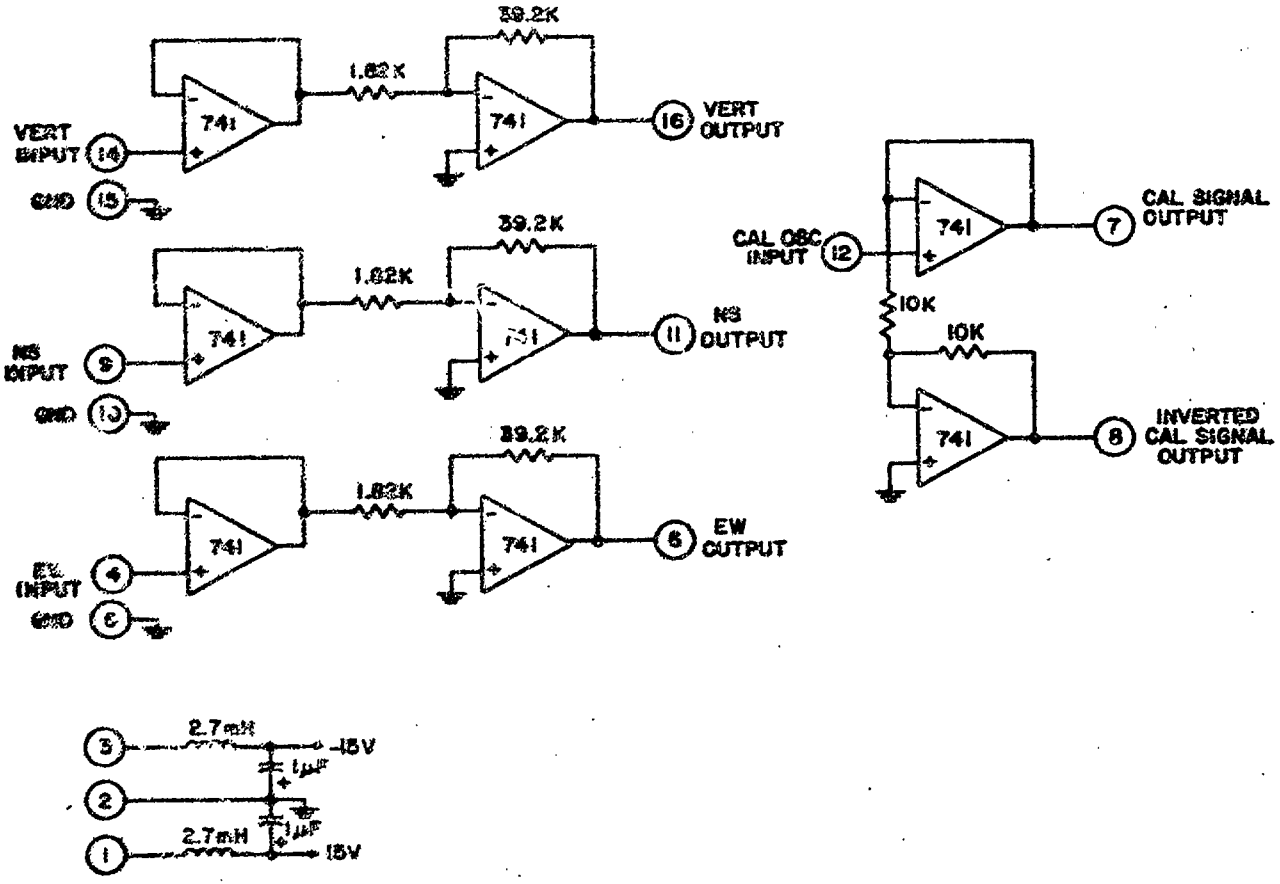


FIGURE B.15 SCHEMATIC OF PREAMP CARD, PC14.

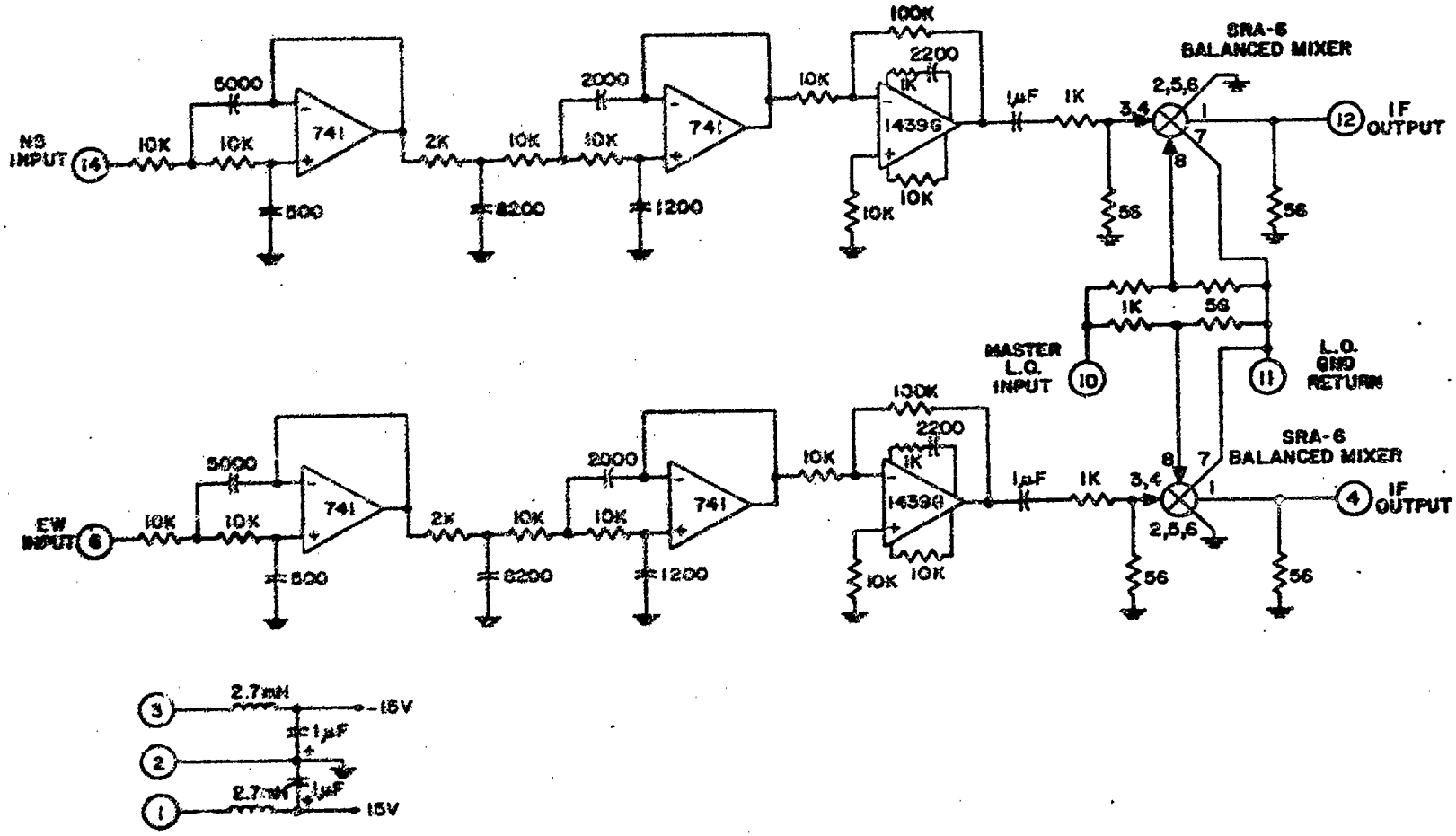


FIGURE B.16 SCHEMATIC OF MIXER-NS AND EW CARD, PC15.

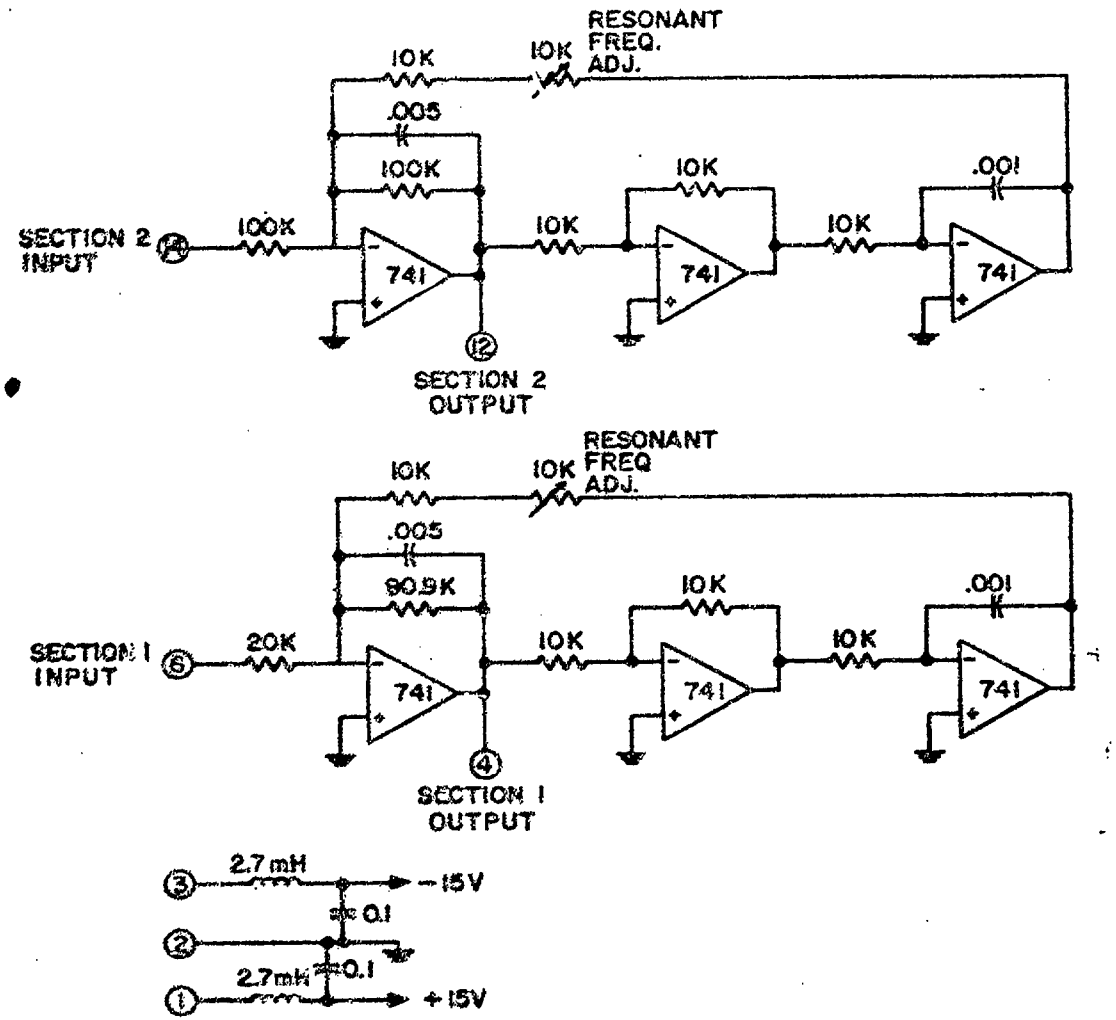


FIGURE B.17 SCHEMATIC OF IF FILTER-NS AND IF FILTER-EW, PC16 AND PC17 (IDENTICAL).

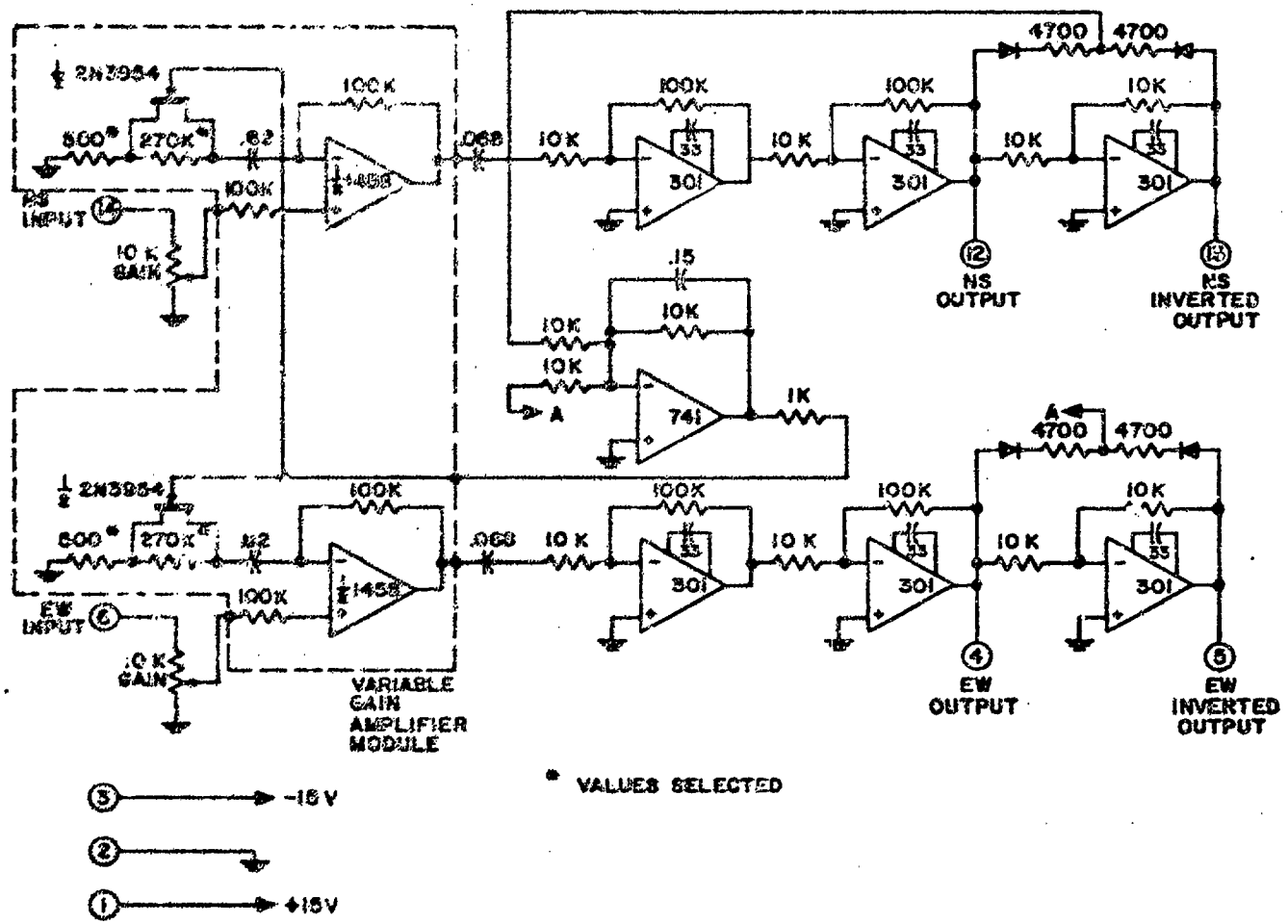


FIGURE B.18 SCHEMATIC OF AGC AMP CARD, PC18.

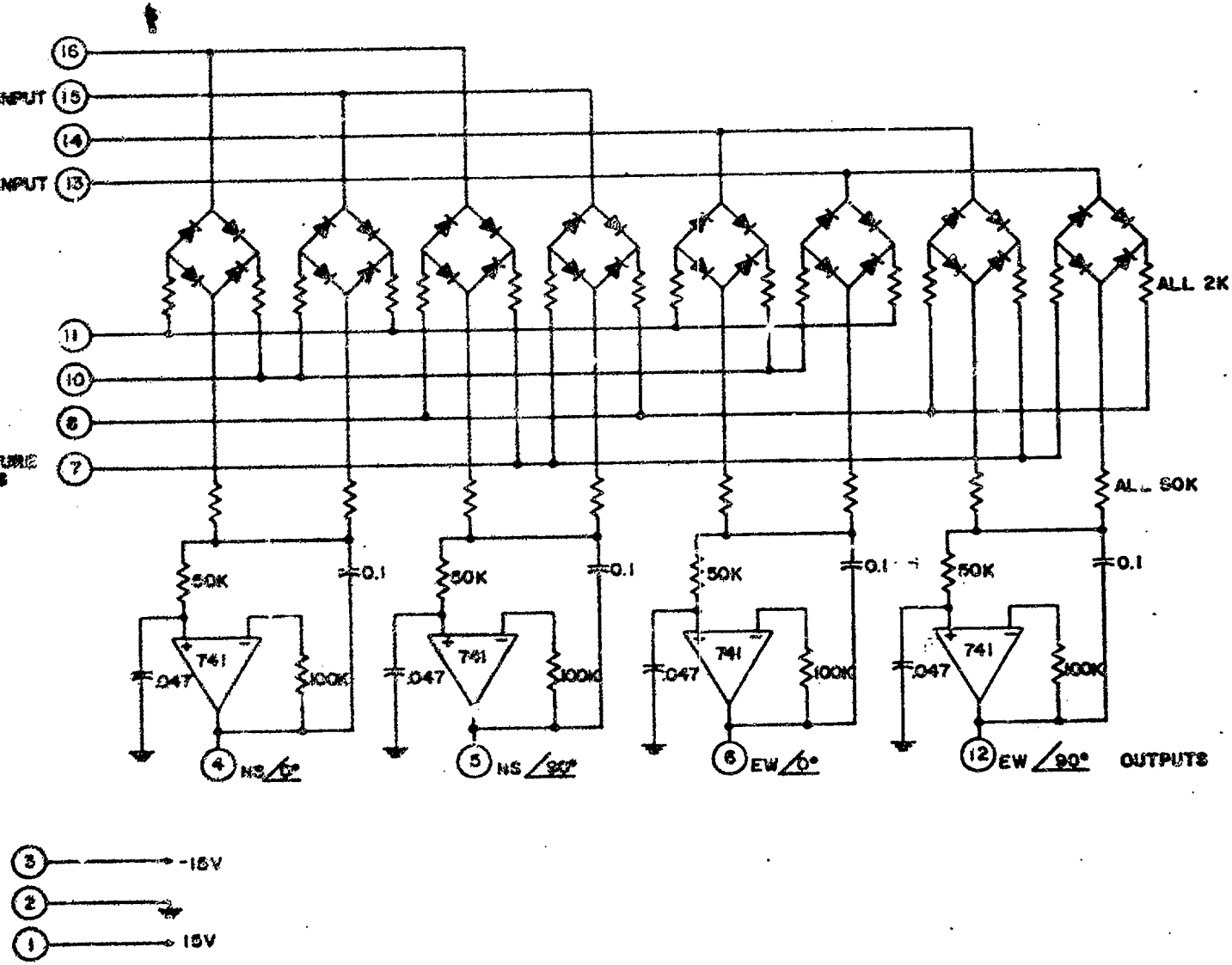


FIGURE B.19 SCHEMATIC OF SYNCHRONOUS DETECTOR CARD, PC19.

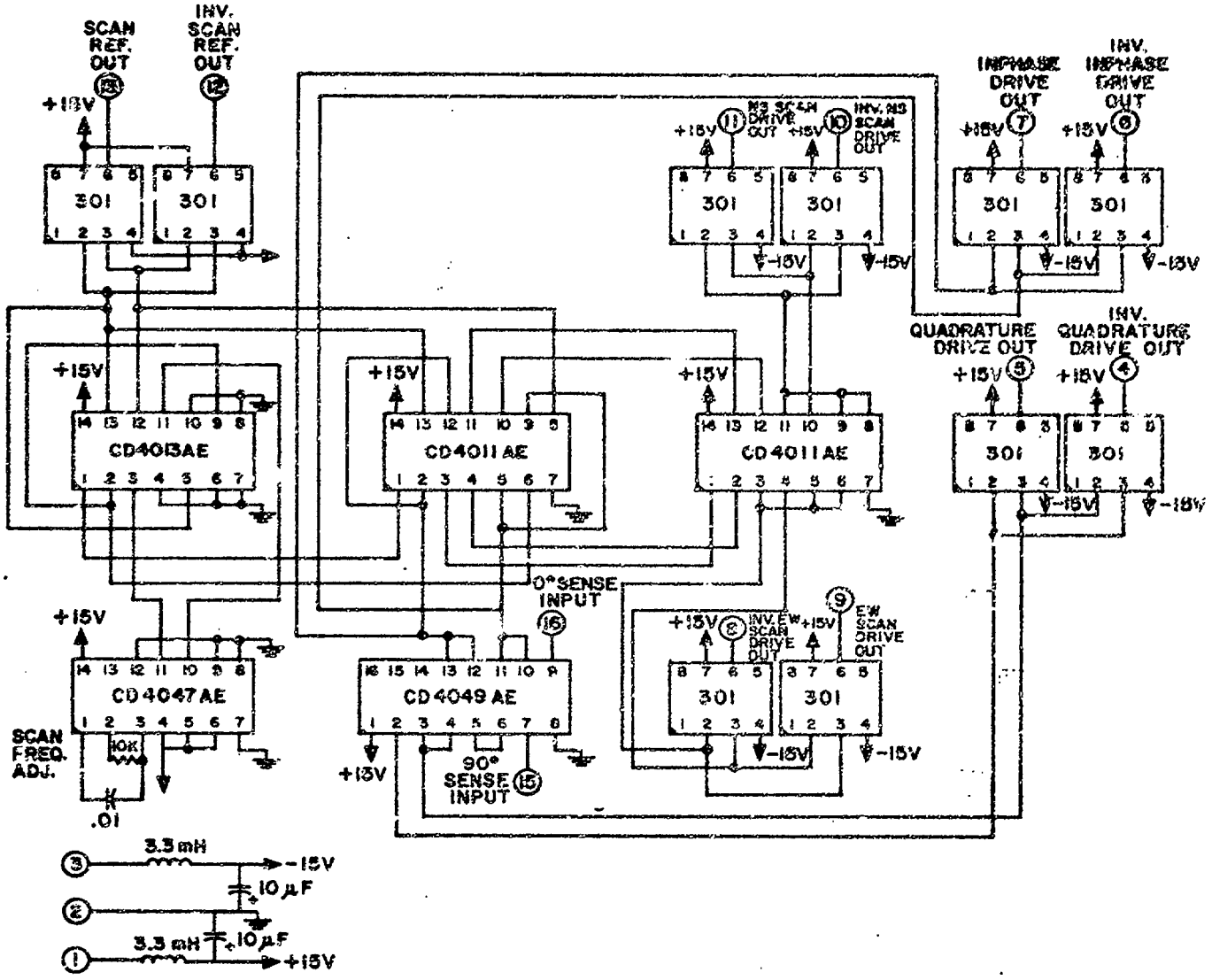


FIGURE B.20 SCHEMATIC OF DETECTOR DRIVER CARD, PC20.

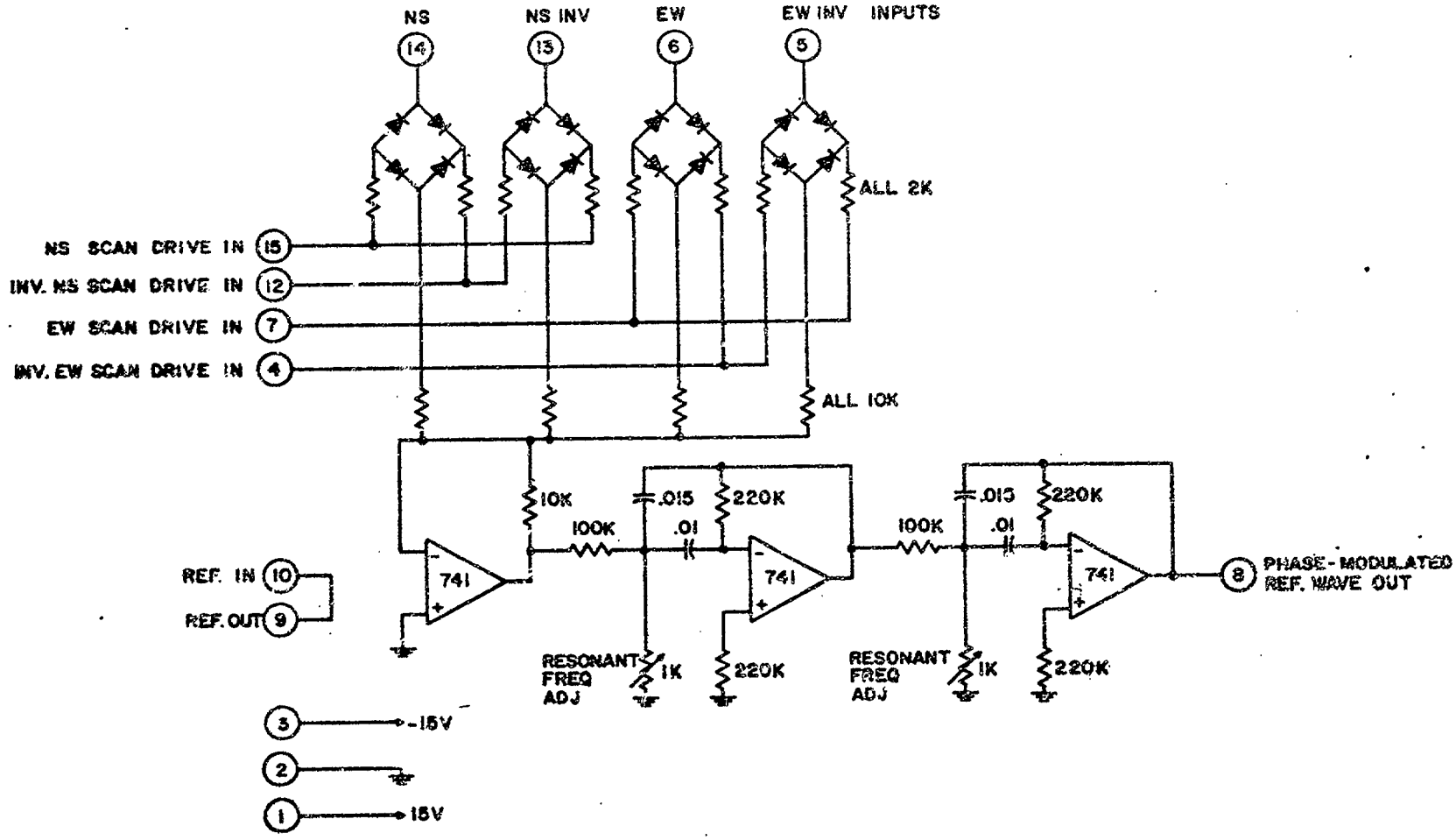


FIGURE B.21 SCHEMATIC OF SCANNING DETECTOR CARD, PC21.

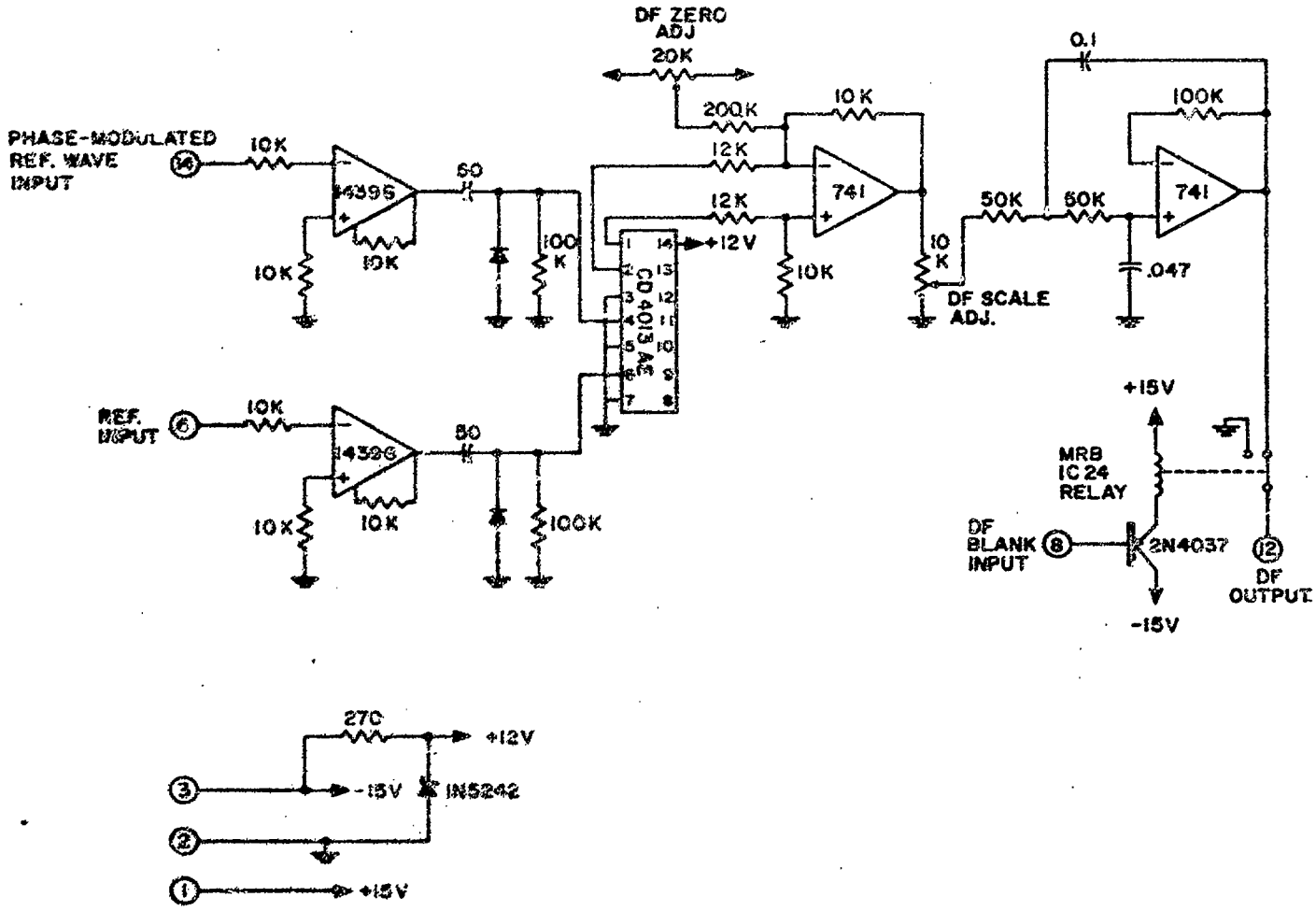


FIGURE B.22 SCHEMATIC OF PHASE METER CARD, PC22

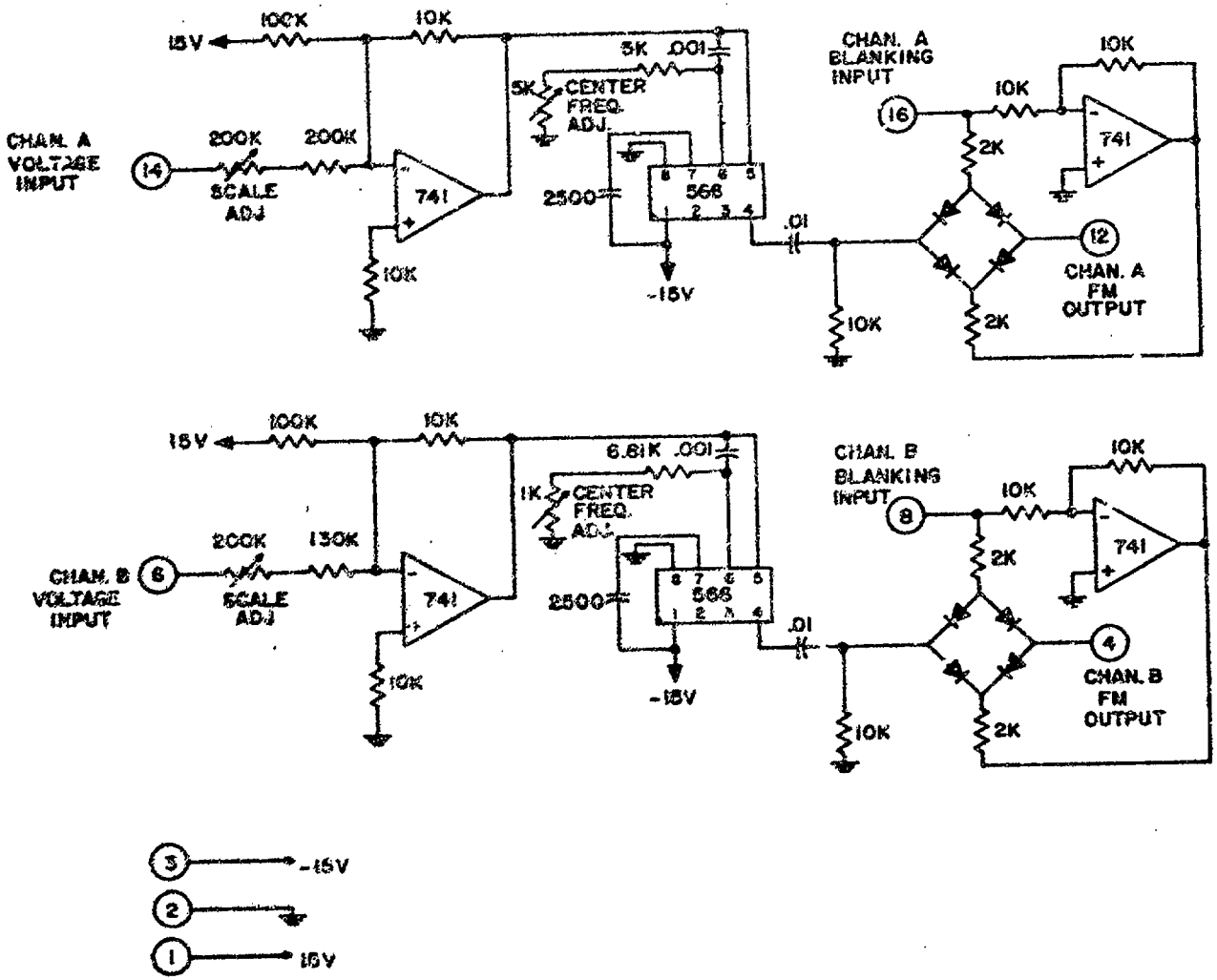


FIGURE B.23 SCHEMATIC OF FM OSCILLATORS CARD, PC23.

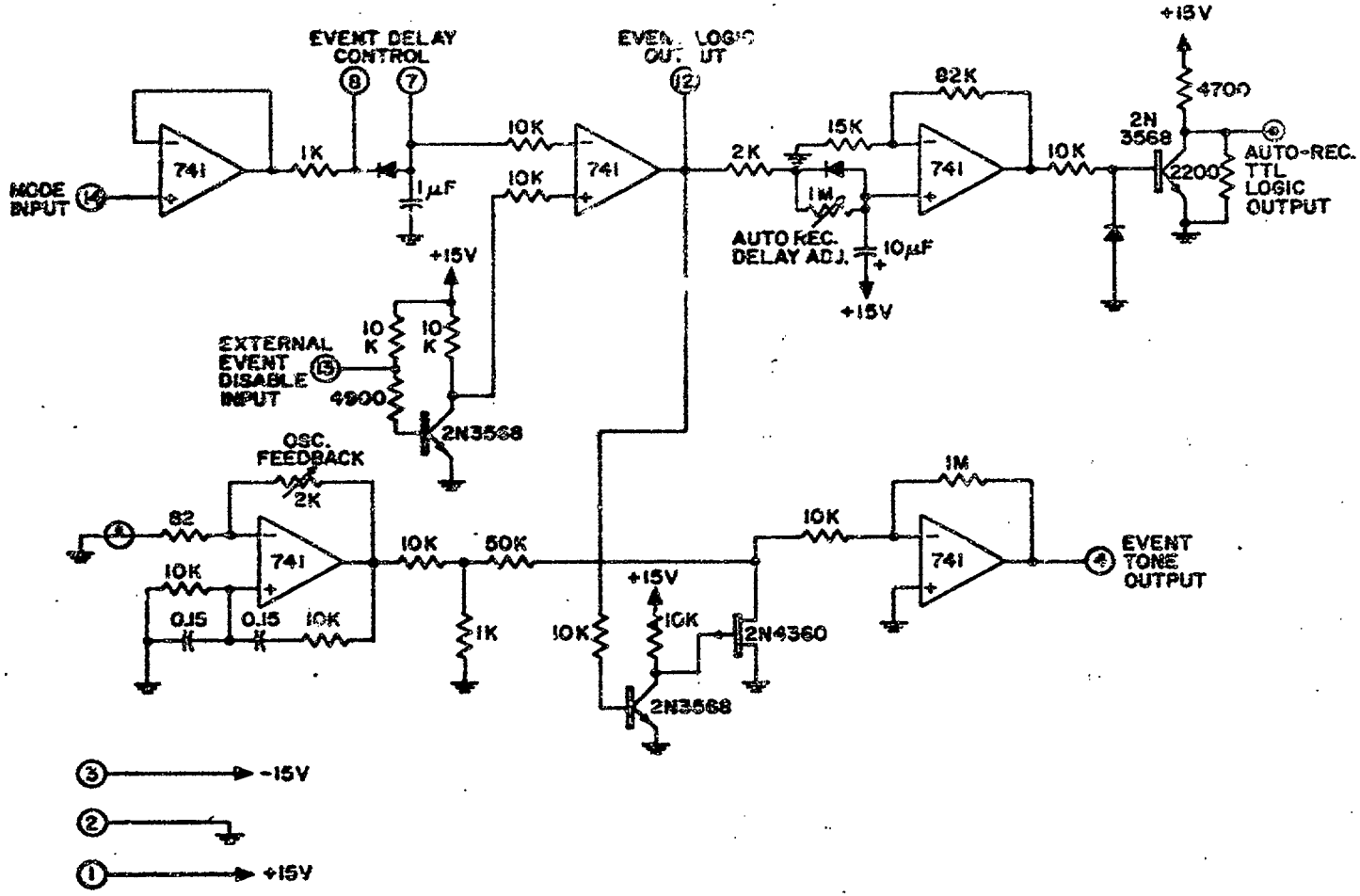


FIGURE B.24 SCHEMATIC OF EVENT LOGIC CARD, PC24.

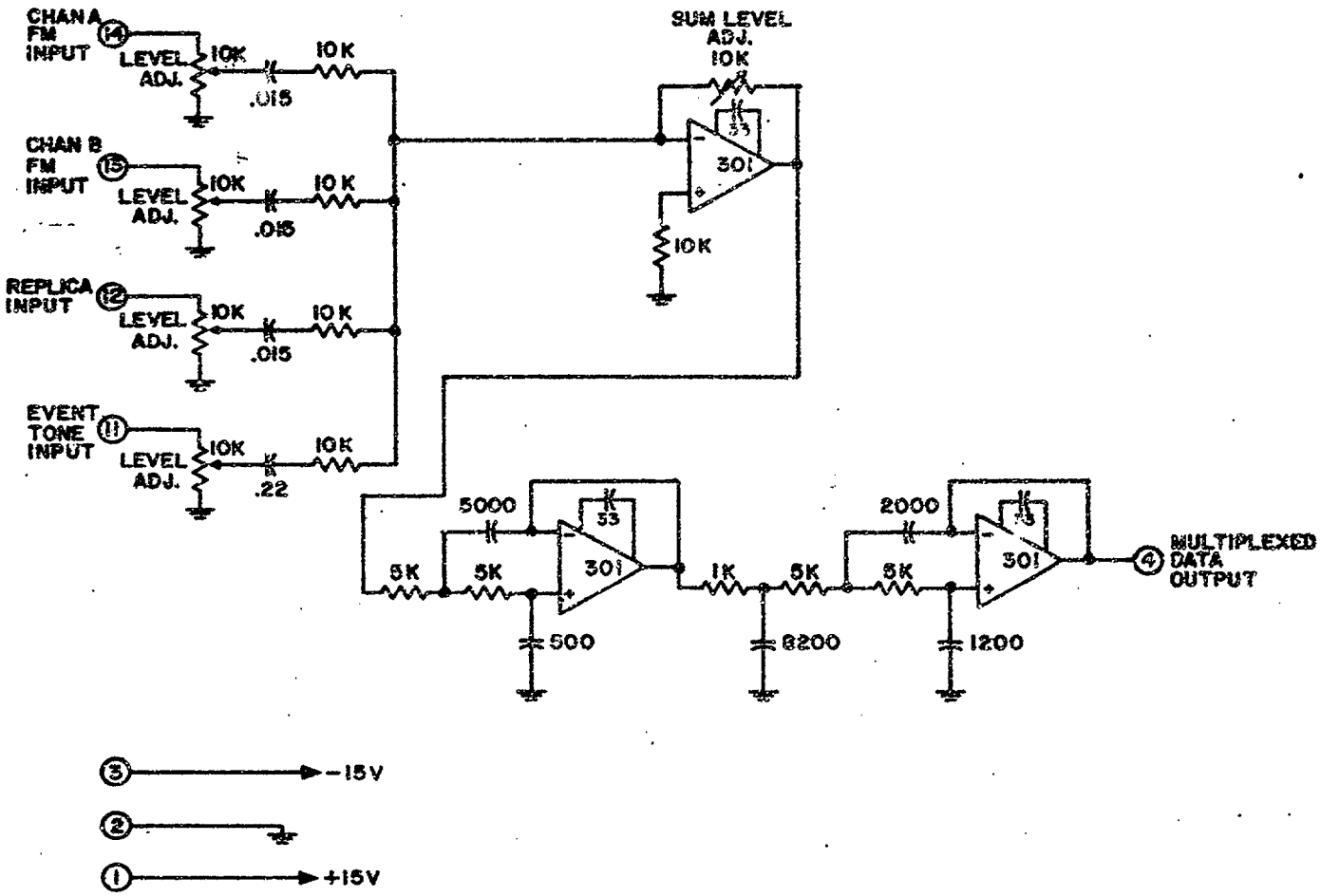


FIGURE B.25 SCHEMATIC OF AUDIO SUMMER CARD, PC25

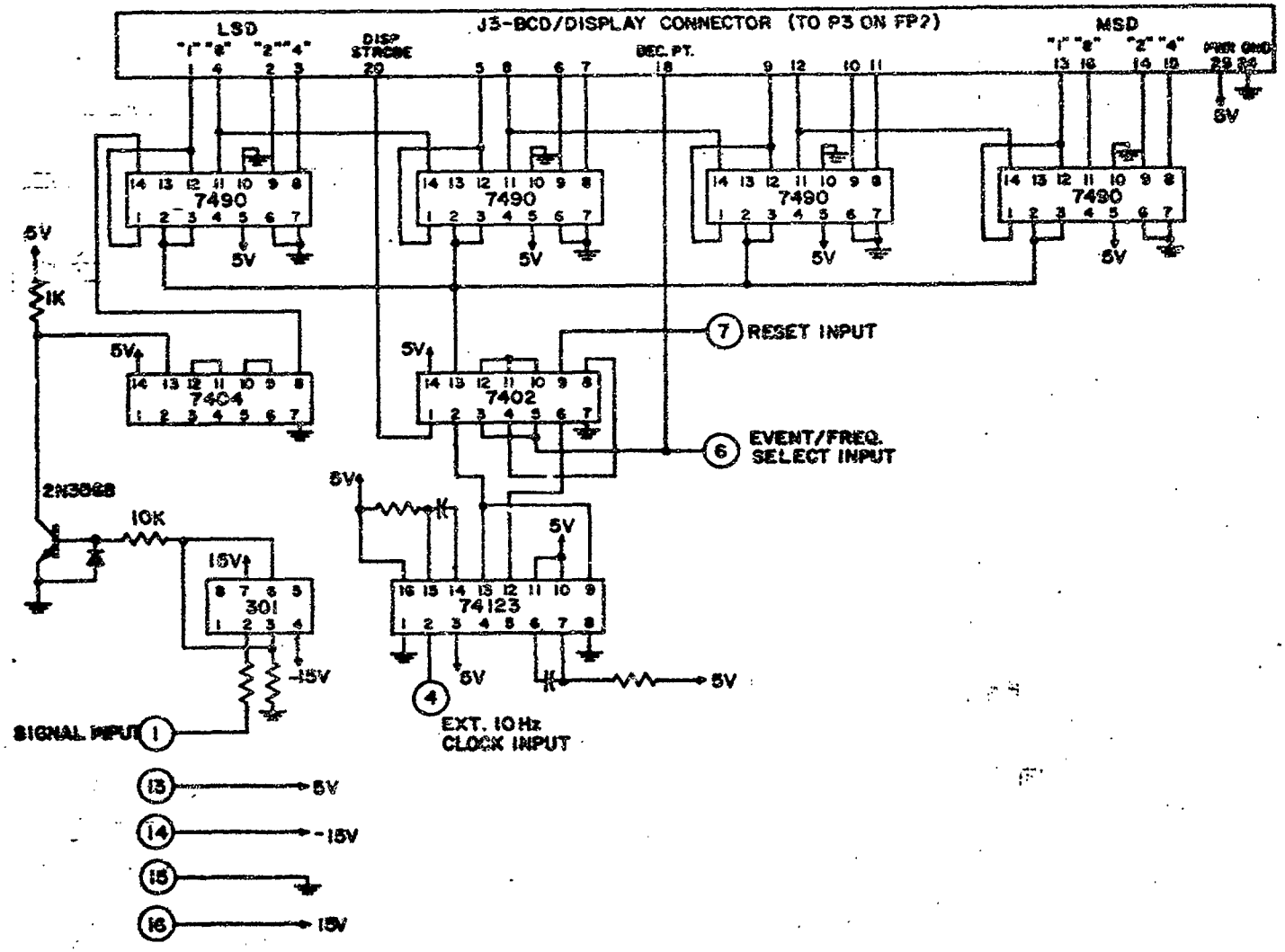


FIGURE B.26 SCHEMATIC OF FREQUENCY COUNTER CARD, PC27.

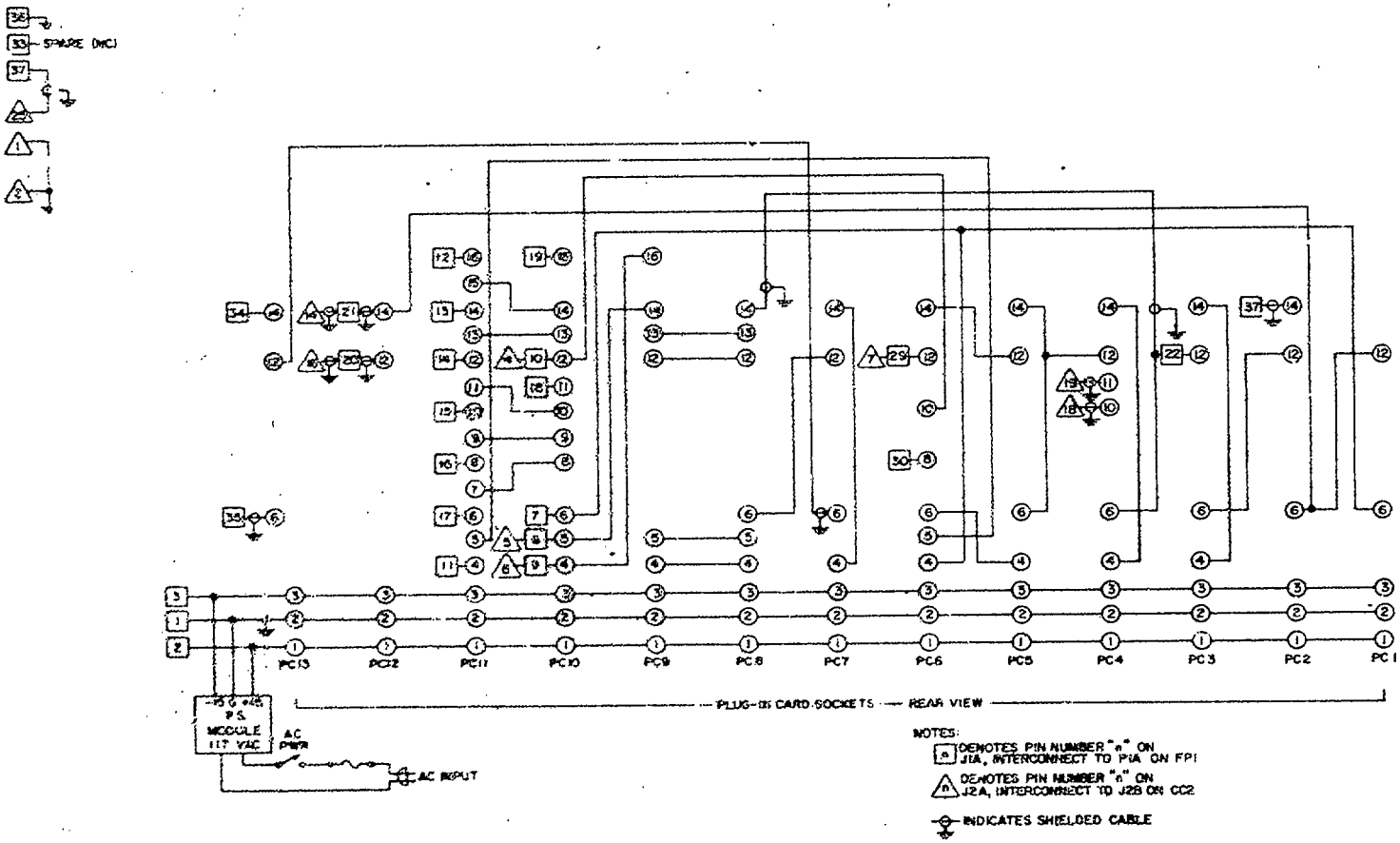


FIGURE B.27 SCHEMATIC OF TRACKING RECEIVER CARD CHASSIS, CC1.

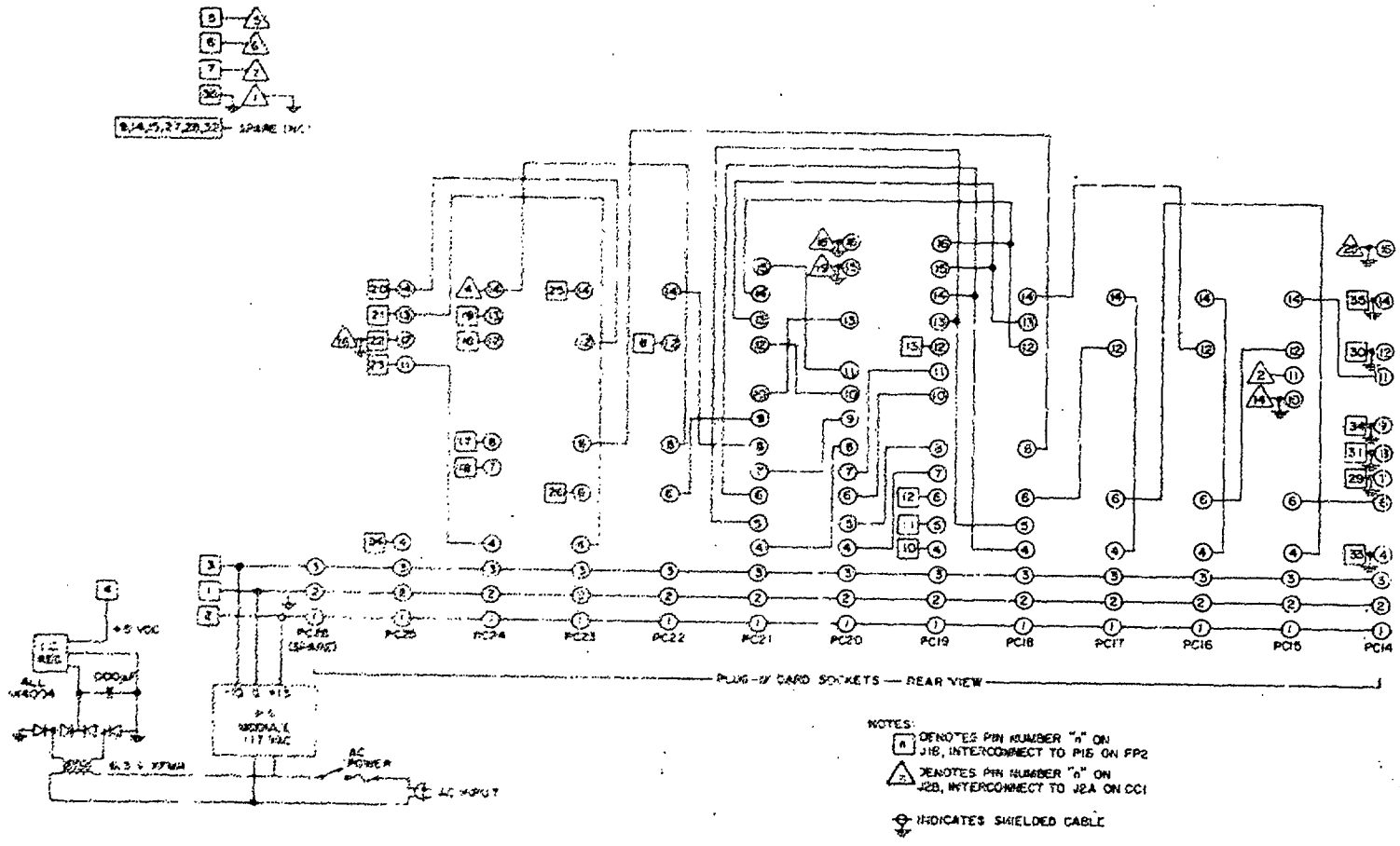


FIGURE B.28 SCHEMATIC OF DF RECEIVER CARD CHASSIS, CC2.

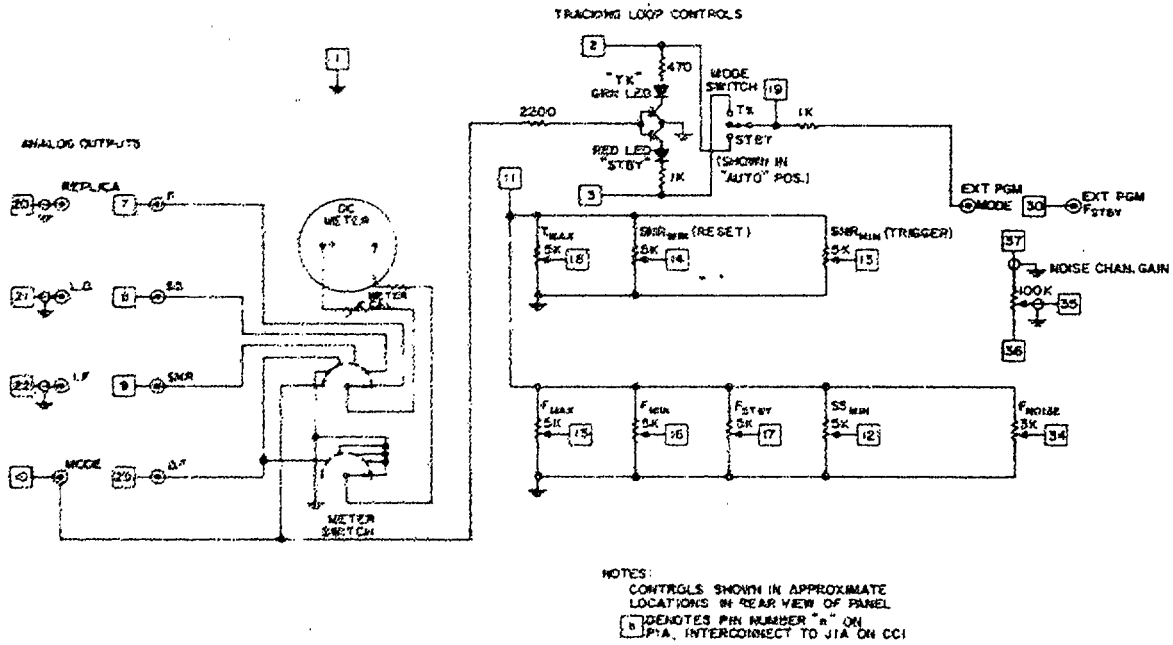


FIGURE B.29 SCHEMATIC OF TRACKING RECEIVER FRONT PANEL, FP1.

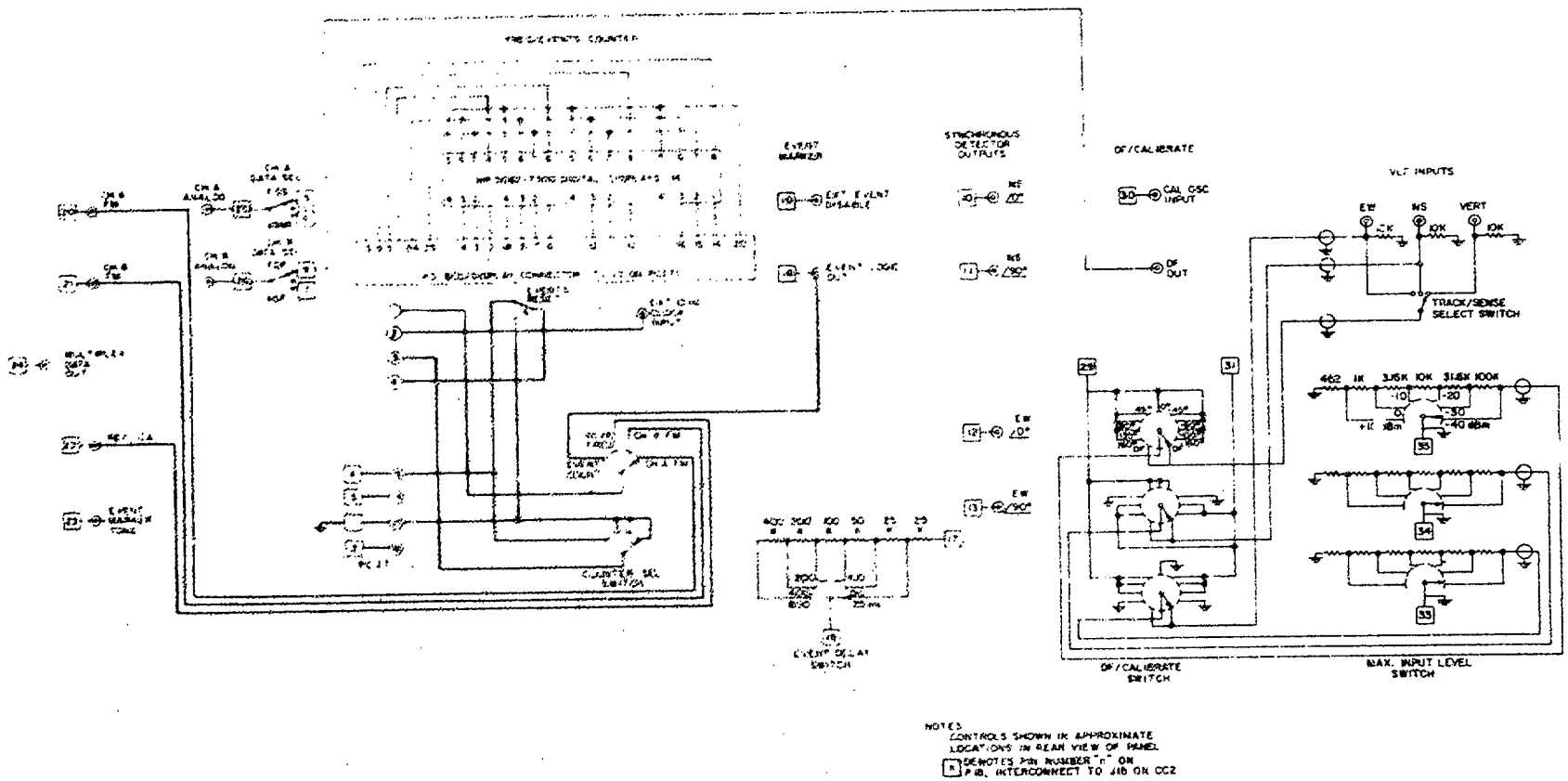


FIGURE B.30 SCHEMATIC OF DF RECEIVER FRONT PANEL, FP2.

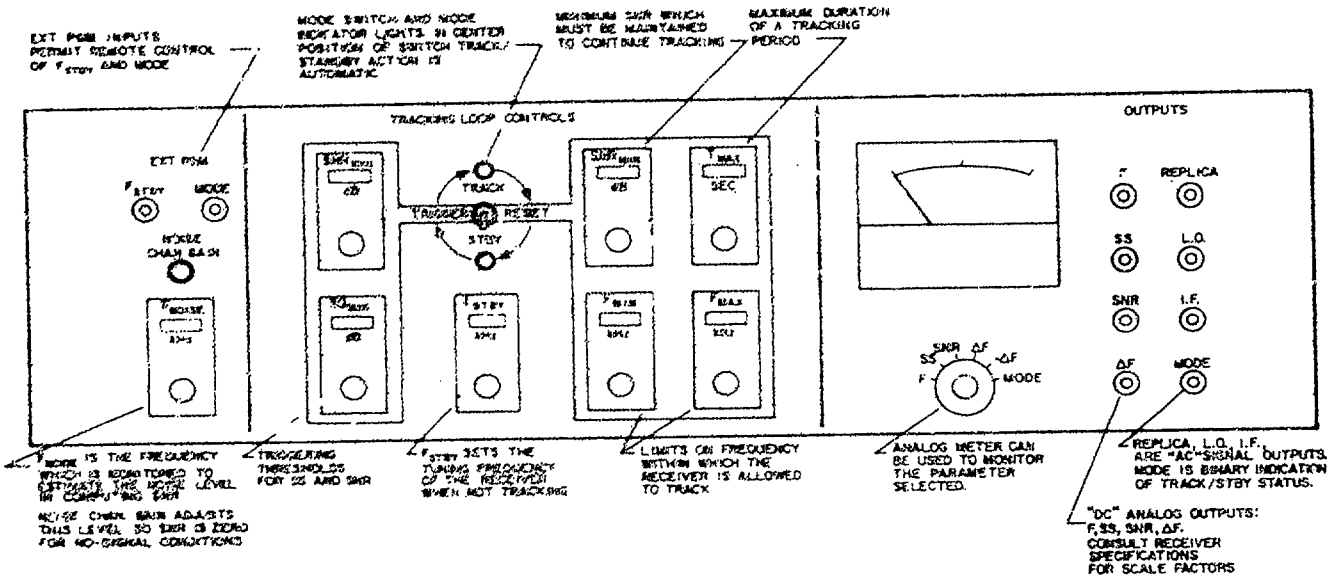


FIGURE B.31 PICTORIAL DIAGRAM OF TRACKING RECEIVER FRONT PANEL.

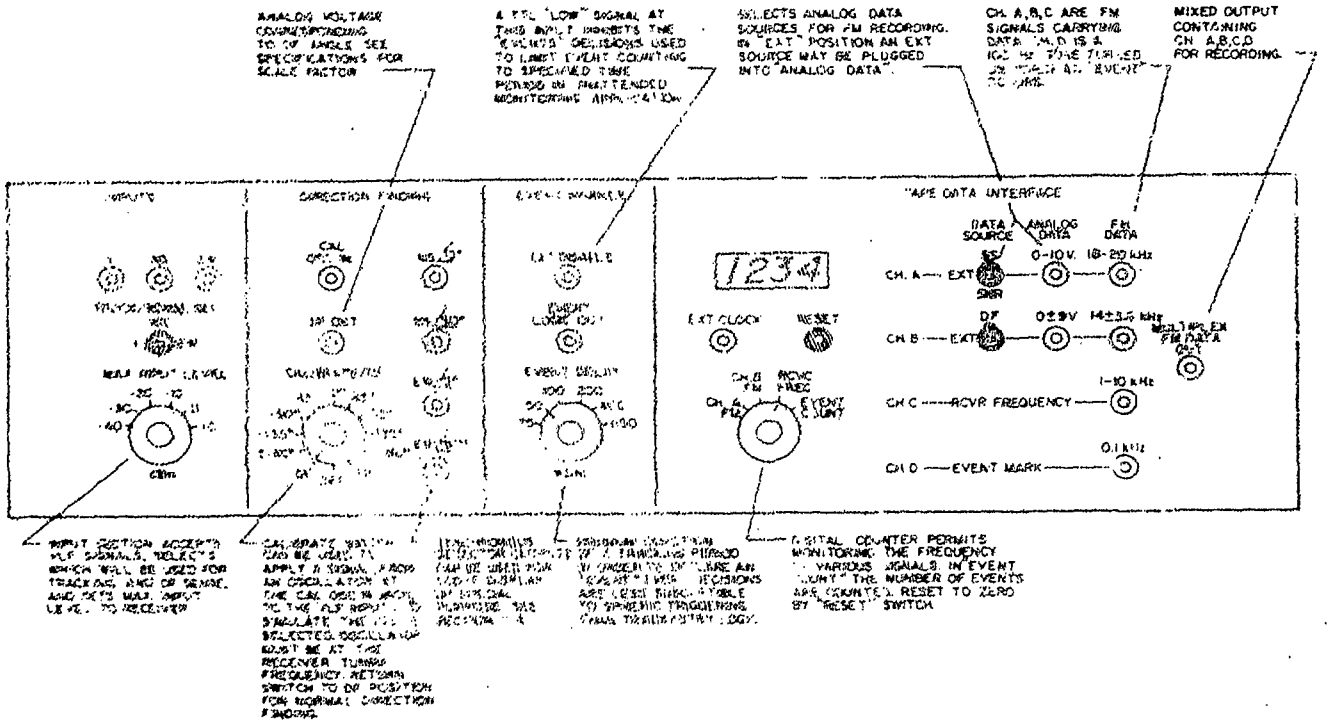


FIGURE B.32 PICTORIAL DIAGRAM OF DF RECEIVER FRONT PANEL

## REFERENCES


Adcock, F. and C. Clarke, The location of thunderstorms by radio direction finding, J.I.E.E., 94, III, 115, 1947.

Axford, W. I., Magnetospheric Convection, Rev. of Geophys., 7, 421, 1969.

Baghdady, E. J., Lectures on Communication System Theory, McGraw-Hill, New York, 1961.

Bullough, K. and J. L. Sagredo, VLF goniometer observations at Halley Bay, Antarctica--I. The equipment and the measurement of signal bearing, Planet. Space Sci., 21, 809, 1973.

Carpenter, D. L. and N. F. Seely, Cross-L plasma drifts in the outer plasmasphere; quite-time patterns and some substorm effects, J. Geophys. Res., in press, 1975.

Cousins, M. D., Direction finding on whistlers and related VLF signals, Tech. Rept. No. 3432-2, Radioscience Lab., Stanford Electronics Labs., Stanford University, Stanford, Calif., 1972.

Crary, J. H., The effect of the earth-ionosphere waveguide on whistlers, Tech. Rept. No. 9, Radioscience Lab., Stanford Electronics Labs., Stanford University, Stanford, Calif., 1961.

Crombie, D. D., Measurement of the arrival angle of "whistlers", J. Geophys. Res., 60, 364, 1955.

Dellcue, J., La determination de la direction d'arrivee et de la polarisation des atmospheriques siffleurs, premere partie, J. Phys. Radium, 8, 514, 1960.

Ellis, G. R. A., Directional observations of 5 Kc/s radiation from the earth's outer atmosphere, J. Geophys. Res., 65, 839, 1960.

Franks, R. E., Summary of propagation conditions and of the efficiency of electrically small antennas, Internal Report, Sylvania Elect. Dev. Labs., Sylvania Corp., 1964.

Gardner, F. M., Phaselock Techniques, Wiley and Sons, New York, 1966.

Hefley, G., R. F. Linfield, and T. L. Davis, The Ephi system For VLF direction finding, J. Res. NBS, 65C, 43, 1961.

Helliwell, R. A., Whistlers and Related Ionospheric Phenomena, Stanford University Press, Stanford, California, 1965.

Helliwell, R. A. and J. P. Katsufrakis, VLF wave injection into the magnetosphere from Siple Station, Antarctica, J. Geophys. Res., 79, 2511, 1974.

Horner, F., The accuracy of the location of sources of atmospherics by radio direction finding, Proc. I.E.E., 101, III, 383, 1954.

Horner, F., Very-low-frequency propagation and direction-finding, Proc. I.E.E., 104B, 73, 1957.

Kukes, I. S., and M. Y. Starik, Osnovy Radiopelengatsii (Principles of Radio Direction Finding), Soviet Publishing House, Moscow, 1962.

Melsa, J. L., and D. G. Schultz, Linear Control Systems,, McGraw-Hill, New York, 1969.

Ockenden, C. V., Sferics, Meteorological Magazine, 83, 137, 1954.

Panter, P. F., Modulation, Noise, and Spectral Analysis, McGraw-Hill, New York, 1965.

Seely, N., personal communication, November 1975.

Tow, J., A step-by-step active filter design, IEEE Spectrum, 6, 64, December 1969.

Tsuruda, K. and K. Hayashi, A new method for direction finding of elliptically polarized VLF waves, Report No. 509, Institute of Space and Aero. Sci., University of Tokyo, Tokyo, 1974.

Watts, J. M., Direction findings on whistlers, J. Geophys. Res., 64, 2029, 1959.

Wheeler, H. A., Fundamental limitations of small antennas, Proc. IRE, 34, 1479, 1946.

SECURITY CLASSIFICATION OF THIS PAGE (When Data Entered)

# REPORT DOCUMENTATION PAGE

READ INSTRUCTIONS BEFORE COMPLETING FORM

| | |
|---|---|
| 1. REPORT NUMBER: 3456-2 | 2. GOVT ACCESSION NO. |
| 3. RECIPIENT'S CATALOG NUMBER | |
| 4. TITLE (and Subtitle): A Frequency-Tracking Direction Finder for Whistlers and Other Very Low Frequency Signals | 5. TYPE OF REPORT & PERIOD COVERED: Technical Report 1975 |
| | 6. PERFORMING ORG. REPORT NUMBER: SEL-76-001 |
| 7. AUTHOR(s): Mark Keith Leavitt | 8. CONTRACT OR GRANT NUMBER(s): Nonr N00014-67-A-0112-0012 |
| 9. PERFORMING ORGANIZATION NAME AND ADDRESS: Radioscience Laboratory, Stanford Electronics Labs., Stanford Univ., Stanford, Ca. | 10. PROGRAM ELEMENT, PROJECT, TASK AREA & WORK UNIT NUMBERS |
| 11. CONTROLLING OFFICE NAME AND ADDRESS: Office of Naval Research, Arlington, Va. 22217 | 12. REPORT DATE: December 1975<br>13. NUMBER OF PAGES: 178 |
| 14. MONITORING AGENCY NAME & ADDRESS (if different from Controlling Office): Office of Naval Research, Electronics Program Office, Arlington, Va. 22217 | 15. SECURITY CLASS. (of this report): unclassified<br>15a. DECLASSIFICATION/DOWNGRADING SCHEDULE |

16. DISTRIBUTION STATEMENT (of this Report)

approved for public release; distribution unlimited

17. DISTRIBUTION STATEMENT (of the abstract entered in Block 20, if different from Report)

same

18. SUPPLEMENTARY NOTES

19. KEY WORDS (Continue on reverse side if necessary and identify by block number)

direction finder
very low frequency signals
whistlers

20. ABSTRACT (Continue on reverse side if necessary and identify by block number)

Whistlers and related very low frequency radio signals are guided in ducts of enhanced or reduced ionization along the geomagnetic lines of force of the earth's magnetosphere. The signals convey information about the distribution of particles in the plasma through which they have propagated and about the occurrence of wave-particle interactions in the magnetosphere. Direction-finding on such signals will aid in locating the ducts and measuring their temporal drifts, thus making an important contribution to studies of magneto-

DD FORM 1 JAN 73 1473 EDITION OF 1 NOV 65 IS OBSOLETE unclassified

SECURITY CLASSIFICATION OF THIS PAGE (When Data Entered)

spheric convection. The signals, although narrowband in nature, exhibit wide frequency excursions in the 1 to 10 kilohertz range. An innovative technique is presented for tracking these frequency excursions in real time to produce a filterred, quasimonochromatic version of the signal. The voltages induced by the incident wave on two orthogonal loop antennas and a vertical monopole antenna are processed by this method. The filtered signals are then cross-multiplied in a manner analogous to a Poynting vector calculation to obtain a continuous indication of the wave direction of arrival. The design, construction, and laboratory testing of a prototype instrument are described. Field testing of the instrument was performed at Stanford, California, and Roberval, Quebec, Canada. Operating at fixed frequencies, the direction-finder produced accurate results on VLF transmissions in the 10 to 20 kilohertz range from NAA, NPG, GBR, and the Omega stations. Well defined bearing indications were also obtained for spherics at frequencies in the 1 to 10 kilohertz region. Successful frequency-tracking and direction-finding were demonstrated for a wide variety of whistler-mode signals, including whistlers, chorus, and discrete emissions. The technique was also successfully applied to emissions in the 2 to 7 kilohertz range stimulated by the VLF transmitter at Siple Station, Antarctica. Direction of arrival indications on whistlers were consistent with the duct positions predicted by frequency profile analysis. Evidence was also presented of temporal changes in the direction of arrival of signals which may be an indication of duct drifts. This instrument provides, for the first time, a continuous, immediately readable record of the direction of arrival of whistler-mode signals. It could also be applied to the automatic acquisition of whistler-mode signals and measurement of their amplitude and frequency variations.

# DISTRIBUTION LIST FOR ONR ELECTRONICS PROGRAM OFFICE

| | |
|---|---|
| Director<br>Advanced Research Projects Agency<br>Attn: Technical Library<br>1400 Wilson Boulevard<br>Arlington, Virginia 22209 | 1 copy |
| Office of Naval Research<br>Electronics Program Office (Code 427)<br>800 North Quincy Street<br>Arlington, Virginia 22217 | 1 copy |
| Office of Naval Research<br>Code 105<br>800 North Quincy Street<br>Arlington, Virginia 22217 | 6 copies |
| Naval Research Laboratory<br>Department of the Navy<br>Attn: Code 2627<br>Washington, D. C. 20375 | 6 copies |
| Office of the Director of Defense<br>Research and Engineering<br>Information Office Library Branch<br>The Pentagon<br>Washington, D. C. 20301 | 1 copy |
| U. S. Army Research Office<br>Box CM, Duke Station<br>Durham, North Carolina 27706 | 1 copy |
| Defense Documentation Center<br>Cameron Station<br>Alexandria, Virginia 22314 | 12 copies |
| Director National Bureau of Standards<br>Attn: Technical Library<br>Washington, D. C. 20234 | 1 copy |
| Commanding Officer<br>Office of Naval Research Branch Office<br>536 South Clark Street<br>Chicago, Illinois 60605 | 1 copy |
| Department of the Navy<br>Office of Naval Research<br>Code 200<br>Arlington, Va. 22217 | 1 copy |

Distribution List for ONR Electronics Program Office

San Francisco Area Office — 1 copy
Office of Naval Research
50 Fell Street
San Francisco, California 94102

Air Force Office of Scientific Research — 1 copy
Department of the Air Force
Washington, D. C. 20333

Commanding Officer — 1 copy
Office of Naval Research Branch Office
1030 East Green Street
Pasadena, California 91101

Commanding Officer — 1 copy
Office of Naval Research Branch Office
495 Summer Street
Boston, Massachusetts 02210

Director — 1 copy
U. S. Army Engineering Research
and Development Laboratories
Fort Belvoir, Virginia 22060
Attn: Technical Documents Center

ODDR&E Advisory Group on Electron Devices — 1 copy
201 Varick Street
New York, New York 10014

New York Area Office — 1 copy
Office of Naval Research
207 West 24th Street
New York, New York 10011

Air Force Weapons Laboratory — 1 copy
Technical Library
Kirtland Air Force Base
Albuquerque, New Mexico 87117

Air Force Avionics Laboratory — 1 copy
Air Force Systems Command
Technical Library
Wright-Patterson Air Force Base
Dayton, Ohio 45433

Distribution List for ONR Electronics Program Office

| | |
|---|---|
| Air Force Cambridge Research Laboratory<br>L. G. Hanscom Field<br>Technical Library<br>Cambridge, Massachusetts 02138 | 1 copy |
| Harry Diamond Laboratories<br>Technical Library<br>Connecticut Avenue at Van Ness, N. W.<br>Washington, D. C. 20438 | 1 copy |
| Naval Air Development Center<br>Attn: Technical Library<br>Johnsville<br>Warminster, Pennsylvania 18974 | 1 copy |
| Naval Weapons Center<br>Technical Library (Code 753)<br>China Lake, California 93555 | 1 copy |
| Naval Training Device Center<br>Technical Library<br>Orlando, Florida 22813 | 1 copy |
| Naval Research Laboratory<br>Underwater Sound Reference Division<br>Technical Library<br>P. O. Box 8337<br>Orlando, Florida 32806 | 1 copy |
| Navy Underwater Sound Laboratory<br>Technical Library<br>Fort Trumbull<br>New London, Connecticut 06320 | 1 copy |
| Commandant, Marine Corps<br>Scientific Advisor (Code AX)<br>Washington, D. C. 20380 | 1 copy |
| Naval Ordnance Station<br>Technical Library<br>Indian Head, Maryland 20640 | 1 copy |
| Naval Ship Engineering Center<br>Philadelphia Division<br>Technical Library<br>Philadelphia, Pennsylvania 19112 | 1 copy |

Distribution List for ONR Electronics Program Office

| | |
|---|---|
| Naval Postgraduate School<br>Technical Library (Code 0212)<br>Monterey, California 93940 | 1 copy |
| Naval Missile Center<br>Technical Library (Code 5632.2)<br>Point Mugu, California 93010 | 1 copy |
| Naval Ordnance Station<br>Technical Library<br>Louisville, Kentucky 40214 | 1 copy |
| Naval Oceanographic Office<br>Technical Library (Code 1640)<br>Suitland, Maryland 20390 | 1 copy |
| Naval Explosive Ordnance Disposal Facility<br>Technical Library<br>Indian Head, Maryland 20640 | 1 copy |
| Naval Electronics Laboratory Center<br>Technical Library<br>San Diego, California 92152 | 1 copy |
| Naval Undersea Warfare Center<br>Technical Library<br>3202 East Foothill Boulevard<br>Pasadena, California 91107 | 1 copy |
| Naval Weapons Laboratory<br>Technical Library<br>Dahlgren, Virginia 22448 | 1 copy |
| Naval Ship Research and Development Center<br>Central Library (Code L42 and L43)<br>Washington, D. C. 20007 | 1 copy |
| Naval Ordnance Laboratory White Oak<br>Technical Library<br>Silver Spring, Maryland 20910 | 1 copy |
| Naval Avionics Facility<br>Technical Library<br>Indianapolis, Indiana 46218 | 1 copy |